NUMERICAL STUDY OF LAMINAR UNSTEADY FLOW OVER AIRFOILS

A THESIS

Presented to

The Faculty of the Division of Graduate Studies

by

Narayanamoorthy Lakshmi Sankar

In Partial Fulfillment

of the Requirements for the Degree

Doctor of Philosophy in Aerospace Engineering

Georgia Institute of Technology

November, 1977

NUMERICAL STUDY OF

LAMINAR UNSTEADY FLOW OVER AIRFOILS

Approved:

James C. Wu, Chairman

G. Alvin Pierce

C. Virgil Smith

Date Approved by Chairman Nov. 28, 1977

ACKNOWLEDGMENTS

I want to express my sincere appreciation to Dr. James C. Wu, my teacher and advisor, for his guidance throughout my graduate academic career. His assistance and encouragement during the course of this study has been invaluable.

I would like to thank Drs. G. A. Pierce and C. V. Smith, the members of the Reading Committee for their useful suggestions.

This work was supported financially by the Office of Naval Research under Contract No. N00014-75-C-0249 and by Lockheed-Georgia Company under Contract No. CN52439.

My sincere thanks is extended to Ms. Shirleye McCombs for an excellent typing job of this thesis. Her patience in keeping track of my p's and ρ's has been remarkable.

My special thanks to my parents who have constantly encouraged me and unselfishly supported me. I also want to thank my wonderful friends for making the past few years at Georgia Tech a happy period. Very few friendships have meant more to me than those of Amir, Yehia, Shahid, Prak and Ann.

Finally, my grateful thanks to God for providing in such an abundant manner everything I have ever needed.

TABLE OF CONTENTS

Chapter Page

LIST OF TABLES

LIST OF ILLUSTRATIONS

LIST OF ILLUSTRATIONS (Continued)

LIST OF ILLUSTRATIONS (continued)

LIST OF ILLUSTRATIONS (continued)

LIST OF ILLUSTRATIONS (continued)

SUMMARY

A numerical scheme for the solution of two-dimensional incompressible Navier-Stokes equations is developed and presented, with special emphasis on laminar flow around oscillating airfoils. This scheme utilizes vorticity and velocity as dependent variables. The flow field is divided into two regions--an inner region close to the airfoil where the flow properties vary rapidly in space and time, and an outer region where the variation of flow properties is gradual. Finite element techniques are used to solve the vorticity transport equation in the inner region, and finite difference techniques are used in the outer region. The two regions overlap, so that the solution of the vorticity transport equation in the outer field may be used as the boundary condition for the solution of vorticity transport equation in the inner field and vice versa.

An explicit integral relationship available in open literature is used to determine the velocity field in terms of vorticity and velocity boundary conditions. The surface vorticity distribution is determined using an accurate, explicit numerical scheme. The integral representation for velocity, as well as the surface vorticity scheme permit the computations to be confined to the region of non-negligible vorticity.

The accuracy and the flexibility of the present method are demonstrated by considering two test cases involving bodies of simple

geometry. The numerical results are compared with available experimental data and other finite difference solutions. Numerical results are also presented for viscous flow over a Joukowski 12%. airfoil at zero and 3^{o} angles of attack.

The present method is applied to the study of viscous flow over an oscillating Joukowski 12%.airfoil. Three different combinations of the mean angle of attack, amplitude of the pitching motion and reduced frequency are considered. The numerical results are presented through time histories of loads as well as surface vorticity and pressure distributions at selected time levels. Stream line plots and constant-vorticity contours are also presented for selected cases. The numerical results indicate that the oscillatory motion can lead to considerable overshoot in the magnitude of the lift coefficient compared to the static lift coefficient. The lift coefficient is observed to lead the angle of attack in phase in all the three cases. The variation of the moment coefficient about quarter chord with angle of attack indicates that the aerodynamic damping is positive in all the cases considered. The viscous drag coefficient is found to be the chief contributor to the total drag whenever the separated flow region on the upper surface of the airfoil is not appreciably large. It is found that the viscous drag is relatively insensitive to the pitching motion whenever the amplitude of motion is small. Qualitative comparisons are made between the present results and the linearized potential flow results wherever applicable. Based on the present results, a detailed explanation for the time variation of the aerodynamic loads is given.

NOMENCLATURE

A	Area of Cross section of the two-dimensional body
B	Solid Boundary
D	Drag force along chord
f	Analytical transformation function
H	Scale factor, given by Equation (2)
k	Reduced frequency based on semi-chord
L	Chord length
L_1	Length of standing vortices
$\bar{n}$	Unit normal vector at the surface of the solid directed into the fluid
N	Linear interpolation function given by Equation (34)
p	Static pressure
Q	Total vorticity defined by Equation (16)
Q_1	Net total vorticity leaving downstream boundary
$\bar{r}$	Position vector in the rotating frame of reference
$\bar{r}'$	Position vector in the inertial frame of reference
R	Region of non-zero vorticity
$\bar{R}$	Region of non-zero vorticity excluding the surface vortex sheet
Re	Reynolds number
S	Body surface in the transformed plane
S_1	Far field boundary in the transformed plane, used in Appendix A
	Coordinate along body surface, shown in Figure 1

t	Non-dimensional time level
$\bar{t}$	Unit tangential vector at the solid surface, shown in Figure 1
u,v	Cartesian components of velocity vector in the rotating frame of reference
$\bar{v}_\infty$	Free stream velocity as observed in the inertial frame of reference
$\bar{v}$	Velocity vector in the rotating frame of reference
$\bar{v}'$	Velocity vector in the inertial frame of reference
x,y	Cartesian coordinate in physical plane
Z	Complex variable in the physical plane denoting the point (x,y)
α	Angle of Attack
β	Ratio $\Delta x/\Delta y$
β_1	Relaxation factor
γ'	Surface vortex sheet strength in the inertial coordinate system
δ_{ij}	Two-dimensional dirac delta function
ν	Kinematic viscosity
ϕ	Coordinate in the transformed plane
Φ	Scalar velocity potential
ρ	Fluid density, coordinate in the transformed plane
Ψ	Stream function, used in Appendix A
θ	Coordinate in the physical plane
τ	Shear stress
$\bar{\omega}$	Vorticity vector as observed in the rotating frame of reference
$\bar{\omega}'$	Vorticity vector as observed in the stationary frame of reference
ω,ω'	Components of $\bar{\omega}$ and $\bar{\omega}'$ respectively, in the direction perpendicular to the plane of the flow
$\bar{\Omega}$	Angular velocity of the solid

$\dot{\bar{\Omega}}$	Angular acceleration of the solid
ρ	Complex variable in the transformed plane denoting the point (ξ,η)

Infrequently used symbols are locally defined as needed.

Subscripts

t	Denotes components in the tangential direction, at the social surface
i	refers to a grid point in the x-direction
j	refers to a grid point in the y-direction

Superscripts

n	denotes time level
k	denotes iteration level

Operators

$\bar{\nabla}'$	vector del operator in the inertial coordinate system
$\bar{\nabla}$	vector del operator in the rotating coordinate system
$\bar{\nabla}'^2$	Laplacian operator in the inertial coordinate system
$\bar{\nabla}^2$	Laplacian operator in the rotating coordinate system
Δ	indicates an increment

Abbreviations

C_D	Drag coefficient
C_{D_f}	Friction drag coefficient
C_{D_p}	Pressure drag coefficient

C_L	Lift coefficient
C_M	Moment coefficient about quarter chord, nose up moment positive
TE	Trailing edge

CHAPTER I

INTRODUCTION

The study of unsteady flow past airfoils has been a topic of great interest to aerodynamicists for a long time. The available theoretical methods for such a study include linearized potential flow theory, unsteady boundary layer theory and numerical solution of the complete Navier-Stokes equations. These approaches are often complemented by experimental studies.

Linearized potential flow theory has been able to give a great deal of quantitative information in many cases, and a large amount of mathematical research has gone into this particular field of fluid dynamics. Because of its inherent simplicity, linearized potential flow theory has been widely used by aircraft designers even in cases where strong viscous interaction effects may be expected.

With the advent of modern electronic computers, numerical solution of unsteady boundary layer equations has received considerable attention. Since, at low angles of attack, the flow remains attached over most of the upper surface of the airfoil, particularly when the flow is turbulent, there exists a wide class of flows where unsteady boundary layer theory can be successfully employed.

Still there are certain situations where linearized potential flow theory or unsteady boundary layer theory cannot predict the flow

phenomenon in sufficient detail. In the past few years, the study of unsteady separated flow phenomena has received special attention, because an understanding and prediction of these phenomena can lead to appreciable improvement in the performance characteristics and efficiency of many aerodynamic devices such as helicopter blades, marine propellers and compressors. Until recently, wind tunnel and water tunnel experiments have provided the qualitative understanding of these phenomena leading to a large amount of experimental data and empirical relationships. However, rapid developments in the field of computational fluid dynamics now provide an attractive alternative to these empirical approaches.

Numerical treatment of Navier-Stokes equations has rapidly grown in status from an art into a science because of many reasons. Past experience with Navier-Stokes equations for viscous flows past simple body shapes has given valuable information on proper treatment of boundary conditions, choice of numerical schemes, reduction and elimination of numerical errors, etc. In addition, computational fluid dynamics has been able to take advantage of the research activities in related fields of engineering and in many cases borrow efficient numerical schemes from these fields. Furthermore, the availability of faster computers with increased memory capacity and lower computational costs has made direct solution of Navier-Stokes equations an economical proposal, at least for two-dimensional problems.

While the numerical solution itself is of direct value, numerical solution of Navier-Stokes equations can help the industry and research workers indirectly in many ways. For example, research workers have

attempted to study the dynamic stall [1] as a strong inviscid-viscous interaction problem, by patching together the potential flow, boundary layer and Navier-Stokes solutions in various parts of the flow-field. Many assumptions and approximations are made whenever such an approach is used. A direct numerical solution of Navier-Stokes equations can give valuable information for a better treatment of these approximations.

The Kutta-Joukowski condition for unsteady flow over airfoils is not very clear mathematically whenever trailing edge separation occurs. Numerical solution of Navier-Stokes equations can be used to evaluate the reliability and accuracy of the many hypotheses put forth by research workers to handle this problem.

In addition, numerical solution of Navier-Stokes equations can be of immense value to the experimental worker who wants to plan his experiments carefully, and select the flow parameters properly so that the maximum amount of useful information may be obtained from a limited number of experiments.

Because of the above reasons, it is widely recognized that the direct numerical solution of Navier-Stokes equations can be a very valuable tool in the areas of design, development and testing of many modern aerodynamic devices. Much of the research work in the field of computational fluid dynamics is thus centered aroumd numerical solution of Navier-Stokes equations. The research workers, in general, try to develop efficient numerical techniques to handle the following problems.

(1) Reynolds Number Limit: At present, the computational capacity, in general, is restricted to laminar flow at low and moderate Reynolds numbers. Therefore, turbulent flow problems involving separa-

tion are receiving increasingly greater attention [2].

(2) Boundary Conditions: Many research workers use the vorticity-stream function approach to solve the two-dimensional incompressible flow problems, though the velocity-pressure approach still remains an attractive choice for three-dimensional problems. Whenever the vorticity is taken as a dependent variable, the vorticity boundary conditions are not explicitly known in most cases. Even though the physics of the problem is well understood, the actual treatment of the vorticity boundary conditions has been a topic of great interest to research workers, because the reliability and accuracy of any numerical scheme for Navier-Stokes equations critically depend on how the vorticity boundary condition is treated [3].

(3) Arbitrary Body Shape: The problem of arbitrary body shape is peculiar to the Navier-Stokes equations. In the case of boundary layer theory, for example, it is possible to use a set of boundary-fitted orthogonal coordinates without serious errors, provided the surface curvature is not high. Unsteady linearized potential flow theory conventionally makes use of integral equations rather than differential equations, and arbitrary body shape is not a serious problem. However, numerical solution of Navier-Stokes equations for viscous flow past arbitrary body shapes requires the use of special techniques at least in the neighborhood of the body. Some of the approaches used by research workers will be described here briefly.

In order to analyze the phenomenon of static stall, Mehta and Lavan [4] used a conformal relationship to transform the flow field around a Joukowski 9% airfoil, into the interior of a unit circle in

the transformed plane. The governing equations expressed in polar coordinates in the transformed plane were solved using finite difference techniques. Mehta [5] in a subsequent work, has extended the mathematical and numerical formulation to treat dynamic stall as well.

Wu and Sampath [6] have also used similar transformation techniques to solve the governing equations in the transformed plane. The vorticity transport equation was solved using finite difference techniques. The kinematics of the problem was treated using an explicit integral realtionship for stream function in terms of the vorticity field and far field boundary conditions. In addition, Wu and Sampath used a surface vorticity scheme based on the above integral relationship.

Thompson et al [7] have used a curvilinear coordinate system, with one of the coordinate lines coincident with the arbitrary body shape. The governing equations, however, were solved in a rectangular coordinate system in the transformed plane. The coordinates in the physical system were obtained as solutions to a system of elliptic partial differential equations in the transformed (uniform, rectangular) plane, with conveniently chosen boundary nodes in the physical plane providing the necessary boundary conditions.

There have also been numerous attempts to solve the governing equations in the physical plane without the use of any transformation techniques. Kinney [8] used a set of natural coordinates (similar to those used in conventional boundary layer theory) in the physical plane to treat the vorticity transport equation in the physical plane. The velocity field was determined explicitly through an integral relationship for velocity in terms of the vorticity field. The same integral relation-

ship was used to obtain an integral equation for the surface vorticity distribution.

Bratanow and Ecer [9] used a finite element network in the physical plane, and solved the vorticity transport equation as well as the Poisson's equations for velocity and pressure using finite element techniques. The surface vorticity was determined from the stream function values at adjacent nodes using the relationship between vorticity and stream function. In a subsequent work Bratanow et al [10] extended this work with the use of higher order interpolation functions for the stream function ensuring continuity of stream function gradients over the element interface.

(4) Computer Time and Memory Requirements: In contrast to numerical solutions based on potential flow theory and boundary layer theory, a direct numerical solution of Navier-Stokes equations requires several hours on the modern computers for the two-dimensional problem. One reason for this large computer time requirement is the way the kinematics is treated in conventional finite difference schemes. Even though the viscous region is confined to a small region close to the body and the wake, conventional finite difference methods have to treat the large non-viscous region as well and solve for the stream function or velocity in the viscous region and the inviscid region simultaneously. In addition, in order to treat the far field boundary condition with reasonable accuracy, conventional finite difference schemes require a large number of nodes for treating the near field as well as the far field reasonably well. This increases the computer memory and time requirements further.

Thus it is clear that any new approach to the numerical solution

of Navier-Stokes equations must attempt to deal with one or more of the above problems. In the present work, the emphasis is placed on the last three factors.

The method to be presented here has the following features:

(1) An integral representation for velocity in terms of vorticity field and surface velocity boundary conditions is used. This method is available in open literature [11]. This representation is explicit, so that the velocity calculations may be confined to the region of non-zero vorticity. This integral representation satisfies the far field boundary condition exactly. In addition, this representation permits the flow field to be divided into compartments inside which the velocity vector may be evaluated from the vector Poisson's equation for velocity using relaxation techniques.

(2) A new method for the determination of surface vorticity is presented. This method retains global coupling between the outer vorticity field and the surface vorticity field as required by the elliptic nature of the kinematic equations. This method can be used to determine surface vorticity distribution for any specified pitching, transverse and translational motion of the airfoil. This method shares with the integral relationship for velocity, the ability to confine the calculations to regions of non-zero vorticity only. In the case of simple body shapes such as circle and flat plate, this method reduces to the familiar image vorticity technique. In the case of stationary airfoils, this method is conceptually equivalent to the scheme used by Wu and Sampath [6].

(3) For the solution of the vorticity transport equation,

a hybrid finite element-finite difference scheme is proposed and developed in the present work. The vorticity transport equation is solved in the neighborhood of the airfoil using Galerkin's procedure and finite element techniques. This results in a set of ordinary differential equations for the nodal values of vorticity. These equations are integrated in time using an implicit time differencing technique. In the outer field the vorticity transport equation is solved using finite difference techniques, with an implicit time differencing technique for the time derivative. The two regions overlap, so that the nodal values in the overlapping regions act as boundary conditions for the two regions without any interpolation.

The finite element techniques were used to solve the vorticity transport equation near the airfoil because of the inherent flexibility of the finite element method. In addition to giving the numerical solution to the discretized form of vorticity transport equation, the finite element method is actually used to generate these equations. Thus, arbitrary body shape does not present any new problem. In addition, the finite element method has several desirable features from the computer programmer's point of view. It is easier to add nodes or adjust the nodal spacing locally with the finite element method, than with the conventional finite difference techniques. In addition, a variety of of problems--circular cylinder, flat plate, airfoil etc.--may be solved using one computer program and it is only necessary to specify the finite element network geometry in each case.

The major problem that finite element method presents is one of computer memory requirements. Because of the coupling between adjacent

nodes, large banded matrices are formed when Galerkin's procedure is used. Practical considerations related to storage and inversion of these matrices lead to the requirement that the number of nodes be kept low in order to avoid large memory and computational costs. Thus it was decided to use the hybrid scheme, with just sufficient number of nodes in the finite element region to have smooth transition from one region to the other.

In order to test the hybrid scheme, a number of calibration studies were made. These calibration studies indicate that the hybrid scheme can predict accurate and reliable solutions, both in the region close to the body and in the outer region, both for separated and attached flow problems.

The hybrid scheme has been used to study the problem of viscous flow over oscillating airfoils. Thus, the bulk of the mathematical and numerical formulation in the present study has been developed with the oscillating airfoil problem in mind. Whenever the body is stationary, it is only necessary to set the angular velocity to zero.

The mathematical and numerical formulation, the calibration study and the study of viscous flow over oscillating airfoils are described in the following sections.

CHAPTER II

MATHEMATICAL FORMULATION

In this chapter the important mathematical relationships that govern the time history of viscous flow over an arbitrary body undergoing arbitrary pitching motion are presented. The velocity and vorticity boundary conditions are presented and discussed. A new method for the determination of surface vorticity is developed. Finally, the prediction of the aerodynamic loads is outlined. In order to improve readability the derivations of some of the equations used in this chapter are omitted here, and given in the Appendices at the end.

Governing Equations

In the absence of body forces, the Navier-Stokes equations for an incompressible fluid with density ρ and kinematic viscosity ν, may be written in an inertial or fixed coordinate system as follows [12].

$$\frac{\partial \bar{v}'}{\partial t} + (\bar{v} \cdot \bar{\nabla}')\bar{v}' = - \frac{1}{\rho} \bar{\nabla}' p + \nu \bar{\nabla}'^2 \bar{v}' \qquad (1)$$

The equation of continuity in the inertial frame is given by

$$\bar{\nabla}' \cdot \bar{v}' = 0. \qquad (2)$$

Here p is the static pressure, and $\bar{v}'$ the velocity vector as observed in the inertial coordinate system. By inertial frame of reference, we mean a coordinate system that is attached to the body and

undergoes uniform translational motion with the body, but does not rotate with it. In this section, as well as in the following sections, whenever necessary every quantity as observed in the inertial frame of reference is distinguished with a prime, from the corresponding quantity in the rotating frame of reference (to be defined below). In the case of quantities such as pressure, shear stress etc., such a distinction is not necessary since these quantities are independent of the coordinate system. It may be also assumed that at any time t, the two coordinate systems (inertial and rotating) are located such that their corresponding axes coincide. Thus, in many places, the position vectors $\bar{r}'$ and $\bar{r}$ in the inertial and rotating coordinate systems may be used indiscriminately except when derivatives with respect to time or space are involved. In addition, vector operators such as the Laplacian operator appear with a prime whenever the derivatives are evaluated in the inertial frame of reference. With appropriate initial and boundary conditions, equations (1) and (2) may be solved for $\bar{v}'$ and p.

If the body is rotating with an angular velocity $\bar{\Omega}$ and angular acceleration $\dot{\bar{\Omega}}$ where $\bar{\Omega}$ and $\dot{\bar{\Omega}}$ are known functions of time, (and if the body does not undergo any transverse vibrations), it is convenient to consider a rotating of coordinate system that is attached to the body and rotates with it. In this rotating coordinate system, the governing Eqs. (1) and (2) may be reformulated at any point located by the position vector $\bar{r}$ in the following manner [5].

$$\frac{\partial \bar{v}}{\partial t} + (\bar{v} \cdot \bar{\nabla})\,\bar{v} = -\frac{1}{\rho}\,\bar{\nabla}\,p + \nu\bar{\nabla}^2\bar{v} - \dot{\bar{\Omega}} \times \bar{r} - 2(\bar{\Omega} \times \bar{v}) - \bar{\Omega} \times (\bar{\Omega} \times \bar{r}) \qquad (3)$$

$$\bar{\nabla} \cdot \bar{v} = 0 \tag{4}$$

Here $\bar{v}$ is the velocity vector as observed in the rotating coordinate system. For convenience, we assume that in the case of the inertial as well as rotating coordinate system, the point about which the body rotates is taken as the reference point. In the case of airfoils, the quarter chord point has been taken as the reference point in the present study. The velocity vectors $\bar{v}$ and $\bar{v}'$ are related to each other by the following equation.

$$\bar{v} = \bar{v}' - \bar{\Omega} \times \bar{r} \tag{5}$$

It is convenient to define the vorticity vector $\bar{\omega}$ as observed in the rotating coordinate system as follows.

$$\omega = \bar{\nabla} \times \bar{v} \tag{6}$$

The vorticity vector $\bar{\omega}$, the angular velocity $\bar{\Omega}$ and the angular acceleration $\dot{\bar{\Omega}}$ have, for two-dimensional problems, non-zero components only in the direction perpendicular to the plane of motion, and it is sufficient to deal with scalar quantities ω, Ω and $\dot{\Omega}$ from now on. Taking the curl of Eq. (3) term by term we get, for the two-dimensional case,

$$\frac{\partial \omega}{\partial t} + u \frac{\partial \omega}{\partial x} + v \frac{\partial \omega}{\partial y} = \nu \nabla^2 \omega - 2\dot{\Omega} \tag{7}$$

where u and v are scalar components of $\bar{v}$.

The vorticity vector ω', as observed in a stationary frame of reference is given by

$$\omega' = \frac{\partial v'}{\partial x'} - \frac{\partial u'}{\partial y'} \tag{8}$$

It may be shown that ω' is related to ω by the following equation:

$$\omega' = \omega + 2\Omega \tag{9}$$

Using Eq. (9) in Eq. (7) and applying the continuity equation (Eq. (4)), we get

$$\frac{\partial \omega'}{\partial t} + \frac{\partial}{\partial x}(u\omega') + \frac{\partial}{\partial y}(v\omega') = \nu\bar{\nabla}^2\omega' \tag{10}$$

Eq. (10) is commonly referred to as the vorticity transport equation.

The above formulation, given by Eqs. (2), (8) and (10) is known as the velocity-vorticity formulation in literature, and may be solved subject to appropriate boundary conditions.

Velocity Boundary Conditions

The kinematics of the problem, governed by Eqs. (2) and (8) is elliptic in nature, requiring the specification of Neumann, Dirichlet or mixed type of boundary conditions for velocity both at infinity (known as far stream condition) and on the solid surface. It is sufficient to prescribe the Dirichlet type of boundary conditions in the present study in the stationary coordinate system. Eq. (5) may then be used to determine these quantities in a rotating frame of reference whenever necessary. In the stationary coordinate system, the velocity boundary conditions may be written as follows:

$$\begin{aligned} \bar{v}' &= \bar{v}_\infty \text{ at the far stream boundary} \\ \bar{v}' &= \bar{\Omega} \times \bar{r}_B' \text{ on the solid surface} \end{aligned} \tag{11}$$

Integral Formulation for Velocity

As mentioned earlier, Eqs. (2) and (8) completely describe the kinematics, and with Eq. (11) as the desired boundary condition, the velocity vector may be directly determined everywhere in the field, for a specified ω' distribution. However, in the velocity-vorticity formulation presented here, it is desirable to confine the calculations to the region of non-zero vorticity. Wu and Thompson [11] have shown that it is possible to recast the kinematic aspect of the problem as an explicit integral representation for $\bar{v}'$ in terms of the vorticity vector $\bar{\omega}'$ and the associated boundary conditions, in the following manner, for two-dimensional flows.

$$\bar{v}'(\bar{r}',t) = \frac{1}{2\pi} \iint_R \frac{\bar{\omega}_o'(\bar{r}',t) \times (\bar{r}' - \bar{r}_o')}{|\bar{r}' - \bar{r}_o'|^2} \, dR_o + \bar{v}_\infty(t)$$

$$- \frac{1}{2\pi} \oint_B \frac{(\bar{v}_{B_o}' \times \bar{n}_o) \times (\bar{r}' - \bar{r}_o') - (\bar{v}_{B_o}' \cdot \bar{n}_o)(\bar{r}' - \bar{r}_o')}{|\bar{r}' - \bar{r}_o'|^2} \, dB_o \tag{12}$$

Here, $\bar{n}_o$ is the unit normal vector at the surface of the body B, directed away from the solid; R is the region of non-zero vorticity. Since $\bar{v}$, rather than $\bar{v}'$ is used in the vorticity transport equation, Eq. (5) is used to calculate $\bar{v}$ once $\bar{v}'$ is known.

Initial and Boundary Conditions for Vorticity

Eq. (10) is parabolic in time, and it is necessary to prescribe the vorticity field ω' at a reference time level as the initial condition. In the case of impulsively started airfoil, the potential flow

solution is customarily chosen as the initial condition, and the vorticity is zero everywhere except in an infinitesimally thin vortex sheet on the surface. This vortex sheet strength may be determined from the potential flow solution, or directly from the surface vorticity scheme to be discussed in the next section. Once the surface vortex sheet strength is known, this vorticity is redistributed in the first row of cells adjacent to the surface assuming a linear variation inside each cell, to obtain the vorticity at the surface nodes as the initial condition at time level $t=0^+$. This procedure is explained in detail in the next chapter.

In the case of oscillating airfoil problems, it is customary to choose the steady flow solution for a suitable stationary airfoil problem as the initial condition. In the case of stationary airfoils, as well as oscillating airfoils, the initial solution is bound to affect the final solution or the periodic solution very little, because, in the case of viscous flow problems, the effect of initial solution rapidly diminishes with time.

In addition to the initial conditions, the solution of vorticity transport equation requires that the surface vorticity distribution be specified at all time levels. The outer boundary is sufficiently far away from the solid so that the vorticity ω' may be assumed to be zero on this boundary. (This condition will be relaxed later). Wu [3] has shown that ω' on the solid boundary at any time level may be determined from kinematic considerations alone.

The kinematics of the problem requires that the no slip condition be satisfied. That is, the surface vorticity generated at any instance

must, together with the free stream velocity and outer vorticity field, induce zero normal and tangential velocity at the surface in the rotating coordinate system. However, it can be shown that the above condition by itself is not sufficient to determine the surface vorticity distribution uniquely [3]. It is necessary to satisfy, in addition, the condition commonly known as the law of total conservation of vorticity. Therefore, before discussing the actual determination of the surface vorticity distribution, a brief mathematical description of the law of total conservation of vorticity will be presented here.

In Appendix B an expression for the momentum equation in the tangential direction is presented.

$$-\frac{1}{\rho}\frac{\partial p}{\partial s} + \nu\frac{\partial^2 V_t}{\partial n^2} - \dot{\Omega} r^2\frac{d\theta}{ds} + \Omega^2 r\frac{dr}{ds} = 0 \ . \tag{13}$$

Here 'n' is the normal direction, pointed away from the solid. 's' represents the tangential coordinate, defined positive in the counterclockwise sense. V_t is the tangential velocity component defined positive in the counterclockwise sense. At the surface,

$$\omega = \frac{\partial V_t}{\partial n}$$

thus,

$$\frac{\partial^2 V_t}{\partial n^2} = \frac{\partial}{\partial n}\left[\frac{\partial V_t}{\partial n}\right] = \frac{\partial \omega}{\partial n} = \frac{\partial \omega'}{\partial n} \tag{14}$$

Therefore, Eq. (13) may be rewritten as,

$$\nu\frac{\partial \omega'}{\partial n} = \frac{1}{\rho}\frac{\partial p}{\partial s} + \dot{\Omega} r^2\frac{d\theta}{ds} - \Omega^2 r\frac{dr}{ds} \tag{15}$$

We define the total vorticity Q in the entire domain R as follows:

$$Q = \int \omega' \, dR \tag{16}$$

Eq. (10) may be integrated term by term. Using well known vector identities, both the convection term, and the diffusion term may be reduced to line integrals. The far stream boundary gives zero contribution to the line integrals, because the vorticity and its gradient, are zero there. On the solid surface, the line integral corresponding to the convection term vanishes because of no slip condition. Thus we arrive at the following final form.

$$\frac{\partial Q}{\partial t} = -\nu \oint_B \frac{\partial \omega'}{\partial n} \, ds \tag{17}$$

Here B represents the solid boundary. Using Eq. (15) in Eq. (17) we get

$$\frac{\partial Q}{\partial t} = - \oint_B \frac{\partial p}{\partial s} \, ds - \oint_B \dot{\Omega} r^2 \frac{d\theta}{ds} \, ds + \oint_B \Omega^2 r \frac{dr}{ds} \, ds \tag{18}$$

The first term on the right hand side vanishes because p is a single valued function over B. The last term in Eq. (18) vanishes as well, leading to the following simple form.

$$\frac{\partial Q}{\partial t} = - \oint \dot{\Omega} r^2 \frac{d\theta}{ds} \, ds = - 2\dot{\Omega} A$$

Here A is the cross-sectional area of the two-dimensional body. Integrating once in time,

$$Q + 2\Omega A = 0 \tag{19}$$

Eq. (19) is the general form of the law of total conservation of

vorticity, including the rotation of the solid.

Surface Vorticity Determination

As mentioned earlier, we seek a surface vorticity distribution which will satisfy the velocity boundary conditions by Eq. (11), and satisfy, in addition, Eq. (19), the law of total conservation of vorticity.

One such method for the determination of surface vorticity has been developed in the present work. This method is applicable to any two-dimensional closed body, that can be mapped conformally onto a circle of unit radius. The details of the method are presented here. In this method we first determine the velocity $\bar{v}_1$ induced at the surface in the absence of surface vorticity. Then we determine a velocity field $\bar{v}_2$, such that upon superposition, $(\bar{v}_1 + \bar{v}_2)$ satisfies zero normal velocity condition at the surface. The no slip condition, together with Eq. (19) then determines uniquely the surface vorticity.

Consider a given two-dimensional closed body in the physical plane (Z plane) that is mapped conformally onto a unit circle in the ζ plane according to the following transformation.

$$Z = f(\zeta) = f(\rho e^{i\phi}) \tag{20}$$

We also define the scale factor H as follows:

$$H(x,y) = H(\rho,\phi) = \left|\frac{dZ}{d\zeta}\right| \tag{21}$$

We first exclude the surface vortex sheet, and consider the relative velocity between the fluid and the solid, due to contributions

from the free stream velocity, outer vorticity field, and rotation of the body.

$$\bar{v}_1(\bar{r}'_B,t) = \bar{v}_\infty(t) + \frac{1}{2\pi}\iint_{R^-} \frac{\bar{\omega}'_o(\bar{r}'_o,t) \times (\bar{r}'_B - \bar{r}'_o)}{|\bar{r}'_B - \bar{r}'_o|^2} \, dR_o$$

$$-\frac{1}{2\pi}\oint_B \frac{(\bar{v}'_{B_o} \times \bar{n}_o) \times (\bar{r}'_B - \bar{r}'_{B_o}) - (\bar{v}'_{B_o} \cdot \bar{n}_o)(\bar{r}'_B - \bar{r}'_{B_o})}{|\bar{r}'_B - \bar{r}'_{B_o}|^2} \, dB_o$$

$$- \bar{\Omega} \times \bar{r}_B \qquad (22)$$

Here R^- is the fluid domain excluding the surface vortex sheet, and $\bar{n}_o$ is the normal vector at the surface, directed away from the solid. The last term is the velocity of the solid surface, and subtraction of this component in accordance with Eq. (5) gives the relative velocity between the solid and the fluid due to the above factors.

Velocity $\bar{v}_1$ has components v_{n_1} and v_{t_1} defined as follows:

$$v_{n_1} = \bar{v}'_1 \cdot \bar{n}$$

$$v_{t_1} = \bar{v}'_1 \cdot \bar{t} \qquad (23)$$

The unit normal and tangential vectors, as well as the details of the transformation are illustrated in Figure 1.

We now consider a potential flow field $\bar{v}_2$ such that

$$\bar{v}_2 \cdot \bar{n} = v_{n_2} = - v_{n_1} \quad \text{on the solid surface} \qquad (24)$$

Assuming that all the components on the right hand side of Eq. (22) are known, $\bar{v}_1$, v_{n_1} and hence v_{n_2} are known. $\bar{v}_2$ is the solution of the Neumann problem

$$\nabla^2 \Phi_2 = 0 \tag{25}$$

in the physical plane, with the following boundary condition.

$$\frac{\partial \Phi_2}{\partial n} = - v_{n_2} \tag{26}$$

We now use the transformation relationship to solve for Φ_2. The governing equation, along with the boundary conditions are transformed into the following equations in the ζ plane.

$$\nabla_\zeta^2 \Phi_2 = 0 \ . \tag{27}$$

$$\frac{\partial \Phi_2}{\partial n} = \frac{1}{H(1e^{i\phi})} \frac{\partial \Phi_2}{\partial p} = v_{n_2}(\Phi) \tag{28}$$

For the Neumann problem for the exterior of a unit circle, a closed form solution is available and a brief derivation of this solution is presented in Appendix A. According to this solution, at the surface,

$$\frac{\partial \Phi_2}{\partial \phi} = \frac{1}{2\pi} \oint \frac{\sin(\phi - \phi_o)}{1 - \cos(\phi - \phi_o)} \ v_{n_2}(\phi_o) \ H(1,\phi_o) \ d\phi_o$$

Using transformation relations,

$$\frac{\partial \Phi_2}{\partial s} = \frac{1}{H(1,\phi)} \frac{\partial \Phi_2}{\partial \phi} = \frac{1}{2\pi H(1,\phi)} \oint \frac{\sin(\phi-\phi_o)}{1 - \cos(\phi-\phi_o)} \ H \ v_{n_2} \ d\phi_o \tag{29}$$

Now, if the two flow fields $\bar{v}_1'$ and $\bar{v}_2'$ are superposed, then on the surface,

$$v_n = v_{n_1} + v_{n_2} = 0 \ .$$

$$v_t = v_{t_1} + v_{t_2}$$

Thus, the requirement that the solid and fluid have the same normal velocity at the interface is satisfied. The no slip condition requires that a vortex sheet of strength $\gamma_1' = v_t$ be generated at the surface.

Thus γ_1' satisfies the normal and tangential velocity boundary condition. It is also necessary to satisfy the total conservation of vorticity, in its integrated form given by Eq. (19). Using the definition of Q in Eq. (19),

$$\oint_B \gamma_1' \, ds = \oint v_{t_1} \, ds + \oint v_{t_2} \, ds = - 2\Omega A$$

Thus, γ_1', while it satisfies the no slip condition, does not satisfy the law of total conservation of vorticity.

To satisfy the law of total conservation of vorticity, we superpose an additional surface vortex sheet distribution γ_2' on the surface given by

$$\gamma_2' = C/H(1,\phi)$$

It is shown in Appendix A that γ_2' induces zero normal and tangential velocity at the interface, and hence γ_2', which satisfies the homogeneous velocity boundary conditions, is a homogeneous solution to the

Neumann problem, added exclusively for the purpose of satisfying the law of conservation of vorticity.

Then,

$$\gamma_1' = \gamma_1' + C/H(1,\phi) \tag{30}$$

Using Eq. (19), the unknown constant C may be explicitly determined at any time level.

Determination of Loads

Instantaneous pressure and surface shear stress distributions are directly related to the body geometry, angular velocity and angular acceleration of the solid, and surface vorticity and vorticity gradient. Eq. (13) gives the surface pressure distribution as a differential equation. The surface pressure distribution in the present work is calculated with pressure at the trailing edge as reference pressure, and in addition, the pressure is non-dimensionalized with respect to the dynamic pressure at infinity. In addition, all distances are non-dimensionalized with respect to L, the chord length of the body; all velocities are non-dimensionalized with respect to $|\bar{v}_\infty|$; the vorticity and angular velocity are non-dimensionalized with respect to $|\bar{v}_\infty|/L$. Then, Eq. (13) becomes,

$$\frac{\partial C_p}{\partial s} = \frac{2}{Re}\frac{\partial \omega'}{\partial n} - 2\dot{\Omega}r^2\frac{d\theta}{ds} + 2\Omega^2 r\frac{dr}{ds} \tag{31}$$

where

$$C_p = \frac{p - p_{Trailing\ edge}}{\frac{1}{2}\rho v_\infty^2} \qquad \text{and}$$

Re, the flow Reynolds number, is given by

$$Re = |\bar{v}_\infty| L/\nu$$

The shear stress at the surface is given by

$$\tau = \rho \nu \omega'$$

Non-dimensionalizing the shear stress with respect to the dynamic pressure, and non-dimensionalizing ω' as before, we obtain the skin friction coefficient C_f in the following form:

$$C_f = \frac{2}{Re} \omega' \tag{32}$$

Knowing the surface pressure and surface shear stress distribution, other quantities of interest--such as lift, drag and moment about quarterchord, may be directly obtained.

CHAPTER III

NUMERICAL FORMULATION

As mentioned in the introduction this particular method uses a hybrid scheme. The flow field around the body is divided into two regions: (1) a large outer region where the flow field properties vary slowly over space and time, and (2) a small inner region close to the body where the flow properties vary much more rapidly. In this chapter, we describe the numerical treatment of the vorticity transport equation in the inner and outer region. This concept of dividing the flow fields into two regions is illustrated in Figure 2, with a hybrid network used in the study of viscous flows past a Joukowski 12°/. symmetric airfoil. We also discuss the numerical formulation of the integral relationship for the kinematics, and the numerical treatment of the vorticity boundary conditions. Finally, the procedure for calculating the loads on the body is also described.

Treatment of Vorticity Transport Equation in the Outer Region

The outer region is chosen to be of regular shape, with rectangular boundaries that are arranged to coincide with the coordinate lines. The vorticity transport equation is written in finite difference form as follows:

$$\frac{\omega'^{\,n+1}_{i,j} - \omega'^{\,n}_{i,j}}{\Delta t} = A_1 + A_2 + A_3 + A_4 \qquad (33)$$

where

$$A_1 = -\left[(u\omega')^{n+1}_{i+1,j} - (u\omega')^{n+1}_{i-1,j} \right] /2\Delta x$$

$$A_2 = -\left[(v\omega')^{n+1}_{i,j+1} - (v\omega')^{n+1}_{i,j-1} \right] /2\Delta y$$

$$A_3 = \nu\left[\omega^{n+1}_{i+1,j} - 2\omega^{n+1}_{i,j} + \omega^{n+1}_{i-1,j} \right] /\Delta x^2$$

$$A_4 = \nu\left[\omega^{n+1}_{i,j+1} - 2\omega^{n+1}_{i,j} + \omega^{n+1}_{i,j-1} \right] /\Delta y^2$$

In the above equation, the increments in x, yand t are specified by Δx, Δy and Δt respectively. The indices i, j indicate the location of the point while n indicates the time level. The truncation error associated with the time derivative is of order $0(\Delta t)$ and the truncation error associated with the convection and diffusion terms is of order $0(\Delta x^2, \Delta y^2)$.

An assumption regarding the coefficients u and v in the convection terms A_1 and A_2 is made at this point. In order to avoid time-consuming iterations for velocity at time level n+1, the value of u and v at the time level n are used in the calculation of these terms.

Since the outer region and the inner region have nodes common to each other, it is necessary to solve for vorticity values in these two regions simultaneously whenever an implicit time differencing scheme, such as Eq. (33), is used in the outer region. Therefore, we first

discuss the numerical treatment of the vorticity transport equation in the inner region, and vorticity boundary conditions, before considering the methods of solution of the resulting algebraic equations in the outer and inner regions.

Treatment of Vorticity Transport Equation in the Inner Region

In the inner region, the vorticity transport equation is solved using Galerkin's process. The region consists of N_B nodes located on the body surface, N_I points located on the interior of this region and N_o points located on the outer boundary common to the inner and outer regions.

The Galerkin's process may be briefly outlined as follows: Associated with each node j in the finite element region R, there exists a linear interpolation function $N_j(x,y)$ with the property

$$N_j(x_i,y_i) = 0 \qquad i \neq j \tag{34}$$

$$= 1 \qquad i = j$$

Here (x_i,y_i) represents the location of the node i.

Thus, the variation of any flow property such as ω' may be written in terms of these functions, and the nodal vorticity values, as follows:

$$\omega' = \sum_{i=1}^{M} N_i(x,y)\ \omega_i' \tag{35}$$

where

$$M = N_I + N_B + N_o \ .$$

In particular, inside every triangular element with nodes i,j and k,

$$\omega' = \begin{bmatrix} N_i & N_j & N_k \end{bmatrix} \begin{pmatrix} \omega_i' \\ \omega_j' \\ \omega_k' \end{pmatrix} \tag{36}$$

Then, Galerkin's process states that an approximate solution to the vorticity transport equation may be obtained by solving for,

$$\iint_R \left[\frac{\partial \omega'}{\partial t} + \frac{\partial}{\partial x}(u\omega') + \frac{\partial}{\partial y}(v\omega') - \nu \bar{\nabla}^2 \omega' \right] N_j(x,y)\, dR = 0 \ . \tag{37}$$

The above weighting process is applied with interpolation function $N_j(x,y)$ corresponding to each of the N_I interior nodes. A simplification to the above equation is possible. Using the divergence theorem, one can write the diffusion term as,

$$\nu \int \bar{\nabla}^2 \omega' \, N_j \, dxdy = - \nu \int \bar{\nabla}\omega' \cdot \bar{\nabla} N_j \, dxdy + \nu \oint_{\partial R} N_j \frac{\partial \omega}{\partial n} \, dB \tag{38}$$

Here ∂R includes the solid boundary, as well as the boundary common to the inner and outer regions. Since we apply Galerkin's process only with interpolation functions associated with interior nodes, by virtue of Eq.(34) the line integral vanishes. Eq. (37) may now be rewritten as follows (see Appendix D):

$$\int_R \left[\frac{\partial \omega'}{\partial t} N_j + \frac{\partial}{\partial x}(u\omega') N_j + \frac{\partial}{\partial y}(v\omega') N_j + \nu \nabla\omega \cdot \nabla N_j \right] dxdy = 0 \tag{39}$$

The above integral may be written as the sum over all the triangular elements in region R. Since N_j is non-zero only inside those elements that share the node 'j' only these elements contribute to the integral. In evaluating the avove integral, it is assumed that u and v also vary linearly inside each element.

One obtains, as a result of Galerkin's process, a system of N_I first order ordinary differential equations in time for the nodal vorticity values. These N_I equations, involve the nodal values of vorticity at all the M nodes.

$$[H_1]\left\{\frac{d\omega'}{dt}\right\} + [C]\{\omega'\} + [D]\{\omega'\} = \{0\} \qquad (40)$$

Matrices $[H_1]$, $[C]$ and $[D]$ are of order N_I x M. Matrix $[H_1]$ represents the unsteady term, matrix $[C]$ represents the convection term, and matrix $[D]$ represents the viscous term. The above matrices are all sparse, and banded. Only matrix $[C]$, since it depends on velocity values at each time level, varies with time.

Writing Eq. (40) in finite difference form, with use of backward time differencing for the time derivative, and approximating the velocity values used in matrix $[C]$ with the velocity values at time level n, we obtain

$$\frac{1}{\Delta t}[H_1]\{\omega'\}^{n+1} + [C]^n\{\omega'\}^{n+1} + [D]\{\omega'\}^{n+1}$$

$$= \frac{1}{\Delta t}[H_1]\{\omega'\}^n \qquad (41)$$

The matrices on the left hand side of the above equation may be

combined to form a single matrix. Since the vorticity values at the old time level are known, the right hand side of the above equation may be readily evaluated as a column vector:

$$\{E\} = \frac{1}{\Delta t} [H_1]\{\omega'\}^n \tag{42}$$

$$[A]\{\omega'\}^{n+1} = \{E\}^n \tag{43}$$

$[A]$ is a sparse mattix of size N_I x M, and $\{E\}$ is a column matrix of size N_I.

Because of the large size of matrix $[A]$, it is desirable to partition matrix $[A]$ into three submatrices $[A_1]$, $[A_2]$ and $[A_3]$, where $[A_1]$, is of order N_I x N_B, $[A_2]$ is of order N_I x N_I and $[A_3]$ is of order N_I x N_0. Eq. (43) thus becomes,

$$[A_1]\{\omega'\}_B^{n+1} + [A_2]\{\omega'\}_I^{n+1} + [A_3]\{\omega'\}_0^{n+1} = \{E\}^n \tag{44}$$

Vorticity Boundary Conditions

The surface vorticity distribution at any instant may be written in the following matrix form.

$$\{\omega_B'\} = \cos(\alpha(t))\ \{\omega'\}_{B\ \substack{\alpha=0\\ \Omega=0}} + \sin(\alpha(t))\ \{\omega'\}_{B\ \substack{\alpha=90^\circ\\ \Omega=0}}$$

$$+ \Omega(t)\ \{\omega_B'\}_{\Omega=1} + [G]_I\{\omega'\}_I + [G]_0\{\omega'\}_0 + \{F\} \tag{45}$$

Because the kinematics of the problem is governed by linear relationships it is possible to consider the surface vorticity distribution

induced by a number of effects, each effect independent of the other, and superpose these effects to get the final vorticity distribution as shown above. In the above equation, the first and second terms represent known vorticity distributions induced at the surface by the free-stream at zero and 90^{o} angle of attack respectively. The third term on the right hand side represents the surface vorticity induced by the rotation of the solid. Matrix $\{F\}$ represents the surface vorticity induced by the outer field.

Matrix $[G]_I$ contains elements G_{ij} which are influence coefficients indicating the vorticity at surface node i, induced by unit vorticity placed at j, where j is any one of the N_I interior nodes. Matrix $[G]_O$ contains similar influence coefficients G_{ij}, where j is a node on the outer boundary of the finite element region.

The numerical procedure involved in calculating all the above matrices may be briefly explained as follows. Eq. (20) maps the given body onto a unit circle. Once such a transformation (analytical or numerical) is available, the geometric factor H given by Eq. (21) may be evaluated directly.

Each factor on the right hand side of Eq. (45) is considered independent of the others, because superposition is valid as far as the kinematic aspect of the problem is concerned.

First we evaluate the velocity vector $\bar{v}_1$, due to each of the factors. For example, due to free stream velocity at zero angle of attack,

$$\bar{v}_1 = 1\vec{i} \tag{46}$$

Due to free stream velocity at 90^{o} angle of attack,

$$\bar{v}_1 = 1\vec{}_j \tag{47}$$

Due to the rotation of the surface we get the following contribution:

$$\bar{v}_1' = -\frac{1}{2\pi} \oint_B \frac{(\bar{v}_{B_o}' \times \bar{n}_o) \times (\bar{r}' - \bar{r}'_{B_o})}{|\bar{r}' - \bar{r}'_{B_o}|^2} \, dB_o$$

$$+ \frac{1}{2\pi} \oint \frac{(\bar{v}_{B_o}' \times \bar{n}_o) \times (\bar{r}' - \bar{r}'_{B_o})}{|\bar{r}' - \bar{r}'_{B_o}|^2} \, dB_o \tag{48}$$

$$\bar{v}_1 = \bar{v}_1' - \bar{\Omega} \times \bar{y}' \tag{49}$$

Here $\bar{n}_o$ is positive when it is directed away from the solid. $\bar{v}_{B_o}'$ is the velocity of the solid surface.

Velocity $\bar{v}_1$ induced by a unit vorticity placed at a node j is given by,

$$\bar{v}_1 = \frac{1}{2\pi} \int_R \frac{\omega' \bar{k} \times (\bar{r}' - \bar{r}'_j)}{|\bar{r}' - \bar{r}'_j|^2} \, dR \tag{50}$$

where we approximate the vorticity variation in the neighbourhood of node j by

$$\omega' = 1 \, N_j(x,y)$$

In reference 13, analytical integration formulae for Eq. (50) are given, and these expressions may be readily evaluated once the above linear variation is assumed. It is clear that the area integral gets non-zero contribution only from those elements that share node j.

As explained in the mathematical formulation, the objective of the present numerical scheme for surface vorticity is to obtain a surface vorticity distribution that gives zero normal and tangential velocity at the surface relative to the solid, and which, in addition satisfies the law of total conservation of vorticity. The desired vorticity distribution is determined in the following manner:

(1) $\bar{v}_1$, which is the velocity induced at the solid surface by all the above factors (free stream, outer vorticity field and rotation of the solid) is calculated, as explained above.

(2) Once $\bar{v}_1$ is known all over the surface due to each of the factors mentioned earlier, we determine the normal and tangential velocity components as given by Eq. (23). Eq. (24) then gives v_{n_2}. Our next objective is to determine the potential flow field $\bar{v}_2$, and particularly v_{t_2} with v_{n_2} as the prescribed boundary condition. This is done using the explicit closed form solution, given by Eq. (29). The integrand appearing in Eq. (29) has a Cauchy type of singularity at $\phi = \phi_o$. Therefore, in order to accurately evaluate the integral with a proper treatment of the singularity, the following numerical scheme is used.

We first assume the following Fourier Series form for the function Hv_{n_2}.

$$f(\phi) = Hv_{n_2} = \sum_{n=0}^{N} a_n \cos n\phi + \sum_{n=1}^{N-1} b_n \sin n\phi \ . \qquad (51)$$

The coefficients of the above series may be then obtained from the well known relationships connecting $f(\phi)$ and the coefficients. If we define

$$f_\nu = f(\phi_\nu) = f\left((\nu-1)\,\frac{2\pi}{2N}\right)$$

then,

$$a_0 = \frac{1}{2N} \sum_{\nu=0}^{2N-1} f_\nu$$

$$a_\mu = \frac{1}{N} \sum_{\nu=0}^{2N-1} f_\nu \cos \mu\phi_\nu \qquad \mu = 1,2,\ldots, (N-1)$$

$$a_N = \frac{1}{2N} \sum_{\nu=0}^{2N-1} f_\nu \cos N\phi_\nu \tag{52}$$

$$b_\mu = \frac{1}{N} \sum_{\nu=0}^{2N-1} f_\nu \sin \mu\phi_\nu \qquad \mu = 1,2,\ldots, (N-1)$$

(3) Then, from Eq. (29),

$$\gamma_1' = v_{t_1} + \frac{1}{2\pi H(1,\phi)} \oint \frac{\sin(\phi-\phi_o)}{1 - \cos(\phi-\phi_o)}\, v_{n_2}\, H(1,\phi_o)\, d\phi_o$$

$$= v_{t_1} + \frac{1}{2\pi H(1,\phi)} \left[\sum_{n=0}^{N} a_n \oint \frac{\sin(\phi-\phi_o)}{1 - \cos(\phi-\phi_o)} \cos n\phi_o d\phi_o \right.$$

$$\left. + \sum_{n=1}^{N-1} b_n \oint \frac{\sin(\phi-\phi_o)}{1 - \cos(\phi-\phi_o)} \sin n\phi_o d\phi_o \right]$$

$$= v_{t_1} + \frac{1}{H(1,\phi)} \sum_{n=1}^{N-1} (b_n \cos n\theta - a_n \sin n\theta) \tag{53}$$

Detail of the above integration may be found in Appendix C. For

the Joukowski 12 */. airfoil a value of N equal to 90 was used.

(4) Eq. (53) gives the surface vortex sheet strength before vorticity conservation law is applied. For the case of free stream velocity contribution, as well as pure rotation of the solid, Eq. (53) obeys conservation law.

For the case where one determines γ' induced at the surface due to unit vortex at node i, one corrects expression in Eq. (53) for vorticity conservation law, and obtains

$$\gamma' = \gamma_1' + \frac{C'}{H(1,\phi)} = \gamma_1' + \gamma_2' \tag{54}$$

Applying vorticity conservation law for this component alone,

$$Q = \int \omega dR = \oint_B \gamma_2' \, dS + \int_{R-} \omega' dR = 0$$

Since ω' is assumed to vary linearly inside each element,

$$\iint_{R-} \omega' dR = \iint_{R-} N_j(x,y) \, dxdy$$

Also,

$$\int \gamma_2' \, dS = \oint \frac{C'}{H(1,\phi)} \, dS = \oint \frac{C'}{H(1,\phi)} H d\phi = 2\pi C'$$

Thus,

$$C' = -\frac{1}{2\pi} \iint_{R-} N_j(x,y) \, dxdy \tag{55}$$

Once C' is known γ' is known from Eq. (54). Then ω' on the solid boundary is determined by redistributing γ' as a linear vorticity varia-

tion in the first row of elements adjacent to the body surface. In the cases studied using the above method, the first row of elements were assumed to be of uniform height Δn all over the surface, though it is not necessary to assume any such variation. For this special case, one gets,

$$\omega'_B = 2\gamma'/\Delta n \tag{56}$$

This procedure, thus gives in general, a column vector $\{\omega'\}_B$ in terms of other factors as given by Eq. (45).

Solution of the Algebraic Equations in the Outer Field

Because Eq. (33) has to be solved simultaneously at a large number of nodes, it is desirable to resort to iterative techniques for this equation. In the present case the successive point overrelaxation method [14] was used because of its inherent flexibility and simplicity. The numerical procedure involved in the successive point overrelaxation scheme may be outlined as follows:

In Eq. (33), the coefficients of $\omega'^{n+1}_{i,j}$ are collected together. The rest of the terms are moved on to the righthand side. An iteration counter k is added to keep track of the various quantities during the iterations. The resulting equation is divided throughout by the coefficient of ω'^{n+1}_{ij} resulting in the following equation:

$$(\Delta\omega')^{n+1,k+1}_{i,j} = \omega'^{n+1,k+1}_{*i,j} - \omega'^{n+1,k}_{ij}$$

$$(\Delta\omega')^{n+1,k+1}_{i,j} = \frac{1}{D}\left[\omega^n_{ij} + \Delta t(A_5 + A_6 + A_7 + A_8)\right] - \omega'^{n+1,k}_{ij} \tag{57}$$

where, $\omega'^{*n+1,k+1}_{i,j}$ is a first estimate for $\omega'^{n+1,k+1}_{i,j}$ before relaxation, and

$$D = 1 + 2\nu\Delta t\left(\frac{1}{\Delta x^2} + \frac{1}{\Delta y^2}\right)$$

$$A_5 = -\left[(u\omega')^{n+1,k}_{i+1,j} - (u\omega')^{n+1,k}_{i-1,j}\right] /2\Delta x$$

$$A_6 = -\left[(v\omega')^{n+1,k}_{i,j+1} - (v\omega')^{n+1,k}_{i,j-1}\right] /2\Delta y$$

$$A_7 = \nu\left[\omega'^{n+1,k}_{i+1,j} + \omega'^{n+1,k}_{i-1,j}\right] /\Delta x^2$$

$$A_8 = \nu\left[\omega'^{n+1,k}_{i,j+1} + \omega'^{n+1,k}_{i,j-1}\right] /\Delta y^2$$

Then,

$$\omega'^{n+1,k+1}_{i,j} = \omega'^{n+1,k}_{i,j} + \beta_1(\Delta\omega')^{n+1,k+1}_{i,j} \qquad (58)$$

Where β_1 is a relaxation parameter. In the case of viscous flow over a Joukowski 12°/. airfoil, a value of β_1 equal to .2 was used.

Since the vorticity transport equation must be solved in the inner and outer regions simultaneously, at the end of each iteration in the outer field, the nodal values of vorticity on the common boundary are taken as the boundary conditions for the inner region.

Solution of the Algebraic Equations in the Inner Field

At any given time level, and for a given iteration level k, since the instantaneous angle of attack $\alpha(t)$, angular velocity $\Omega(t)$ and the vorticity field $(\omega')^{n+1,k+1}$ are known, in Eq. (45), the first, second, third and sixth terms on the righthand side may be directly evaluated. In addition, since the vorticity on the outer boundary of the finite element region is also known from the finite difference scheme calculations, at any given iteration level k+1, the fifth term may also be evaluated. Thus, Eq. (45) becomes,

$$\{\omega'\}_B^{n+1,k+1} = [G]_I\{\omega'\}_I^{n+1,k+1} + \{R\}^{n+1,k+1} \tag{59}$$

where

$$\{R\}^{n+1,k+1} = \cos(\alpha(t))\{\omega'\}_{\substack{B\alpha=0\\ \Omega=0}} + \sin(\alpha(t))\{\omega'\}_{\substack{B\alpha=90^o\\ \Omega=0}}$$

$$+ \Omega(t)\{\omega'\}_{B_{\Omega=1}} + [G]_I\{\omega'\}_I + \{F\}$$

Similarly, Eq. (44) may be rewritten, incorporating the iteration counter as follows:

$$[A_1]\{\omega'\}_B^{n+1,k+1} + [A_2]\{\omega'\}_I^{n+1,k+1} = \{E_1\} \tag{60}$$

where $$\{E_1\} = \{E\}^n - [A_3]\{\omega'\}_0^{n+1,k+1} \tag{61}$$

Using Eq. (59) in Eq. (60) we get,

$$\left[[A_1][G]_I + [A_2]\right]\{\omega'\}_I^{n+1,k+1} = \{E_2\} \tag{62}$$

where,

$$\{E_2\} = \{E_1\} - [A_1]\{R\}^{n+1,k+1} \tag{63}$$

In Eq. (62) the coefficient matrix is a N_I x N_I square matrix, and it is, in general, not sparse or banded because $[G]_I$ is a full matrix. For moderately small values of N_I, a direct inversion is both efficient and economical. So Eq. (62) is solved using direct inversion to obtain $\{\omega'\}_I^{n+1,k+1}$. Then Eq. (59) is used to determine $\{\omega'\}_B^{n+1,k+1}$.

Sequence of Calculations Involved in Solution of the Vorticity Transport Equation

The calculations for the vorticity field are performed in the following sequence. One assume that the velocity field and vorticity field at a reference time level n are given as initial conditions. Since the velocity lags by one time step, it is not necessary to iterate for velocity also during this sequence of calculations.

For the first iteration, i.e. for k=1, we assume that

$$\omega_{i,j}'^{n+1,1} = \omega_{i,j}'^{n} \qquad \text{in the outer field.}$$

1. Using Eqs. (57) and (58) we sweep through the outer field once, and obtain $\omega_{i,j}'^{n+1,k+1}$. These calculations are also performed for the boundary nodes located on the common boundary for the inner and outer regions. Thus $\{\omega'\}_0^{n+1,k+1}$ is known. The calculations of $\{\omega'\}_0^{n+1,k+1}$ makes use of nodal vorticity values in the overlap region.

2. The matrix $\{R\}^{n+1,k+1}$ in Eq. (59) and the matrices $[G]_I$ and $[G]_0$ are in Eq. (45) are evaluated. Since $[G]_I$ and $[G]_0$ consist of geometric coefficents independent of time level or the iteration counter,

they are calculated only once during the calculations.

3. Matrices $[A_1]$, $[A_2]$ and $[A_3]$ in Eq. (44) are calculated from the Galerkin's process, along with the column matrix $\{E\}^n$ in Eq. (43). Since these matrices depend only on the time level, and not on the iteration counter, they have to be obtained only once for each time level. Matrix $\{E_1\}$ from Eq. (61) and $\{E_2\}$ from Eq. (63) are also determined.

4. Eq. (62) is solved through direct inversion, for $\{\omega'\}_I^{n+1,k+1}$. These values are used in Eq. (59) to determine $\{\omega'\}_B^{n+1,k+1}$. Since the inner and outer regions overlap, at the nodal positions positions in the overlapping region, the vorticity determined acts now as the boundary condition for the outer region when returning to Step 1.

5. Steps 1, 2, 3 and 4 are repeated as many times as needed until the desired convergence is achieved. In the case of viscous flow over Joukowski 12°/. airfoil the following convergence criterion was used.

$$|\omega_B'^{n+1,k+1} - \omega_B'^{n+1,k}| \leq .005 \qquad (64)$$

for all nodes on the surface.

An Explicit Scheme for the Vorticity Transport Equation

In the earlier stages of work, during the calibration of this present scheme using the study of viscous flow over a flat plate as the test case, an explicit numerical scheme was used in the outer field. Whenever explicit schemes are used in the outer field, the solution for

vorticity in the outer field is determined once and for all. Thus no iterations are involved. For the sake of completeness, the finite difference formulae used will be given here:

$$\frac{\omega'^{n+1}_{i,j} - \omega'^{n-1}_{i,j}}{2\Delta t} = A_1 + A_2 + A_3 + A_4 \tag{65}$$

where

$$A_1 = -\left[(u\omega')^n_{i+1,j} - (u\omega')^n_{i-1,j}\right]/2\Delta x$$

$$A_2 = -\left[(v\omega')^n_{i,j+1} - (v\omega')^n_{i,j-1}\right]/2\Delta y$$

$$A_3 = \nu\left[\omega^n_{i+1,j} - \omega^{n-1}_{i,j} - \omega^{n+1}_{i,j} + \omega^n_{i-1,j}\right]/\Delta x^2$$

$$A_4 = \nu\left[\omega'^n_{i,j+1} - \omega'^{n-1}_{i,j} - \omega'^{n+1}_{i,j} + \omega'^n_{i,j-1}\right]/\Delta y^2$$

It is seen that the viscous terms are represented by the Dufort-Frankel scheme [14]. The above equation has the following stability criterion [14].

$$\left|\frac{u\Delta t}{\Delta x}\right| + \left|\frac{v\Delta t}{\Delta y}\right| \leq 1 \tag{66}$$

The Dufort-Frankel scheme was found to be very good for all the test cases considered. But the stability criterion permits very small time steps only. In most of the cases studied in the present work, the

implicit scheme allows the time step based on free stream velocity and chord to be as high as .1, while the explicit scheme allows the maximum value of Δt to be less than .025. The implicit schemes, however, because of the iterations involved and the resulting increase in the number of arithmetic operations, require twice as much central processor unit time (CPU) compared to the explicit scheme. As a result, taking into account the time step as well as the CPU time per time step, the implicit scheme is found to be at least twice as fast as the explicit scheme in the present formulation. Therefore, it was decided to use the implicit time differencing scheme in the outer field in the later studies.

Determination of Velocity

Determination of the Velocity Field in the Inner Region. In the inner region, the vorticity field is assumed to vary in the following manner.

$$\omega' = \Sigma N_j(x,y)\ \omega_j(t) \tag{67}$$

Here $N_j(x,y)$ is a linear interpolation function with properties given by Eq. (34).

The solid boundary moves with a velocity given by Eq. (11). Knowing the velocity of the solid boundary, the line integral contribution from Eq. (12) may be readily found. In the present study, since the nodes on the surface are placed non-uniformly, trapezoidal rule is used to evaluate the line integral. Using the analytic integration formulae given in Reference(13), for vorticity distribution of the form given by Eq. (67), the contribution of the inner region vorticity to the

nodes in the inner region may be found.

The vorticity in the outer field varies very slowly. So, for the purpose of calculating the velocity contribution from the outer field to a node 'k' in the inner region, the area integral is approximated in the following manner.

From the rectangular cells in the outer field, the following contribution is obtained.

$$\iint \frac{\omega'\bar{k} \times (\bar{r}'_k - \bar{r}'_o)}{|\bar{r}'_k - \bar{r}'_o|^2} \, dR_o = \sum_{ij} \sum \iint \frac{\omega'\bar{k} \times (\bar{r}_k - \bar{r}'_o)}{|\bar{r}'_k - \bar{r}'_o|^2} \, dR_o$$

$$= \sum_{ij} \sum A_{ij,k} \bar{\bar{\omega}}'_{i,j} \Delta x \Delta y \qquad (68)$$

where

$$\bar{\bar{\omega}}'_{i,j} = \left(\omega'_{i,j} + \omega'_{i+1,j} + \omega'_{i,j+1} + \omega'_{i+1,j+1}\right)/4$$

$$A_{ij,k} = \left[\frac{(x_k - \bar{x})\vec{j} - (y_k - \bar{y})\vec{i}}{(X_k - \bar{X})^2 + (y_k - \bar{y})^2}\right]$$

and

$$\bar{x} = \left(x_{i,j} + x_{i+1,j} + x_{i,j+1} + x_{i+1,j+1}\right)/4 \, .$$

$$\bar{y} = \left(y_{i,j} + y_{i+1,j} + y_{i,j+1} + y_{i+1,j+1}\right)/4 \, .$$

Determination of Velocity in the Outer Field

During earlier stages of the present work, the velocity field in the outer field was calculated using the integral expression for velocity, given by Eq. (12). The method of calculating the area integrals, and

line integrals was similar to the method used for the inner field as described in the previous section.

The advantage of using Eq. (12) to calculate exterior flow problems stems from its explicit nature. Thus, the integral formulation permits determination of velocity on the boundaries of rectangular regions without regard to the interior nodes. In several cases, since rapid computational schemes are available to solve the Poisson's equation in regions with rectangular boundaries, a combination of Eq. (12), and such schemes will provide a faster means of computing velocities in the case of exterior flow problems. For this reason, it was decided to use Eq. (12) only for the boundary nodes of the outer region, and then use successive overrelaxation techniques to solve the finite difference formulation of the Poisson's equation.

At the far field boundary (located sufficiently far away from the body so that both ω' and $\frac{\partial \omega'}{\partial x}$ are zero), the velocity is specified using Eq. (12). At the common boundary, the velocity components are again specified from Eq. (12). In the outer region domain, the following equations need to be solved:

$$\frac{\partial^2 u}{\partial x^2} + \frac{\partial^2 u}{\partial y^2} = - \frac{\partial \omega'}{\partial y} \tag{69}$$

$$\frac{\partial^2 v}{\partial x^2} + \frac{\partial^2 v}{\partial y^2} = \frac{\partial \omega'}{\partial x} \tag{70}$$

Using central difference schemes to represent the derivatives in the above two equations, one obtains,

$$\Delta u = \frac{1}{2(1+\beta^2)}\left[\frac{\omega^n_{i,j+1} - \omega^n_{i,j-1}}{2\Delta y}\,\Delta x^2 + u^{n,k}_{i-1,j} + u^{n,k}_{i+1,j}\right.$$

$$\left. + \beta^2\left(u^{n,k}_{i,j+1} + u^{n,k}_{i,j-1}\right)\right] - u^{n,k}_{i,j}$$

$$\Delta v = \frac{1}{2(1+\beta^2)}\left[-\frac{\omega_{i+1,j} - \omega_{i-1,j}}{2\Delta x}\,\Delta x^2 + v^{n,k}_{i-1,j} + v^{n,k}_{i+1,j}\right.$$

$$\left. + \beta^2\left(v^{n,k}_{i,j+1} + v^{n,k}_{i,j-1}\right)\right] - v^{n,k}_{ij} \qquad (71)$$

where $\beta = \frac{\Delta x}{\Delta y}$. The subscripts (i,j) denote geometric location as before, n is the time level and k is the iteration counter. Then,

$$u^{n,k+1}_{i,j} = u^{n,k}_{i,j} + \beta_1 \Delta u \qquad (72)$$

$$v^{n,k+1}_{i,j} = v^{n,k}_{i,j} + \beta_1 \Delta v \qquad (73)$$

where β_1 is the relaxation factor. In the case of viscous flow over a Joukowski 12°/. airfoil, a value of $\beta_1 = 1.8$ was used.

Calculation of Loads

Eq. (31) defines the surface pressure distribution with reference to the pressure at the trailing edge. The polar coordinates (r,θ) are related to the Cartesian coordinates (x,y) in the following manner:

$$\theta = \tan^{-1}\frac{y}{x} \qquad r = \sqrt{x^2 + y^2} \tag{74}$$

Thus, $$d\theta = \frac{-ydx + xdy}{x^2 + y^2} \qquad rdr = vdx + ydy \tag{75}$$

Thus Eq. (31) becomes,

$$C_p = -2\left[-\int_o^s \frac{1}{Re}\frac{\partial\omega'}{\partial n}ds + \dot{\Omega}\int_o^s x\,dy - ydx + \Omega^2\left(r_s^2 - r_o^2\right)\right] \tag{76}$$

where $r_s = \sqrt{x_s^2 + j_s^2}$ and $r_o^2 = x_{T.E.}^2 + y_{T.E.}^2$

Here the subscript 'T.E.' stands for the trailing edge. The derivative $\frac{\partial\omega'}{\partial n}$ is evaluated using first order one-sided formulae. The integrations are performed using trapezoidal rule.

The skin friction is directly determined from Eq. (32).

Once the surface pressure and shear stress distribution are known, the loads are obtained from the following expressions.

$$C_L = \oint_B C_p \frac{dx}{ds}ds + \frac{2}{Re}\oint_B \omega' \frac{dy}{ds}ds \tag{76}$$

$$C_{D_p} = -\oint_B C_p \frac{dy}{ds}ds$$

$$C_{D_f} = \frac{2}{Re}\oint_B \omega' \frac{dx}{ds}ds$$

$$C_M = - \oint_B C_p \left[x \frac{dx}{ds} + y \frac{dy}{ds} \right] ds$$

$$- \frac{2}{Re} \oint_B \omega' \left[- y \frac{dx}{ds} + x \frac{dy}{ds} \right] ds \qquad (78)$$

In all the above expressions s increases in the counter clockwise sense. It is clearly shown that the terms in which $\frac{\omega'}{Re}$ appears , give the shear stress contribution to loads, while terms in which C_p appears give the pressure contribution to the above loads. Here C_{D_p} represents the viscous drag and C_M represents the moment coefficient about the quarter chord, which is also the pitching axis for the oscillating airfoil problem. Nose up moment has been assumed to be positive in the present study. Here, C_L and C_D are calculated as force components normal to, and along the airfoil chord. This definition differs from the conventional definition based on wind axes.

CHAPTER IV

PRELIMINARY INVESTIGATIONS

In order to evaluate the accuracy of the present method and demonstrate its ability to treat attached flow as well as separated flow problems, this method has been applied to two classical test cases. In this chapter, the numerical results for these two test cases are presented. In addition, this new method has been applied to the study of viscous flow past a Joukowski 12'/. airfoil at selected angles of attack, and the results of this study are also presented here.

Calibration Studies

Case 1. Viscous Flow Past a Finite Flat Plate at Zero Angle of Attack. (Reynolds Number = 1000.). The inner region finite element network for this problem is shown in Figure 3. A relatively coarse mesh has been used, with $\Delta x = .1L$ and $\Delta y = .04L$. There are 114 nodes with 20 nodes on the upper and lower surfaces of the flat plate and 168 triangular elements. It may be noted that in this problem, as well as in the subsequent cases, Δy is kept lower than Δx, because the flow properties vary much more rapidly in the y-direction than in the x-direction. The outer region is represented by 1250 nodes spaced uniformly, also with $\Delta x = .1L$ and $\Delta y = .04L$. The downstream boundary of the outer field is located at a distance 3.4 chord lengths from the trailing edge. The upstream boundary is located at a distance 0.5 chord length from the

leading edge. The two lateral boundaries of the outer field are also located 0.5 chord length from the flat plate.

In the outer field, the vorticity transport equation is treated using Dufort-Frankel scheme as discussed in Chapter III. A constant value of time step equal to .04 is used. The calculations are performed up to a time level of 2.4. Here, the time level, as well as the time step has been non-dimensionalized with respect to the ratio between chord length L and free stream velocity $\bar{v}_\infty$.

In the inner region, the vorticity has been assumed to vary linearly inside each triangular element. Exact analytical integration techniques, as discussed in Chapter III, are used to evaluate the area integrals in the surface velocity and surface vorticity calculations. In the present case, because of symmetry conditions, at the surface of the flat plate v_{n_1} and v_{n_2} become zero. Thus the surface vorticity gets contribution only from v_{t_1}. (Here, v_{n_1} is the normal velocity induced on the plate by the outer vorticity field, and v_{n_1} is clearly zero because the flow is symmetric about the flat plate). v_{t_1} represents the tangential velocity at the flat plate due to free stream velocity, vorticity in the upper half of the flow field, and vorticity in the lower half of the flow field. Thus, for the flat plate case, the present scheme is equivalent to the familiar image vorticity technique.

Extensive numerical experiments have been performed to study the effect of time step, as well as choice of integration technique. The system of simultaneous ordinary differential equations, obtained from the Galerkin's process, may be integrated in many ways. Some of the popular methods are (1) Crank-Nicholson method [14]; (2) Fully implicit

scheme (explained in Chapter III); (3) Time Element scheme, where the vorticity is assumed to vary linearly inside time elements, and the Galerkin's process is applied both in space and time, and (4) Runge-Kutta methods. In order to study the effect of integration technique on the numerical solution, the following experiment was performed.

In Table 1, the vorticity values at selected locations in the flow field are shown at a time level of .4. These calculations were performed with a time step equal to .02, with the solution at $t=0^+$ following the impulsive start as the initial solution. During the impulsive start, the free stream velocity changes from zero at $t=0$ to $\bar{v}_\infty$ at $t=0^+$, and the potential velocity distribution everywhere is the initial condition. Table 1 indicates that the numerical solution obtained using Crank-Nicholson scheme agrees up to three significant digits with the results obtained using the fully implicit scheme. Thus it is clear that the numerical solution is relatively insensitive to the choice of integration technique.

Table 1. Effect of Integration Technique on Numerical Results for Vorticity

Node	1	2	3	4	5	6	7
Crank Nicholson	-20.96	-15.69	-18.68	-17.44	-18.61	-18.70	-18.16
Fully Implicit	-20.19	-15.95	-18.40	-17.45	-18.46	-18.57	-18.19

The time development of the vorticity profile at mid profile is shown in Figures 4 and 5, and compared with the results obtained by Sampath [15]. The results of Sampath have been chosen, because of the

many similarities that exist between the way Sampath treated the kinematics of the problem, and the present scheme. Sampath used the integral representation for velocity, and used a scheme that is conceptually equivalent to the present method to determine the surface vorticity. The main difference between the two schemes is the way the vorticity transport equation is treated. Sampath used the alternate direction implicit scheme to integrate the finite difference form of the vorticity transport equation. His calculations were performed with a somewhat finer grid ($\Delta y = .02$, as opposed to $\Delta y = .04$ in the present work).

Immediately following the impulsive start, the boundary layer is very thin all over the surface, and the present grid does not represent the boundary layer adequately at the early time levels. Thus some difference exists between the two results, expecially near the surface for early time levels. However, at later time levels the agreement is quite good (for $t \geq 1.0$).

In Figure 6, the velocity profile at mid-plate, as calculated using the present method is compared with Blasius solution. Both Reference 15 and the present results show an overshoot in the velocity profile, leading to velocities higher than the free stream velocity at some points in the boundary layer. Such an overshoot is expected, and is due to the favorable pressure gradient along the surface caused by displacement thickness effect.

One of the main conclusions to be drawn from the present case is that the present scheme can give an accurate solution even with a relatively coarse mesh. This accuracy is achieved by the use of analytical integration techniques for velocity and surface vorticity.

Secondly, the hybrid scheme does not generate any additional difficulties at the common boundary. The flow properties are found to vary smoothly across the boundary between the inner and outer region, even though the matching is performed very close to the body surface at ($\frac{y}{L}$ = .12).

Case 2. Viscous Flow over a Cylinder (Re = 40). The present scheme has been applied to the study of viscous flow over a circular cylinder at Reynolds number 40. This classical test case was chosen to demonstrate the ability of the present scheme to handle flows with strong separation.

The computational domain is divided into an inner (finite element) region and an outer region. The inner region consists of 200 nodes, including 40 nodes on the surface, and 320 elements. The outer region is well represented by approximately 1200 nodes. The two regions are matched at distance 0.32 radius away from the surface. The far field boundary is located 21.6 radii away from the surface. In the θ direction the grid spacing is equal to $\frac{\pi}{20}$. In the radial direction, the following variation is assumed, both in the inner and the outer regions.

$$r = e^{\xi} \qquad ; \qquad dr = e^{\xi} d\xi .$$

By varying ξ uniformly, with $\Delta\xi$ = .08, an exponential variation is obtained. The first set of nodes are located approximately .08 radius away from the cylinder surface. The inner finite element grid, as well as the outer grid is oriented such that the finite element-finite difference network is symmetric about the flow axis. However no symmmetry has been assumed regarding the flow properties.

In the outer region, the time derivative is approximated by a two point backward difference formula. In addition, because of the geometry, in the outer field the vorticity transport equation was solved in polar coordinates. In the inner region Cartesian coordinates were used, because the curvature of the body does not affect the numerical formulation of the finite element method.

The time step was varied gradually from .05 to .25 for the present calculations. At the earlier time levels, the lower value of Δt was necessary because the flow properties were changing very rapidly following the impulsive start. The computations were terminated when a non-dimensional time level (based on circular cylinder radius and free stream velocity) equal to 20.9 was reached. At this time level, the drag coefficient had converged up to three significant digits.

In Figure 7, the surface pressure distribution at this time level is compared with the solution obtained by Grove et al [16]. The agreement is quite good over most of the surface.

In addition to the experimental results for viscous flow over circular cylinder at low Reynolds numbers, a large volume of research work based on finite difference techniques is available in literature. The present results are compared with the available data in Table 2; θ_{sep} represents the angle at which the flow separates measured from the rear-axis, and it is obtained in the present study as the point on the surface where the surface vorticity changes sign. $\phi_{pr.min}$ represents the point on the cylinder surface where the surface pressure coefficient reaches a minimum value. The length of the standing vortices, $\frac{L_I}{R}$ as presented in Table 3 represents the distance between the center of the

Table 2. Comparison of Present Results with Other Results for Viscous Flow over a Circular Cylinder (Re = 40)

	Kawaguti (Ref. 17)	Apelt (Ref. 18)	Kawaguti and Jain(Ref. 19)	Jain & Raw (Ref. 20)	Present
C_D	1.618	1.496	1.529	1.594	1.705
C_{D_p}/C_D	0.65	0.62	0.655	0.657	0.67
Length of Standing Vortex L_1/R	4.5	5.27	6.03	6.3	4.01
θ_{sep}	52.5^o	50^o	53.7^o	52.7^o	53.2^o
$\phi_{pr.min}$	87^o	96^o	89^o	85.7^o	90^o
ω'_{min}	-6.15	-6.28	-5.985	-5.985	-6.09
Ψ'_{min}	- .025	- .034	- .04	- .04	- .025

cylinder, and the point on the center line where the velocity changes sign. Here R represents the circular cylinder radius. Ψ_{min} represents the minimum value of stream function, found inside the separation bubble.

It is seen that the present solution is in good agreement with the finite difference solutions, as shown in Table 2. In particular, the present scheme predicts the flow properties on the surface, and near the surface-- ζ_{min}, ϕ_{min}, θ_{sep} and Ψ_{min}--in very good agreement with the finite difference solutions.

For the purpose of plotting the stream lines, it is necessary to calculate the stream function in a small region near the circular cylinder. This is done in the following manner. Knowning u and v, the Cartesian components of the velocity vector, the polar components v_r and v_θ are determined first.

$$v_r = u \cos\theta + v \sin\theta$$

$$v_\theta = v \cos\theta - u \sin\theta$$

Here v_r is considered positive outward, and v_θ is considered positive in the counter clockwise sense, and θ is also measured in the counter clockwise direction from the flow axis. Based on the definition of stream function,

$$\frac{\partial \Psi}{\partial r} = - v_\theta .$$

Thus Ψ can be found along each radial line by integrating the above equation along the radial direction numerically. It is also assumed in these calculations that the stream function is zero at the surface.

In Figure 8, the streamlines, and constant vorticity lines are shown at the time level t=20.9 on the upper and lower halves of the figure respectively. The common boundary for the inner and outer region is also shown as a dotted line. It is noted that the results show no abnormal behavior (kinks or wiggles) near this boundary. Thus it is clear that the present method allows a smooth transition from one numerical scheme to another even in flows with strong separation.

It is also of interest to note that the constant vorticity contours show islands and zig-zag lines far away from the surface. These lines represent spurious vorticity of order $0(10^{-2})$. The spurious vorticity is generated by two sources; (1) the coupling between the nodal values of vorticity, as produced by the finite element scheme, produces small spurious vorticity following impulsive start. With time this vorticity is convected out of the finite element region. (2) The representation of the convective terms in the vorticity transport equation with central difference formulae produces spurious convection effects, because central differencing schemes depend both on the upstream properties and downstream properties, while in reality only the upstream properties affect convection.

This spurious vorticity is small in magnitude, and appears only at large distances from the body. Thus it does not affect the accuracy of the solution to any extent.

Viscous Flow Over Stationary Airfoils

The two cases considered so far indicate that the present method can produce solutions comparable in accuracy to other finite difference

and integro-differential schemes. The real potential of the present method is however realized only for arbitrary bodies, because conventional finite difference and integro-differential schemes can not be directly used to solve the governing equations in the physical plane for arbitrary bodies. In order to demonstrate the ability of the present method to treat viscous flow problems involving arbitrary bodies with equal ease, we consider two cases involving viscous flow over Joukowski 12%. airfoils.

The surface vorticity scheme developed in Chapter II requires a convenient analytical or numerical scheme that will map the given arbitrary shape onto a unit circle in the ζ-plane conformally. Computationally efficient and accurate numerical procedures are available in literature [21] for this purpose. However, in the present case, since a convenient analytical transformation is available, it is not necessary to resort to numerical techniques. The transformation relationship used in the present study is given by

$$Z = \frac{1}{3.63}\left[\zeta - .0753423 + \frac{.81278}{\zeta - .0753423}\right]$$

The above relationship produces a 12%. symmetric Joukowski airfoil with rounded trailing edge.

Even though the present method can be used to treat viscous flow problems at high angles of attack, the angle of attack is kept low in the two cases to be discussed here. This is done in order to get some insight into the properties of the flow from the potential flow theory

and boundary layer theory. While the numerical results are of value by themselves, their usefulness is further increased by the fact that the steady state results can be directly used as the starting solution for the oscillating airfoil problem.

Case 1. Joukowski 12°/. Airfoil at Zero Angle of Attack, (Re = 400.)

For this study, the finite element network shown in Figure 2 is used. The network consists of 232 nodes including 48 nodes on the surface of the airfoil, and 354 triangular elements. The first set of nodes away from the surface are located .01 chord away from the surface. The outer flow field has approximately 2500 nodes. Because of the low time levels considered, the vorticity at the downstream boundary is set to zero. In the outer field, explicit Dufort-Frankel scheme is used. The time step is varied from .0025 to .02 gradually during the course of computations. The time steps and the time levels shown here are all non-dimensionalized with respect to the ratio between the chord length and free stream velocity.

The numerical results obtained for the zero angle of attack case show all the important features of the viscous flow over an impulsively started airfoil. Immediately following the impulsive start, the vorticity distribution everywhere on the surface is very high. In addition, the impulsive start produces large pressures near the leading edge, and favorable pressure gradients all over the surface. As a result, both the pressure drag and the viscous drag values are very high after the impulsive start. Figure 9 shows the variation of the total drag during the time period: $0^{+} < t < .06$. It is seen that the total drag coeffi-

cient decreases at first rapidly, and then slowly, as the transient effects begin to die down. The numerical results indicate that the pressure drag is very high compared to the viscous drag immediately after the impulsive start. However, at later time levels, the pressure drag decreases much more rapidly than the viscous drag. Thus the viscous drag is the major contributor to the total drag. This was found to be the pattern for all the moderate Reynolds number flow problems considered in this study.

Figure 10 presents the variation of drag at later time levels ($.06 < t < .9125$). It is observed that the drag coefficient at t=.9125 is varying very slowly. The numerical results show that the drag coefficient at t=.9125 is varying only in the third digit.

Figure 11 describes the surface vorticity distribution at selected time levels. At t=.1925, it is seen that the surface vorticity values are very high. The vorticity everywhere decreases with time; but aft of the quarterchord point, the decrease in vorticity is much more noticeable than near the leading edge region.

The surface pressure distribution is shown in Figure 12 at selected time levels. It is seen that at t=.1925, the pressure gradient is still favorable all over the surface, indicating that the impulsive start effects are still dominant at this time level. However, with the development of the flow, the viscous effects lead to the development of an adverse pressure gradient on the surface, as seen in Figure 12 at time levels t=.5925 and t=.9125. It is also observed that the variation in the pressure distributions between the time levels t=.5925 and t=.9125 is small; thus, the flow is asymptotically approaching a

steady state solution at these time levels.

The adverse pressure gradient on the surface is not strong enough to produce separation at this Reynolds number. At this Reynolds number, the viscous displacement effect aft of midchord is appreciably high. Thus the pressure distribution on the surface is considerably different from the pressure distribution predicted by the potential flow theory. Boundary layer theory predicts separation, because it is based on the potential flow theory. However, many investigators [3] have observed that no appreciable separation occurs until the Reynolds number is sufficiently high (Re $\simeq$ 5000 or higher).

Case 2. Joukowski 12%. Airfoil at 3° Angle of Attack (Re = 1000.)

For this case, the finite element network used is the same as in the previous case. However, the following modifications are made with regard to the computations in the outer field.

(1) About 1250 new nodes are added to the outer region, so that the outer field now contains approximately 3750 nodes. As a result, the lateral boundaries of the outer field are now located approximately .625 chords away from the surface. The upstream boundary is now located .9 chord away from the leading edge.

(2) In the outer field, the vorticity transport equation is solved using the fully implicit time-differencing scheme described in Chapter III. It was observed that the implicit scheme, because of the number of iterations required to converge, requires longer computer time per time step. However, the value of Δt chosen is large enough to offset this disadvantage. Thus, fewer number of time steps, and lower

computer time are required to reach a desired time level. The choice of the time step is now governed exclusively by accuracy considerations.

During earlier time levels, immediately following the impulsive start, a value of Δt equal to .01 is used in the computations. While lower values of Δt than the above value would produce better resolution of the flow immediately after the impulsive start, this value of Δt is good enough in the present case, where we are interested more in the steady state solution. This value of Δt is slowly increased during subsequent stages of computations, until a final value of Δt equal to .1 is reached. This value of Δt is about four times as large as the value of maximum Δt that the explicit scheme (with Dufort-Frankel scheme for viscous terms) would allow.

Immediately after the impulsive start, there is a large favorable pressure gradient everywhere, both on the upper and lower surfaces as shown in Figure 16. During the time period $0^+ < t < 0.35$, the loads on the airfoil are mainly due to the high pressures and high shear stresses acting on the airfoil, and as the effect of the impulsive start decreases, all the loads-total drag, pressure drag, lift and moment-decrease, as shown in Figures 13 and 14. However, the variation of C_L and C_M during the time period $0^+ < t < 0.05$ shows a rapid drop in magnitude of these quantities at first ($0^+ < t < 0.02$) and a recovery of these quantities before the variation finally stabilizes at t=0.05. Kinney [8] has also observed similar variation of the lift coefficient at early time levels in his numerical calculations for viscous flow over an impulsively started Joukowski 9°/. airfoil. The experimental results obtained by Taneda [22] for elliptic cylinders immediately after impulsive start also

indicate that the lift coefficient decreases rapidly after impulsive start, and even becomes negative before it begins to increase rapidly.

The numerical results of Mehta and Lavan [4] and the results obtained by Wu and Sampath [6] for the viscous flow over an impulsively started airfoil (Joukowski 9%. airfoil at 15^{o} angle of attack), however, show that the C_L and C_M values monotonically decrease following the impulsive start. Thus it is not very clear whether such a kink in the variation of C_L and C_M is a physical phenomenon, or if it is due to numerical inaccuracies in calculating the very large pressure values all around the airfoil following the impulsive start.

The variation of C_L and C_M, however, follows the expected behavior after t=0.05. The lift and moment coefficients decrease steadily until t=0.35. The moment coefficient about quarter chord becomes very close to zero after t=0.35. This is expected because linearized potential flow theory predicts, for symmetric airfoils, that the moment coefficient is zero at steady state.

For later time levels ($t > 0.35$) the pressure drag contributes very little towards the total drag, and viscous drag dominates. The total drag coefficient continues to fall as shown in Figure 15. Figure 15 also shows that the lift coefficient, after decreasing in magnitude until t=0.35 begins to increase again until it levels off at $t \simeq 2.0$. This increase in C_L due to thickening of the boundary layer on the upper surface, as seen in the streamline plots (Figures 24, 25 and 26). This thickness of the airfoil, leading to higher velocities and lower pressures especially near the leading edge.

The behavior of the C_L variation during this time period is qualitatively very similar to the variation obtained by Mehta and Lavan [4] as well as Wu and Sampath [6] for the 15^o angle of attack case. Before the separation bubble bursts and other stall effects occur, according to their calculations, the lift coefficient increases in a manner very similar to the present case. The increase in strength of the separation bubble in their calculations causes the effective thickness to increase, and leads to higher velocities and lower pressures at the outer edge of the bubble. Kinney [8] also reports a similar variation in C_L for the three cases (α = 5^o, 10^o and 15^o) that he considered, though no separation bubble is present in the 5^o angle of attack case.

Figures 16 through 19 show the surface pressure distribution at selected time levels. At t = 2.07, as seen in Figure 19, the surface pressure gradient over most of the upper surface is adverse, though not strong enough to cause separation. In addition, from the figures it is clear that the pressure variation at these late time levels is very little, and the pressure distribution on both the surfaces appears to be asymptotically converging towards a steady state solution.

Figures 20, 21 and 22 show the surface vorticity distribution at selected time levels. It is seen that the surface vorticity decreases everywhere with time at first rapidly and then much more slowly. The surface vorticity ahead of the 10%. chord location reaches steady state much more rapidly than the rest of the surface. A comparison of the surface vorticity variation between time levels t=1.47 and t=2.07 (Figure 22) shows that the vorticity distribution is varying very slowly

towards the asymptotic steady state solution at these time levels.

Figures 24, 25 and 26 illustrate the development of flow at selected time levels with the aid of constant vorticity lines and streamlines. The streamline plots show a rapid growth of the viscous region around the airfoil, especially on the upper surface. The vorticity contours show constant vorticity lines moving outwards from the surface of the airfoil, and extending in the downstream direction with time.

Figures 23 and 27 show the variation of the velocity profiles at selected points on the airfoil for several time levels. The gradual growth of the viscous region on the upper surface is even more apparent in these plots. At time t = 1.47, the velocity profiles in the aft portion of the airfoil show a very thick boundary layer though no separation has occurred yet. Also, in the region close to the leading edge, the boundary layer shows very little variation in size with time, indicating that, at least on regions close to the leading edge on the upper and lower surface these flow properties are close to the steady state values.

The streamline-vorticity contours, and the boundary layer profiles show a very smooth transition from the inner (finite element) region to the outer region, indicating that the use of the hybrid scheme does not produce any unacceptable behavior. As in the circular cylinder case, spurious vorticity of very small magnitude is present at large distances away from the body. But a comparison of the magnitude of the spurious vorticity values to the magnitude of the vorticity values near the surface, together with the fact that the spurious vorticity is far

away from the body indicates that the spurious vorticity can affect the final results only to a negligible extent.

The surface pressure distribution, as shown in Figures 16 through 19 does not close for many of the time levels considered. Experience with flat plate, circular cylinder and airfoil solutions indicates that the present grid is adequate to describe the viscous region for the present Reynolds number. Still, near the leading edge, the number of nodes is not sufficient to represent the rapid variation of pressure. This is the main reason why the pressure curve does not close exactly. However the integrated loads are accurate enough, because the pressure distribution everywhere else except 3 or 4 nodes near the leading edge is varying gradually and is well represented by the present grid.

Observations and Conclusions

Figure 19 indicates that the surface pressure gradient is favorable over most of the lower surface, for the 3^{o} angle of attack case. Numerical results also indicate that the viscous layer is quite thin over most of the lower surface, especially in the region ahead of the quarterchord.

It is therefore desirable to see whether some of the assumptions made in the classical boundary layer theory are valid in the accelerating flow region on the lower surface, at this moderate Reynolds number of 1000. As mentioned earlier, the viscous layer is appreciably thick on the upper surface and there is, as a result, strong interaction between the viscous flow in the boundary layer and the outer invisid flow. Thus it is less meaningful to test whether boundary layer type

of approximations are valid on the upper surface.

In particular, it is desirable to test whether (1) $\frac{\partial p}{\partial n}$ (or the pressure variation across the boundary layer) is indeed small, or negligible. (2) variations in the streamwise direction are small compared to the variations in the direction normal to the flow.

In order to test the first hypothesis, the following calculations were performed. The velocity profiles at selected locations on the lower surface were evaluated from the known velocity field solution at $t = 2.07$ by numerical interpolation. The outer edge of the viscous layer was arbitrarily defined as the point where $|\omega'| < 1$ for this purpose. Knowing the velocity, it is possible to estimate the pressure approximately using Bernoulli's equation. Bernoulli's equation, which is the integrated form of Euler's equations for an inviscid fluid contains an arbitrary constant. This arbitrary constant was determined by matching the calculated pressure, at midchord, with the surface pressure at midchord obtained from the viscous flow results.

The midchord was chosen as the matching point because of the following reasons. Near the leading edge, the surface pressure increases rapidly, and matching the pressures at the leading edge may produce large numerical errors. In addition, because of numerical inaccuracies, the numerical solution indicates a small jump in the pressure distribution at the leading edge. Thus, it is difficult to match the pressure at the outer edge with the surface pressure at the leading edge. Near the trailing edge the surface curvature is large, and it is difficult to define a local normal at the trailing edge. Besides since the boundary layer near the trailing edge is thicker than elsewhere on the

lower surface, matching the pressures near the trailing edge may cause inaccuracies.

In Figure 19, the pressure distribution at the outer edge of the boundary layer is compared with the pressure distribution obtained from the viscous flow calculations. It is seen that the agreement is quite good over most of the lower surface. Thus it appears reasonable to expect that the pressure varies very little across the boundary layer, in accordance with the classical boundary layer theory. It is also interesting to note that the slope of the pressure curve ($\frac{dp}{dx}$, which is approximately equal to $\frac{dp}{ds}$, the surface pressure gradient) also agrees reasonably well over most of the surface.

In order to test the second hypothesis, the following calculations were performed. The vorticity ω' may be defined in a set of boundary fitted coordinates as follows.

$$\omega' = -\frac{\partial v}{\partial s} + \frac{\partial u}{\partial n}$$

Here s and n represent coordinates along and normal to the surface respectively; u and v are the corresponding velocity components. According to boundary layer assumptions $\frac{\partial v}{\partial s}$ is of order $\frac{v_\infty}{L}(1/\sqrt{Re})$ while $\frac{\partial u}{\partial n}$ is of order $(\sqrt{Re})\frac{v_\infty}{L}$. Thus, it is reasonable to drop the streamwise derivative, and write

$$u_e = \int_o^\delta \omega' dn$$

where u_e is the velocity at the boundary layer edge, along the s coordinate direction.

The magnitude of u_e was estimated at selected locations on the lower surface, using the above relationship. These values are compared with the velocity at the edge of the boundary layer calculated from the known velocity field, in Table 3.

Table 3. Determination of Viscous Layer Velocity Profile Using Approximate Methods

Node	4	8	12	16	20	24
Integral Relationship	.950	1.077	1.090	1.080	1.058	.74
Approximate Method	1.05	1.1418	1.124	1.101	1.078	1.346

In Table 3, 6 nodes are arbitrarily chosen from leading edge to trailing edge. It is found that everywhere, except at the 24th node, the error involved in calculating the velocity using approximate relationships is less than 10%. At the 24th node, since it is very close to the trailing edge, the agreement is not very good. Surprisingly the agreement improves as we move from leading edge to trailing edge; this is due to the fact that the numerical quadrature used to evaluate the velocity gives inaccurate results whenever the value of Δn used is not small enough to represent the thin viscous layer adequately. In the above calculations a value of $\Delta n = .01$ was used, which is very large compared to viscous layer thickness in the leading edge region.

Thus the above approximate analysis shows that streamwise derivatives are small even at moderate Reynolds numbers, at least in accele-

rating flows. In addition, this assumption gives a very valuable relationship between u and ω' involving integration only in one direction. Once u is known v may be determined from the local application of continuity equation. Thus, whenever rapid, but approximate determination of the velocity profile is sought, the above relationship may be used in place of the integral relationship for velocity.

In the present chapter three different body shapes have been considered. The flexibility of the present method permits the use of the same numerical procedure, and hence the same computer program to be used to treat these three problems. The test cases indicate that the method can produce accurate time dependent solutions for external flow problems. In the case of Joukowski 12%. airfoil, though no direct comparison is available, the numerical solution follows the expected behavior from physical considerations.

In the next chapter, the present method is applied to the study of viscous flow over oscillating airfoils.

CHAPTER V

VISCOUS FLOW OVER OSCILLATING AIRFOILS

The study of viscous flow past airfoils is a somewhat different problem from the cases considered previously for two reasons. First of all, as discussed in the mathematical formulation, the rotation of the solid introduces additional terms in the kinetic and kinematic relationships, and a proper numerical treatment of these additional terms is essential for an accurate simulation of the physical processes. Secondly, unlike the previous cases, in the present study the exact time history is of interest, and not just the peak or limit values. Thus far, for the cases studied in the previous chapter, the steady state properties, rather than the actual time histories, were of interest, and it was permissible to make approximations during the time development of the flow. But in the present case, it is necessary to reexamine all the numerical approximations involved to ensure accurate prediction of the loads. The time history of the pitching moment variation, for example, determines the conditions that may lead to flutter, and it is necessary to get an accurate representation of the pitching moment variation for this purpose. Therefore, before discussing the results, we discuss the numerical approximations that may significantly affect the prediction of the time history of the loads.

It has been observed that the numerical solution of viscous flows depends on a large number of factors: grid size, the surface vorticity scheme, the truncation errors assosicated with the discretization etc. The loads on the impulsively started airfoil, as evaluated from the numerical solution at earlier time levels, are critically dependent on the grid size for their accuracy, because the viscous layer is very thin at early time levels. Thus at later time levels, a coarser grid may be sufficient. The surface vorticity scheme , in many cases , determines the accuracy and reliability of a given scheme, because it is not uncommon to encounter wiggles and unexpected behavior in the vorticity field that can be directly traced back to an improper treatment of the surface vorticity scheme, especially at high Reynolds numbers.

Roache [14] discusses in great detail how the errors associated with the discretization of the governing equations play a significant role in the accuracy of the numerical solution. While treating the vorticity transport equation, many investigators use schemes such as Arakawa scheme for the convection terms, at the expense of a large number of arithmetic operations for the purpose of conserving vorticity and avoiding errors such as phase errors, aliasing errors, etc.

The time differencing, in addition, can introduce errors. For example, the leap frog method has been known to produce time splitting errors in some cases.

Since, in the present study, the main objective is to simulate the time history of the flow as accurately as possible, special care has been taken to achieve this purpose. In the evaluation of surface vorticity, for example, analytical integration methods have been used where-

ever possible. While iterating for the vorticity field in the outer region using successive overrelaxation techniques, high tolerance limits have been used to ensure proper convergence. In the inner field the velocity is evaluated using accurate analytical techniques whereever possible.

In addition, in the course of computations, a number of tests have been performed using different time steps to study the effect of time step on the accuracy of the solution. For the time steps considered, the time step is found to play a minor role in the accuracy of the solution.

In order to demonstrate this point, the surface vorticity distribution obtained at a time level of t=.32 is shown for selected nodes on the surface of the airfoil for two test runs, in Table 4. The numerical solution at t=.28 was chosen as the reference solution (initial solution). The time steps used were .04 and .02 respectively in the two cases. In Table 4, node 1 corresponds to the leading edge, node 7 corresponds to the trailing edge, and the other nodes are located at arbitrary stations on the upper surface. During the time period, the airfoil undergoes the following pitching motion:

$$\alpha = 9^{\circ} - 6^{\circ} \cos 6t$$

Table 4. Effect of Time Step on the Numerical Results

Point	1	2	3	4	5	6	7
Run 1 $\Delta t=.04$	-117.44	-47.56	-25.71	-5.999	2.536	-1.897	38.37
Run 2 $\Delta t=.02$	-117.47	-48.33	-25.95	-6.20	2.538	-2.40	40.68

It is seen from the above table, that the solution at t=.32, obtained from two different runs differs very little. The trailing edge (node 7), being the most sensitive point in the entire flow field, shows the maximum deviation. Since the surface vorticity distribution is the most sensitive quantity among all the flow properties, its insensitiveness to Δt indicates that the time step plays a minor role in the accuracy of the solution.

In addition, various possibilities such as the Crank-Nicholson scheme, fully implicit scheme, time element scheme have been explored for the integration of the ordinary differential equations obtained by the application of Galerkin's process. All the above methods produce virtually the same solution for the time levels considered.
Though no detailed analysis of the effect of grid size on the numerical solution has been performed, the final results indicate that there are sufficient number of nodes in the neighborhood of the airfoil to describe the viscous region adequately.

It was recognized during the course of computations, that the

downstream boundary condition should be modified, since the wake might extend beyond the downstream boundary at later time levels. It may be noted that, for the four cases considered in the previous chapter, the assumption that ω' was equal to zero, was accurate enough, because of the low time levels considered. In the present calculations the following boundary condition is used.

$$\frac{\partial \omega}{\partial x} = 0 \quad \text{at downstream boundary.}$$

While calculating the velocity boundary conditions, the velocity values at the nodal points on the downstream boundary were evaluated using the integral relationship for velocity. The effect of the vorticity downstream of the downstream boundary (i.e. the vorticity leaving computational domain) was ignored. It is clear that such an assumption would introduce additional approximations in the calculation of the velocity boundary conditions. However, since the influence of velocity boundary conditions at any point in the field decreases inversely with the distance between the point and the boundary, it is expected that the above approximation would not affect the velocity field in the neighborhood of the airfoil.

In order to ensure proper conservation of vorticity, the net amount of total vorticity Q_1 leaving the downstream boundary was calculated at each time level.

$$Q_1 = \int_0^t dt \int_{S_1} (\bar{v} \cdot \bar{n})\, \omega'\, dS$$

Here S_1 denotes the downstream boundary, $\bar{n}$ is the unit normal vector, positive when directed away from the outer field. Then, while

calculating the total vorticity in the flow field, Q_1 gives the magnitude of total vorticity outside the computational domain.

There are no experimental results available for comparision for the cases considered here. However, it is felt that the numerical results must be in qualitative agreement with linearized potential flow theory, at least for low angles of attack, when there is no trailing edge separation.

Therefore, the first two cases considered involve very low mean angle of attack and amplitude. As expected good qualitative agreement is found in these two cases. The third case studied involves the study of large amplitude-high frequency motion.

Linearized Potential Flow Results

We first present some linearized potential flow results, and show the phase relationship between the integrated loads and the angle of attack. These results are available in open literature [23].

We consider a thin symmetric airfoil, placed in a uniform stream of velocity $\bar{v}_\infty$, at a mean angle of attack α_o. Because superposition is valid within the framework of the linearized potential flow theory, the mean value of the lift coefficient is given by $2\pi\alpha_o$ and the mean value of the moment coefficient about quarter chord is zero. These mean quantities are unaffected by the perturbations induced by the oscillations in pitch.

We further assume that the pitching motion of the airfoil is given by

$$\alpha = \bar{\alpha} e^{i\omega_1 t}$$

Where $\bar{\alpha}$ is the amplitude of motion (a complex number with magnitude and phase angle) and ω_1 is the frequency of oscillations. The complex representation is used here because of its generality. Then, the following expressions are true within the framework of linearized potential flow theory:

$$\text{Lift} = \pi\rho \frac{L^2}{4} \left[v_\infty \dot{\alpha} + \frac{L}{4} \ddot{\alpha}\right]$$

$$+ 2\pi\rho v_\infty \frac{L}{2} C(k) \left[v_\infty \alpha + \frac{L}{2} \dot{\alpha}\right]$$

Moment about quarter chord point

$$= - \pi\rho \frac{L^2}{4}\left[v_\infty \frac{L}{2} \dot{\alpha} - \frac{3}{32} L^2 \ddot{\alpha}\right]$$

In the above expressions, C(k) is the Theoderson function defined in terms of Bessel's functions. L is the chord of the airfoil, and the dot on top of 'α' denotes differentiation with respect to time. 'k' is the reduced frequency, given by $\omega_1 L/2\ v_\infty$.

After non-dimensionalizing time with respect to $\frac{L}{v_\infty}$, expressions for the lift and moment coefficients are obtained as follows:

$$C_L = \frac{\text{Lift}}{\frac{1}{2}\rho v_\infty^2 L} = \frac{\pi}{2}\left[\dot{\alpha} + \frac{\ddot{\alpha}}{4}\right] + C(k)\ [2\pi\alpha + \pi\dot{\alpha}]$$

$$C_M = \frac{\pi}{2}\alpha\left[- \frac{\dot{\alpha}}{2} - \frac{3}{32}\ddot{\alpha}\right]$$

In the above expressions the time derivatives are evaluated with the non-dimensional time.

We define

$$C(k) = A + iB$$

From tables, $C(.3) = .66496 - .17933i$

$C(3) = .50635 - .0399i$

If we are interested in pure sinusoidal oscillations, we only need to consider the imaginary parts of the above expressions for loads. Thus, after simplifications,

$$\alpha = \bar{\alpha} \sin \omega_1 t$$

$$\frac{C_L}{\bar{\alpha}} = \left(\frac{\pi}{2}\omega_1 + 2\pi B + \pi\omega_1 A\right) \cos \omega_1 t + \left(2\pi A - B\omega_1\pi - \frac{\pi}{8}\omega_1^2\right) \sin \omega_1 t$$

$$\frac{C_M}{\bar{\alpha}} = \frac{\pi}{2}\left(-\frac{\omega_1}{2} \cos \omega_1 t + \frac{3}{32}\omega_1^2 \sin \omega_1 t\right)$$

From the expression for C_M, it is clear that the moment coefficient will always lag behind the angle of attack. If C_M is plotted as a function of α, the plot will describe a counter clockwise loop for the present definition of C_M (nose-up moment positive) indicating positive aerodynamic damping. Linearized potential flow theory, thus predicts positive aerodynamic damping always.

Considering the expression for C_L, it is clear that for small reduced frequencies ($\omega_1 \ll 1$) C_L will lag behind α. This is because the coefficient of the term containing $\cos \omega_1 t$ becomes negative for low

values of ω_1, B being always negative. The circulatory component of lift always lags behind the angle of attack. However, for larger values of ω_1, the inertial terms in the expression for C_L may dominate, causing C_L to lead α. For the cases considered here ($.6 \leq \omega_1 \leq 6$) this is found to be the case.

Similar conclusions may be drawn for the case where the pitching motion is defined by a cosine wave.

For very low reduced frequencies, the inertial terms in the expressions for C_L and C_M may be dropped, and additional approximations may be made leading to simpler expressions for the lift and moment coefficients. Such approximations, commonly called "Quasi-unsteady" and "Quasi-steady" approximations are not applicable for the present calculations. The full unsteady expressions are more appropriate.

Viscous Flow Results

In the following sections, we present the numerical results for the viscous flow over oscillating airfoils for three different combinations of mean angle of attack, amplitude and reduced frequency. These calculations were performed for a Reynolds number of 1000. A detailed time history of the integrated loads is presented for each of the three cases and compared with the potential flow theory whenever appropriate. The properties of the viscous flow, such as surface pressure and vorticity distribution, velocity profiles in the boundary layer, streamlines and vorticity contours are also presented at several selected time levels for these cases.

Case 1. Viscous Flow Over a Joukowski 12%. Airfoil Undergoing Low Amplitude Oscillations at Moderate Reduced Frequencies. For this study, the finite element network shown in Figure 2 is used. In addition a coarse grid ($\Delta x = .1$, $\Delta y = .05$) is added to the outer field. This coarse grid contains 1000 nodes, and addition of this coarse grid ensures that the downstream boundary is located sufficiently far away from the airfoil. For the present case, the downstream boundary is located 5.7 chords away from the trailing edge. The upstream boundary is located in this case .9 chord units away from the leading edge.

The airfoil is impulsively started from rest at a mean angle of attack equal to 3^{o}, and set into pitching motion according to the following equation.

$$\alpha = 3^{o} + 1^{o} \sin (.6t)$$

where time level t is non-dimensionalized with respect to the ratio between chord length and free stream velocity. The reduced frequency based on semichord, for this motion is .3. The calculations have been performed up to a time level of 10.4, which corresponds approximately to one complete cycle of pitching motion. The time step for these calculations is varied gradually from .0075 to .1, in order to ensure good resolution of results during the early time levels.

Because of the impulsive start, very large loads, pressure coefficients and vorticity values are obtained during the early part of the cycle, and these effects become negligible after $t > 1.3$. Because the primary objective of the present method is to study the loads associated with the pitching motion, these impulsive loads are of minor significance,

and will not be discussed here.

The upstroke of the airfoil takes place during the time period: $0 < t < 2.618$. At t=2.618, the airfoil is at its maximum angle of attack (4^{o}). Between t=2.618 and t=7.854, the airfoil undergoes downstroke motion and the angle of attack decreases from 4^{o} to 2^{o}. Between the time levels t=7.854 and 10.472, the airfoil is on the upstroke again, and reaches the mean angle of attack at the end of this time period.

The angular velocity of the pitching motion is maximum at the time levels t=o, t=5.236 and t=10.472. The inertial term corresponding to the centrifugal acceleration ($\Omega^2 r \frac{dr}{ds}$ effect) is at its largest magnitude at these time levels. Since Ω varies at the frequency ω_1, this term will vary at the frequency $2\omega_1$. However, the centrifugal acceleration effect produces identical changes in the pressure distribution on the upper and lower surface. Thus its effect on C_L and C_M is zero. Since the effect on the pressure drag, however, is cumulative, the contribution of this term to pressure drag will lead to a component of the pressure drag varying in time at a frequency of $2\omega_1$.

The angular acceleration $\dot{\Omega}$(equal to $-\ddot{\alpha}$) is maximum in magnitude at time levels 2.618 and 7.854, and the inertial term corresponding to the angular acceleration effects ($\dot{\Omega} r^2 \frac{d\theta}{ds}$ effect) assumes its largest magnitude at these time levels.

These inertial terms affect the surface pressure distribution and load history to a noticable extent even at this moderate reduced frequency, and are responsible for many of the flow phenomena observed in the present case.

The time histories of the various integrated loads are presented in Figures 28, 29, 30, 31 and 32 for the time period $1.3 \leq t \leq 10.4$. The following observations may be made regarding the load histories.

(1) Viscous Drag: The viscous drag values are somewhat high during the early time levels. ($t < 2$). This is because these values are still influenced by the impulsive start effect. During the rest of the time period, the viscous drag values are found to be relatively insensitive to the pitching motion. This is due to the following reason. Even though the pitching motion leads to build up and depletion of circulation around airfoil, the net effect on the surface shear stress is actually small, since any increase in shear stress on the upper surface is partly compensated by a decrease in shear stress (as observed by surface vorticity magnitude) on the lower surface, and vice versa.

This observation has been found to be true even in high Reynolds number cases [24]. Numerical results, based on boundary layer theory, for viscous flow on an oscillating airfoil in a fluctuating air stream are presented in Reference 24. These results indicate that the drag variation due to the pitching motion alone is very small compared to drag variation due to free stream speed fluctuations.

(2) Pressure Drag: The pressure drag is large at earlier time levels, because of the impulsive start effects, and decreases rapidly as shown in Figure 29. Near t=2.1, the pressure drag shows a pronounced dip. This is due to the leading edge suction effect--a large drop in pressure in the leading edge region due to the higher velocities as the angle of attack increases. The drag recovers to somewhat higher values during the downstroke. The pressure drag, in general, is found to be

very much smaller in magnitude than the viscous drag for the present case.

(3) Lift: The Lift history based on the present numerical results are shown in Figure 31, and compared with the results based on linearized unsteady potential flow theory. It is observed that there is good agreement between the two sets of results in phase. It is also noted that the lift coefficient leads the angle of attack in phase. The two sets of results do not agree in magnitude, however. This is expected because of the strong viscous effects on the flow properties near the surface at this moderate Reynolds number.

(4) Moment: The variation of the moment coefficient about quarter chord is presented as a function of time in Figure 32, and compared with the potential flow theory. The present results show a pronounced dip in C_M at t=2.1, while the potential flow theory does not predict any such dip. At other time levels, it is observed that the numerical results and the potential flow results agree reasonably well both qualitatively and quantitatively.

If the moment coefficient is plotted as a function of α, the potential flow theory as well as the viscous flow results produce counter clockwise hysteresis loops. In view of the present sign convection for moment coefficient (nose-up moment positive) this means positive aerodynamic damping--a property important from the aerodynamic flutter point of view.

The pressure distribution on the surface of the airfoil is shown in Figures 34, 35, 36 and 37 at selected time levels. It is possible to explain the surface pressure variation and the load histories (parti-

cularly C_L and C_M) based on familiar concepts of circulation, induced camber and angular acceleration effects.

As the angle of attack increases, the front stagnation point moves rearward, indicating the build up of circulation around the airfoil. The build up of circulation is casued by the increase in the angle of attack, as well as rotation of the airfoil. This rotation of the airfoil induces on the surface a distribution of vorticity, and hence a circulation around the airfoil. In the case of thin airfoil, this additional circulation is equivalent in form to the circulation produced by a stationary cambered airfoil, and is known as the induced camber effect. However, as the circulation builds up on the airfoil, vorticity is being continuously shed into the wake; this vorticity moves at a speed much less than the free stream velocity, and also diffuses as it moves down stream. The effect of this shed vorticity is to cause the circulatory lift to lag behind the angle of attack.

The effect of this build up of circulation leads to lower pressures on the upper surface of the airfoil and higher pressures on the lower surface of the airfoil as shown in Figure 34.

As the angle of attack decreases, an exactly opposite process takes place. The circulation around the airfoil decreases, and the circulatory lift also decreases.

Even though the terms "circulatory lift", "induced camber effect" etc. are used only in the context of potential flow theory in literature, in the case of viscous flows these terms are equally valid provided proper care is taken to recognize the effect of the viscous region on the quantities described here. For example, while calculating the cir-

culation around the airfoil, it is now necessary to consider both the surface vorticity, and the vorticity in the viscous region around the airfoil.

The inertial acceleration effects, however, modify the surface pressure distribution and the integrated loads. Among the inertial terms, the term corresponding to the angular acceleration ($\dot{\Omega}r^2 \frac{d\theta}{ds}$ effect) is of significance.

During the upstroke, and part of the downstroke, ($0 < t < 5.236$) it may be shown that the angular acceleration effect tends to produce adverse pressure gradient on the upper surface, and favorable pressure gradient on the lower surface. As a result, during the upstroke, the cumulative effects of the shear stress gradient effect ($\frac{\partial \omega}{\partial n}$ effect) and the angular acceleration effect tends to produce large adverse pressure gradients aft of midchord. It is seen in Figure 32, for example, that the pressure gradient t=2.64 ($\alpha = 4^{\circ}$) is much larger that the pressure gradient at t=5.235($\alpha \approx 3^{\circ}$, Figure 35). This large adverse pressure gradient leads to higher values of pressure on the upper surface of the airfoil, and causes a drop in lift even before the maximum angle of attack is reached. It is for this reason that the lift leads the angle of attack in phase, even though the circulatory component of lift tends to lag the angle of attack in phase.

During the time period $5.236 < t < 10.472$, the angular acceleration produces favorable pressure gradient on the upper surface, and leads to a recovery of lift even before the angle of attack reaches its minimum value. Thus throughout the cycle the total lift leads the angle of attack in phase.

The numerical results show that there is trailing edge separation on the upper surface near $\alpha = 4^{\circ}$, as the angle of attack increases. The flow reattaches itself during the downstroke. The separated region is very small and does not affect the integrated loads significantly. The velocity profiles on the upper surface are plotted at selected time levels in Figure 33. It is clearly seen that the flow near the trailing edge has a tendency to separate as the angle of attack increases.

Case 2. Viscous Flow Past a Joukowski 12%. Airfoil Undergoing Low-Amplitude Oscillations at High Frequencies. For this case, the finite element network used in Case 1 is again used, and the configuration of the outer field is also kept the same as for Case 1. The numerical solution obtained for Case 1 is used as the starting solution. As before, the Reynolds number of the flow is assumed to be 1000. The airfoil is assumed to undergo the following pitching motion.

$$\alpha = 3^{\circ} + 1^{\circ} \sin 6t$$

The reduced frequency for this specified motion is 3.0 based on semichord and free stream velocity.

The numerical calculations were performed up to a non-dimensional time level of 2.4, using a constant value of time step equal to .04. During this time period the airfoil undergoes a little more than two complete cycles of oscillation. Most of the calculated flow properties were observed to vary periodically after the first cycle. The impulsive start produced significant transient loads during most of the first

cycle; the transient effects were found to be negligible during the second and third cycles.

The time history of the loads--C_{D_p}, C_{D_f}, C_D, C_L, and C_M are shown in Figures 38 through 42 for two cycles. The hysteresis loops for the lift and moment coefficients are shown in Figures 43 and 44. In addition, the results from the potential flow for C_L and C_M are also presented in Figures 41 through 44. Figures 45 through 50 show the surface pressure distribution at selected time levels. The streamline contours as observed in a rotating frame of reference, as well as the constant vorticity contours as observed in an inertial coordinate system are shown in Figures 51, 52 and 53 at selected time levels.

The following observations may be made regarding the load histories from the numerical solution presented in Figures 38 through 44.

(1) Pressure Drag: It is observed from Figure 38 that the pressure drag reaches a minimum at $t \simeq .35$ and $t \simeq 1.39$. The variation of pressure drag is found to be nearly periodic with a time period equal to 1.04, which corresponds to the time period of the pitching motion. The pressure distribution at time level $t \simeq 1.44$ (Figure 46) shows lower pressures near the leading edge compared to the pressure distribution at time level $t = 1.28$ (Figure 46). Thus the minimum pressure drag observed at time level $t \simeq .35$ and $t \simeq 1.39$ is entirely due to the low pressures near the leading edge--the leading edge suction effect.

The amplitude of the pressure drag variation is about .002, as seen from Figure 38, and the pressure drag oscillates about a mean value of .019. A comparison of typical magnitudes of pressure drag and viscous drag values as shown in Figures 39 and 39, clearly indicates that

the viscous drag is the dominant contributor to the total drag.

(2) Viscous Drag: From Figure 40, it is observed that the variation of viscous drag with time is very small, ($\Delta C_{D_f} < .004$) indicates that the viscous drag is relatively insensitive to the pitching motion. This was found to be true even in Case 1, as mentioned earlier. The variation of the skin friction coefficient is found to be nearly periodic, but not harmonic. During the second cycle, the skin friction drag values are somewhat higher than for the first cycle. Thus, it may be necessary to perform the calculations for more than 2 cycles to reach periodic behavior. This is expected of course, because the skin friction drag is directly dependent on the surface vorticity distribution. While all the other quantities like stream function, velocity, vorticity, etc. have reached limit cycle or periodic variation, the surface vorticity variation is still not periodic, even after two cycles.

(3) Lift and Moment Variation: It is possible to explain the variation of lift and moment coefficients, and the variation of surface pressure distribution based on the concepts of circulatory lift and inertial forces. The effect of viscosity is to modify the loads predicted by the potential flow theory somewhat by the presence of a thick boundary layer around the airfoil at this moderate Reynolds number. A brief qualitative explanation of the lift and moment history is given here.

During the upstroke, the numerical results indicate that the surface vorticity at the leading edge increases, and that the forward stagnation point moves backwards. This indicates the build up of circulation around the airfoil. At the same time, vorticity is continuous-

ly being shed into the wake from the trailing edge region, to satisfy conservation of vorticity. This shed vorticity in the wake moves at a velocity less than free stream velocity (owing to the velocity defect) in the wake and also diffuses rapidly. In classical thin airfoil theory, this shed vorticity is assumed to move at free stream velocity. Since in the viscous flow case the shed vorticity moves at a much lower speed the increase in circulatory lift takes place at a much slower rate than in the potential flow case. Thus the circulatory lift lags behind the angle of attack much more in the case of viscous flow than in the case of potential flow.

The effect of inertial forces, especially the angular acceleration, is to produce adverse pressure gradient on the upper surface during the upstroke. The cumulative effects of surface shear stress gradient and the angular acceleration effect produces very large pressure gradients on the upper surface as shown in Figure 45 at time level $t = 1.28$. There is actually a cross over of the upper and lower surface distributions as shown in Figure 45.

As a result of the larger pressures on the upper surface, the total lift begins to fall even before the maximum angle of attack is reached, and the maximum lift occurs at $t = 1.08$ (Figure 41). Thus the numerical results correctly predict that the total lift leads the angle of attack in phase. The predicted lift, however, lags behind the lift predicted by potential flow theory, presumably because the circulatory lift in the viscous flow case lags behind the circulatory lift for the potential flow case as explained earlier.

The thick boundary layer around the airfoil also leads to lower

magnitudes of C_L compared to the potential flow results, as shown in Figure 41.

During part of the downstroke, as the airfoil angle of attack decreases from 4^o to 3^o, the adverse pressure gradient produced by the angular acceleration effect continues to exist. In addition, the circulatory lift drops in magnitude as the angle of attack decreases. As a result, the total lift continues to decrease during this period ($1.3 < t < 1.56$). Figure 46 shows a large adverse pressure gradient on the upper surface, and it is seen that the enclosed area in the cross over region has also increased, showing that the lift is decreasing. During part of this cycle, the C_L values become negative as shown in Figure 41.

The effect of higher pressures on the upper surface is to produce a nose up moment, and from Figure 42, it is seen that C_M steadily increases during the upstroke and during part of the downstroke ($1.3 < t < 1.56$, $3^o < \alpha < 4^o$).

During the rest of the downstroke the angle of attack decreases from 3^o to 2^o ($1.56 < 1.82$). The surface vorticity at the leading edge further decreases in magnitude, indicating further decrease in circulatory lift magnitude. However, during this period the angular acceleration changes sign, and produces a change in the surface pressure gradient all over the surface. The effect of the angular acceleration is, for this period, to produce favorable pressure gradient on the upper surface, and adverse pressure gradient on the lower surface. As a result, a second crossover in surface pressure distribution as shown in Figure 47 appears. The lift coefficient begins to increase after $t = 1.6$. It

is seen in Figure 48 that the second loop has increased in size at $t = 1.76$ indicating the increase in lift.

The effect of lower pressures on the upper surface, and higher pressures on the lower surface, in the region defined by the second cross-over, tends to produce a nose-down pitching moment effect, and the moment coefficient begins to decrease after $t = 1.6$.

During the period $1.82 < t < 2.08$, the angle of attack increase is from 2° to 3°. The lift coefficient continues to increase while the moment coefficient continues to decrease.

The numerical results indicate trailing edge separation during the periods $1.04 < t < 1.24$ and $1.86 < t < 2.08$. This separation is primarily due to the adverse pressure gradient on the upper surface. This separated flow region is very small and does not affect the integrated loads, or the surface pressure gradient very much.

In order to enhance the understanding of the flow field, and to ensure that the numerical solution produces physically realistic velocity and stream function fields, the vorticity and stream function contours are shown in Figures 51, 52 and 53 at selected time levels. The streamlines are plotted as observed by an observer stationed on the rotating airfoil. As a result, during the upstroke (Figure 52) the observer will see the free stream approaching the airfoil at an angle of attack less than α, and observe the streamlines far downstream at an angle of attack greater than α. The exactly opposite effect occurs during the downstroke.

The streamline plots show many of the qualitative features expected: (1) the high velocity near the leading edge on the upper

surface as seen by the crowding of the streamlines in that region. (2) the thick boundary layer on the upper surface aft of mid chord. In addition, the smoothness of the streamlines as they enter and leave the finite element region shows that the hybrid scheme permits a smooth transition from one scheme to another.

The lift and moment hysteresis loops are plotted for the two cycles of motion in Figures 43 and 44. The moment hysteresis loop is found to be in the counterclockwise sense, both for the potential flow and the present case. Thus both these solutions predict positive aerodynamic damping.

Comparison of the Results for Cases 1 and 2

Valuable conclusions regarding the effect of reduced frequency on the flow properties may be drawn from Cases 1 and 2, because these two cases involve the same mean angle of attack and amplitude of motion, but different reduced frequencies.

Considering the moderate reduced frequency case (k = 0.3 based on semi-chord) the inertial effects are significant even at this reduced frequency. The quasi-unsteady theory, for example, predicts a C_L variation that is quite different from the unsteady flow theory which is more appropriate for the present reduced frequency. The predicted viscous flow results agree in phase with the potential flow theory.

Comparing $C_{L_{max}}$ for both the cases, it is found that there is considerable increase in $C_{L_{max}}$ at the higher reduced frequency according to the potential flow theory. The viscous flow results do not show such an increase. The $C_{L_{max}}$ is however different for both the cases. The

$C_{L_{min}}$ for the high reduced frequency case becomes negative, which is not surprising, because of the pronounced inertial effects at this frequency. The C_M variation is very pronounced for the higher reduced frequency case, again because of the increase in the magnitude of the inertial forces. The C_M variations in both the cases predict positive aerodynamic damping, in accordance with the unsteady potential flow theory.

The viscous drag variation was found to be relatively insensitive to the pitching motion in both the cases. The pressure drag variation, though small, could be traced back to the leading edge suction effect for both the cases. The total drag as well as its components are of comparable magnitudes in both these cases.

Both the cases predict trailing edge separation during parts of the cycle. The separation is caused by a combination of adverse shear stress gradient and inertial force effects leading to adverse pressure gradients on the upper surface.

Case 3. Viscous Flow Over a Joukowski 12%. Airfoil Undergoing Large Amplitude Oscillations at High Reduced Frequencies. For this case, the finite element network shown in Figure 2 is used. The number of nodes in the outer field is kept the same as in Case 1. The numerical solution discussed in the previous chapter for viscous flow over a Joukowski 12%. airfoil at 3^o angle of attack (Re = 1000, t = 2.07) is chosen as the starting solution. The airfoil is assumed to undergo the following pitching motion.

$$\alpha = 9^o - 6^o \cos(6t)$$

The above relationship gives $\alpha = 3^{o}$, and Ω=0 at t=0. Thus at t=0, the starting soltuion and the present variation match both in angular velocity and angle of attack. This is the reason the cosine variation is chosen in preference to the sine variation. The mean angle of attack, and the amplitude of motion have been so chosen that the airfoil oscillates in and out of the static stall region.

The numerical calculations have been performed for the first cycle and part of the second cycle ($0 < t < 1.68$). A constant value of time step equal to .04 has been used throughout the computations. The numerical results indicate that the integrated loads are nearly periodic, though not necessarily harmonic, after $t \sim .40$.

Even though the maximum angle of attack reached in the present case is 15^{o}, no dynamic stall effects are observed. Many investigators [25,26,27] have observed that the dynamic stall occurs at an angle of attack higher than static angle of attack, from theoretical studies based on potential flow models, and experiments conducted at higher Reynolds numbers. In addition,the dynamic stall angle is observed to increase with the reduced frequency. Many explanations have been suggested in literature regarding the stall delay, but the theory proposed by Carta [28] based on inviscid flow results is more appropriate at high reduced frequencies. Carta observed that the adverse pressure gradient on the upper surface of the oscillating airfoil as calculated from inviscid flow theory is much lower over most of the upper surface than the corresponding adverse pressure gradient on a stationary airfoil at the same instantaneous angle of attack. Thus, if separation, leading to the formulation of the bubble and stall, depends only on the pressure

gradient, an oscillating airfoil at a given angle of attack is less likely to stall than a stationary airfoil at the same value of α.

Because no dynamic stall effects are observed in the present case (despite the appearance of a separation bubble, to be discussed later), it is felt that the lift and moment variation must be in qualitative agreement with the unsteady linearized potential flow results. Therefore the potential flow results are also presented in Figures 54, 55, 56 and 57, along with the present viscous flow results for C_L and C_M. The drag variation is presented in Figures 58, 59 and 60.

The C_L variation is shown in Figure 54. It is observed that the C_L variation predicted by the viscous flow lags behind the C_L variation given by the potential flow results. This is presumably because convection of the shed vorticity in the viscous wake occurs at a much lower mean velocity than in the potential flow case, where the vorticity shed from the trailing edge is convected away at the free stream velocity. As a result, the circulatory lift builds up at a much slower rate in the viscous flow case during the upstroke. Similarly, the circulatory lift decreases at a much slower rate for the viscous flow. Thus the circulatory lift, and hence the total lift always lag behind the lift variation predicted by potential flow theory.

The $C_{L_{max}}$ occurs before α reaches α_{max}, because of reasons similar to those given for Cases 1 and 2. The large adverse pressure gradient on the upper surface, leading to higher pressures aft of mid chord, causes the lift to decrease even before α_{max} is reached. This effect is a phenomenon governed by inertial forces, which are substantial for Case 3 compared to Cases 1 and 2.

It is observed in Figure 54, that the maximum lift achieved is much higher than the static C_L value for 15° angle of attack. Similarly, $C_{L_{min}}$ reaches large negative values. This is due to the fact that the inertial effects at this high reduced frequency and large amplitude of pitching motion create substantial pressures on the surface of the airfoil.

A comparison of the C_L magnitudes between the first cycle and second cycle shows that the C_L variation is not periodic yet. Thus it may be necessary to perform the calculations for 3 or more cycles before a reasonable periodic behavior is observed. This was not attempted in the present case, because the deviation from periodic behavior is small during the two cycles, compared to the magnitudes of $C_{L_{max}}$ and $C_{L_{min}}$.

Figure 55 shows the lift hysteresis effect for both the potential flow and viscous flow cases. The orientation of the hysteresis loop for the viscous flow case is different from that for the potential flow, because of the phase lag.

The moment history is presented in Figure 56, and compared with the potential flow results. It is again observed that the C_M history, as predicted by the viscous flow theory lags behind the potential flow results. It is seen that the C_M variation is also nearly periodic, though it may require 3 or more cycles before good periodic behavior is established.

The moment hysteresis loops as predicted by the present calculations, and the potential flow theory, are shown in Figure 57. These variations describe counterclockwise loops in the present case. Thus the aerodynamic damping is positive--a very desirable property from the

flutter point of view. It is also observed that the hysteresis loop for the viscous flow case is nearly elliptic, indicating that the variation is primarily simple harmonic, with higher frequency components present in small amounts. It may be noted that the potential flow theory, which retains only first order perturbations will always predict a simple harmonic variation of C_L and C_M.

The pressure drag variation is shown in Figure 58. It is seen that the pressure drag reaches its minimum value near $\alpha = \alpha_{max}$ ($t \simeq 0.56$ and $t \simeq 1.60$). This is primarily due to the very high velocities, and the low pressures that exist in the leading edge region at α_{max}. The figure shows that the pressure drag even becomes negative at some time levels. However, if the drag components are re-expressed in a more conventional wind axis system, the pressure drag and viscous drag coefficients will always be positive.

Even though the maximum value of pressure drag is definitely higher for the first cycle than for the second cycle, the pressure drag variation shows a near periodic variation after $t \simeq .44$. The variation of C_{D_p} during the time period $.44 < t < .64$ compares reasonably well with the variation of C_{D_p} during the second cycle for the corresponding period: $1.48 < t < 1.68$.

The viscous drag variation is shown in Figure 59. Unlike Cases 1 and 2, where the skin friction coefficient variation was found relatively insensitive to the pitching motion, in the present case the viscous drag varies from a minimum value of .066 to a maximum value of .103 during the first cycle. This large variation is primarily due to the large variation in angle of attack ($3^\circ < \alpha^\circ < 15^\circ$) which leads

to the surface shear stress variations of large magnitude during the cycle.

A brief description of the factors affecting the viscous drag variation will be given here. During part of the upstroke ($0 < t < .32$) the increase in angle of attack increases the velocities over the lower surface, leading to increased shear stress magnitudes over most of the lower surface. This outweighs the growth of negative shear stress on the upper surface due to the separated flow (to be discussed later). Thus the net integrated skin friction drag increases during the period: $0 < t < 0.32$.

During the rest of the upstroke motion ($0.32 < t < 0.52$) the increase in the strength of the separated flow on the upper surface outweighs the increase in the surface shear stress strength on the lower surface; therefore, the skin friction drag decreases in magnitude during this period.

During the time period $0.6 < t < 1.04$, the variation in skin friction drag is due to two different effects. As the angle of attack decreases, the surface vorticity over most of the airfoil tends to decrease, causing the viscous drag to decrease. However, the separated flow region decreases in strength during downstroke, and finally disappears at $t \simeq 1.0$, and the negative shear stress produced by the reversed flow decreases in magnitude as well. This effect tends to increase the viscous drag. Thus, the two opposing effects give rise to the complex behavior of C_{D_f} during the above period.

The total drag variation is presented in Figure 60. In the present case, as in Cases 1 and 2, the viscous drag is the major contributor.

The total drag coefficient reaches a maximum value of 0.13 in the present case. It is found that the total drag values in the present case are somewhat higher than the total drag values in Cases 1 and 2, mainly because Cases 1 and 2 involve small mean angle of attack and amplitude. The large variation in angle of attack in Case 3 leads to noticeable separation over most of the upper surface. In cases 1 and 2, the separation was confined to the trailing edge region, and since the region of separation was very small, it did not affect the integrated loads significantly. In the present case, the numerical results show the following sequence of events on the upper surface during the first cycle.

Immediately after the start, a strong trailing edge separation is observed, the flow separating from the trailing edge region on the upper surface near the station $\frac{x}{L} = .75$ (Figure 61). As the angle of attack increases, at t = .16, it is seen that the region of recirculation increases in size, as shown in Figure 62. The vorticity contour plot (on the upper half of Figure 62) shows that vorticity is being shed from the trailing edge. At t = 0.4 , as shown in Figure 63, the separation point has moved upstream on the upper surface. Some of the stream lines in the recirculating region form a closed bubble as seen in the figure. In addition the vorticity contour plot shows that the vorticity shed near the trailing edge region has diffused over a larger region. At t = 0.52, as shown in Figure 64, the airfoil reaches its maximum angle of attack (15^{o}), and there is a strong recirculation phenomenon taking place on the upper surface at this time level. The closed loop near the trailing edge in the vorticity contour plot in Figure 64 represents a part of the shed vorticity. Since during the upstroke, the fluid near the

trailing edge appears to move in the vertical direction (y direction) relative to the trailing edge, this vorticity field is noticeably displaced in the y direction. Its effect is also noticed in the streamline plot, as the stream line curvature is seen to increase sharply near this shed vortex. After t = 0.52, as the angle of attack decreases, the separated flow region begins to decrease in size as seen in Figures 65 and 66. In Figure 65, the movement of the shed vortex away from the trailing edge is also seen. The separation bubble finally disappears at t = 0.96, near the end of the downstroke.

The phenomenon of dynamic stall, as explained earlier, was not observed during the present study.

The following phenomena distinguish Case 3 from Cases 1 and 2.

(1) The inertial effects in Case 3 are substantially stronger than in Cases 2 and 1 because of the large amplitude of oscillations, and the high reduced frequency.

(2) A strong separation bubble appears in Case 3, while the separation phonomenon in Case 1 and 2 is restricted to the trailing edge region .

(3) The drag variation in Case 3 is significant compared to Cases 1 and 2 mainly due to the large variation in the angle of attack.

CHAPTER VI

CONCLUDING REMARKS

In the preceding chapters, a numerical procedure has been developed to study viscous flow past arbitrary bodies undergoing arbitrary motion. This procedure has been applied to the study of viscous flow over airfoils undergoing oscillatory pitching motions. Based on the numerical results, an attempt has been made to explain the physical and qualitative features of the flow phenomena.

The numerical procedure involves the following speical features that are not found in conventional finite difference schemes.

(1) A hybrid finite element-finite difference scheme has been developed for the treatment of the vorticity transport equation in the physical plane. This scheme makes use of all the attractive features that finite element schemes offer, when applied to an irregular region, while retaining the flexibility and simplicity of the finite difference techniques in the uniform outer region.

(2) A highly accurate surface vorticity scheme has been developed. This scheme can handle any arbitrary motion of the body. This scheme makes use of analytical integration techniques wherever possible so that the inaccuracies associated with the numerical integration techniques do not affect the accuracy of the solution. While using this method, it is possible to confine the calculations to the vis-

cous region alone.

(3) This method makes use of an integral relationship for velocity, available in open literature. This integral relationship is explicit, and therefore needs to be applied only to the nodes in the viscous region. In addition this integral relationship provides several attractive alternatives for calculating the velocity in the flow field rapidly and accurately. Some of these alternatives are explained in References 29, 30 and 31.

The main conclusions, drawn from the study of the three cases involving viscous flow over oscillating airfoils, are the following:

(1) The lift coefficient leads the angle of attack in phase. As the angle of attack increases, the cumulative effect of vorticity gradient and angular acceleration effect leads to a large increase in pressure over the upper surface relative to the trailing edge. As a result C_L begins to decrease even before the maximum angle of attack is reached. For similar reasons, $C_{L_{min}}$ is reached even before the minimum angle of attack is reached.

(2) The moment variation with angle of attack leads to positive aerodynamic damping in all the cases considered.

(3) The stall effects diminish at high reduced frequencies.

(4) The maximum C_L shows considerable overshoot over the static $C_{L_{max}}$ for the same angle of attack.

(5) For low amplitude oscillations, the viscous drag is relatively insensitive to the pitching motion. Whenever no substantial separation effects occur the viscous drag is the chief contributor to the total drag.

Because of the large number of combinations that are possible between the flow parameters--Reynolds number, mean angle of attack, amplitude of motion and reduced frequency--the three cases considered in the present study serve only as characteristic examples that highlight some of the flow properties associating with the oscillating airfoil. The good qualitative agreement with potential flow theory, however, gives the necessary confidence to extend the present scheme to other flow situations as well. It is hoped that the present work will provide an effective basis for studying the more complex dynamic stall phenomenon.

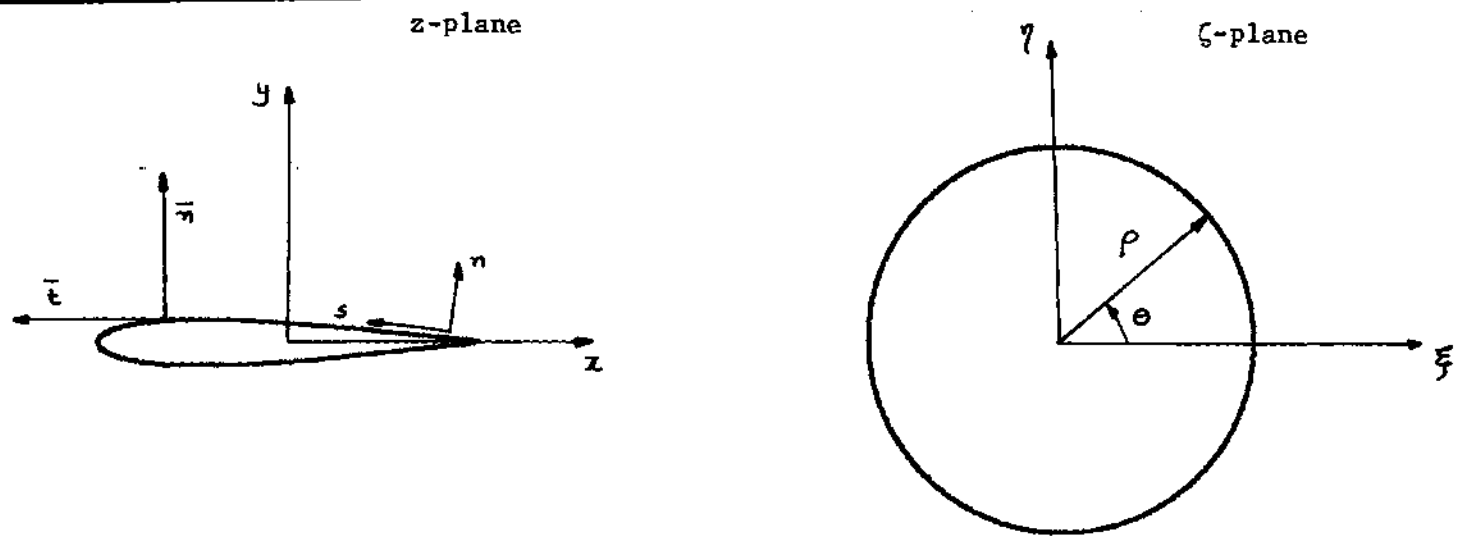

$$z = f(\zeta)$$

$$H = \left|\frac{dz}{d\zeta}\right|$$

Figure 1. Details of the Transformation

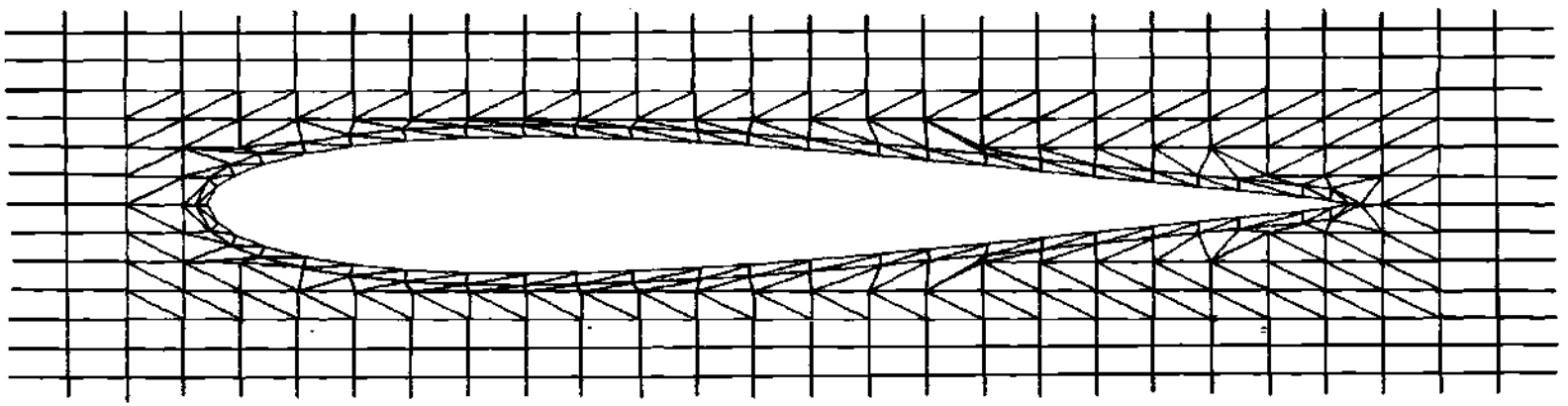

Figure 2. Inner Region of a Hybrid Grid System

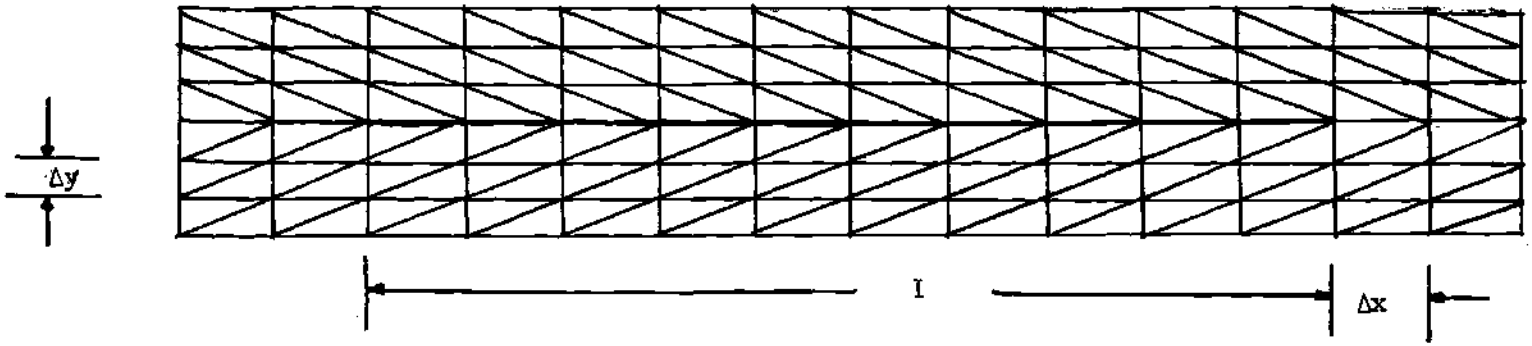

L . Length of Flat Plate

$\Delta x = .1\ L$

$\Delta y = .04\ L$

Figure 3. Flat Plate Problem-Finite Element Network

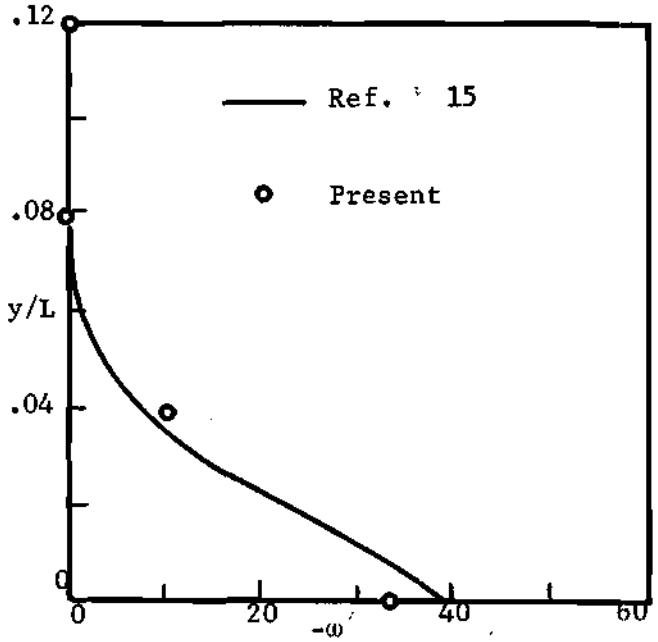

Figure 4a. Vorticity Profile at Mid-plate (t = .25)

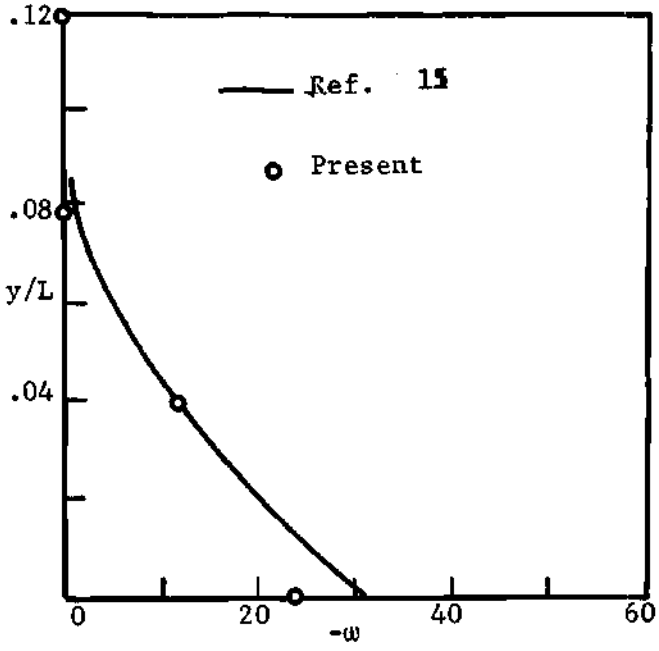

Figure 4b. Vorticity Profile at Mid-Plate (t = .5)

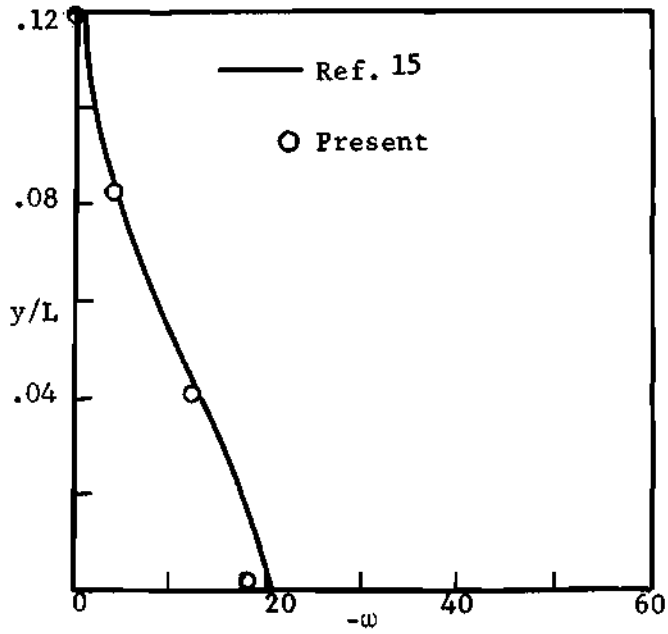

Figure 5a. Vorticity Profile at Mid-Plate (t = 1.5)

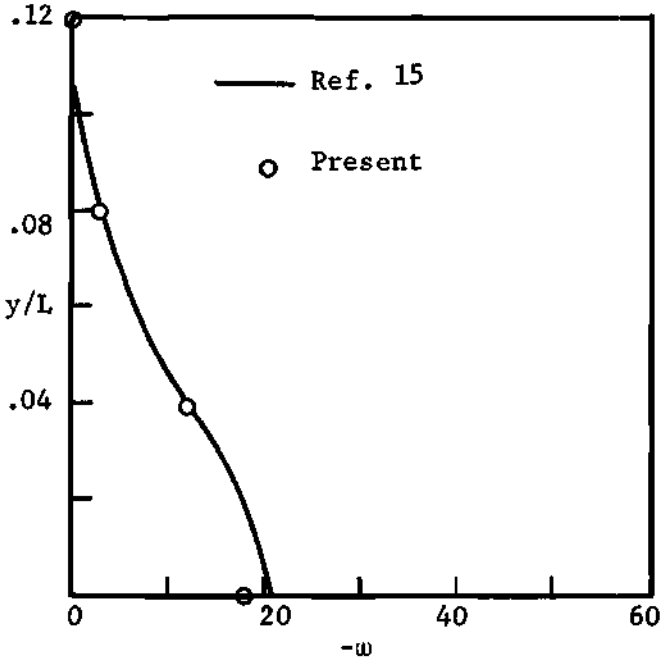

Figure 5b. Vorticity Profile at Mid-Plate (t = 1.0)

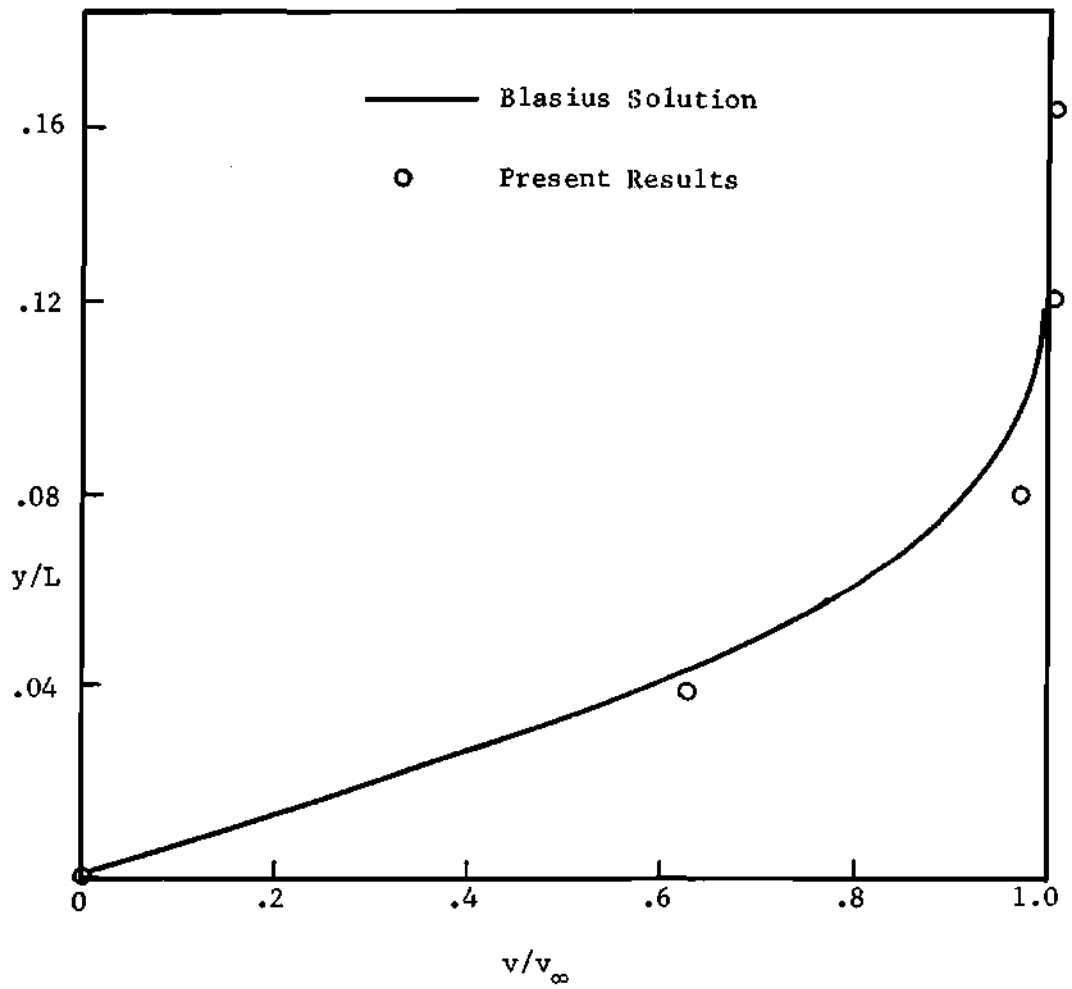

Figure 6. Flat Plate Problem--Mid-Plate Velocity Profile at Later Time Levels

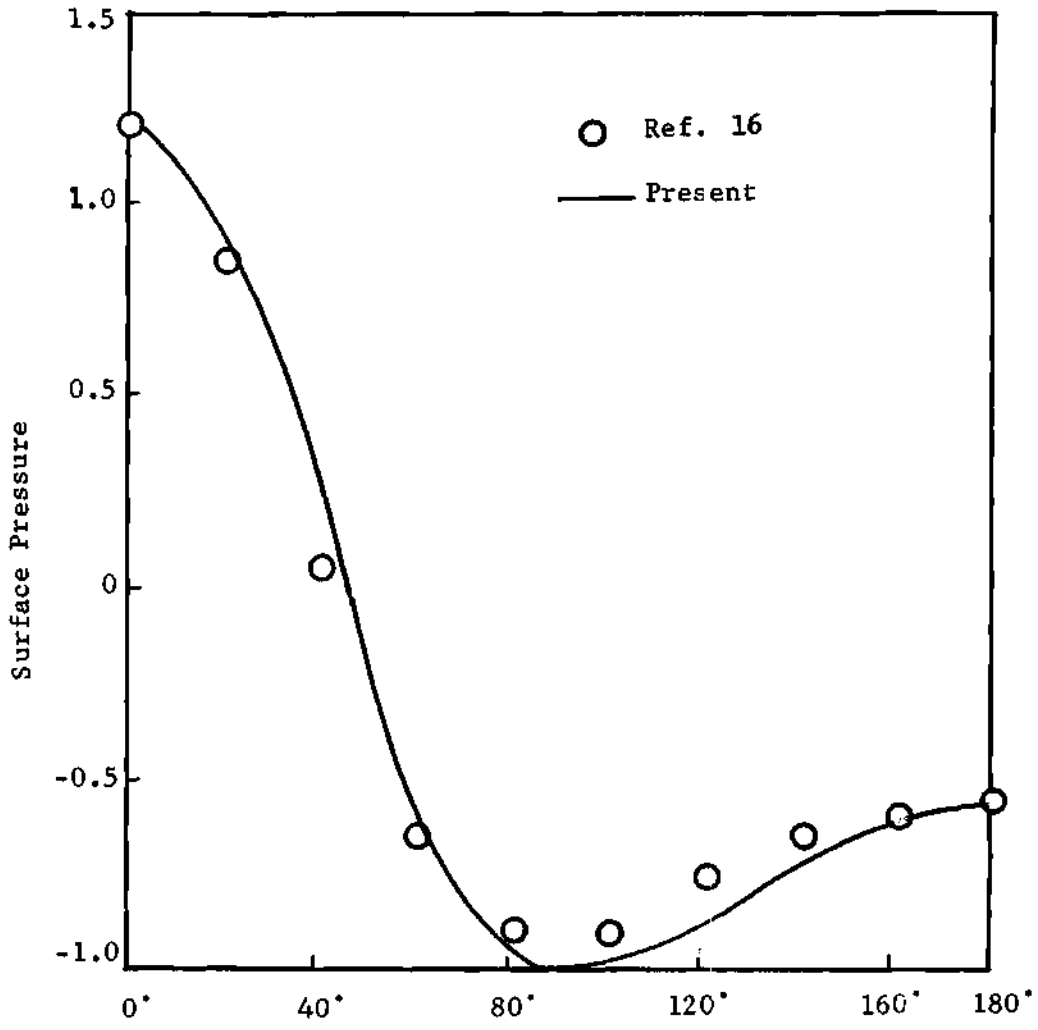

Figure 7. Circular Cylinder Surface Pressure Distribution at Later Time Levels

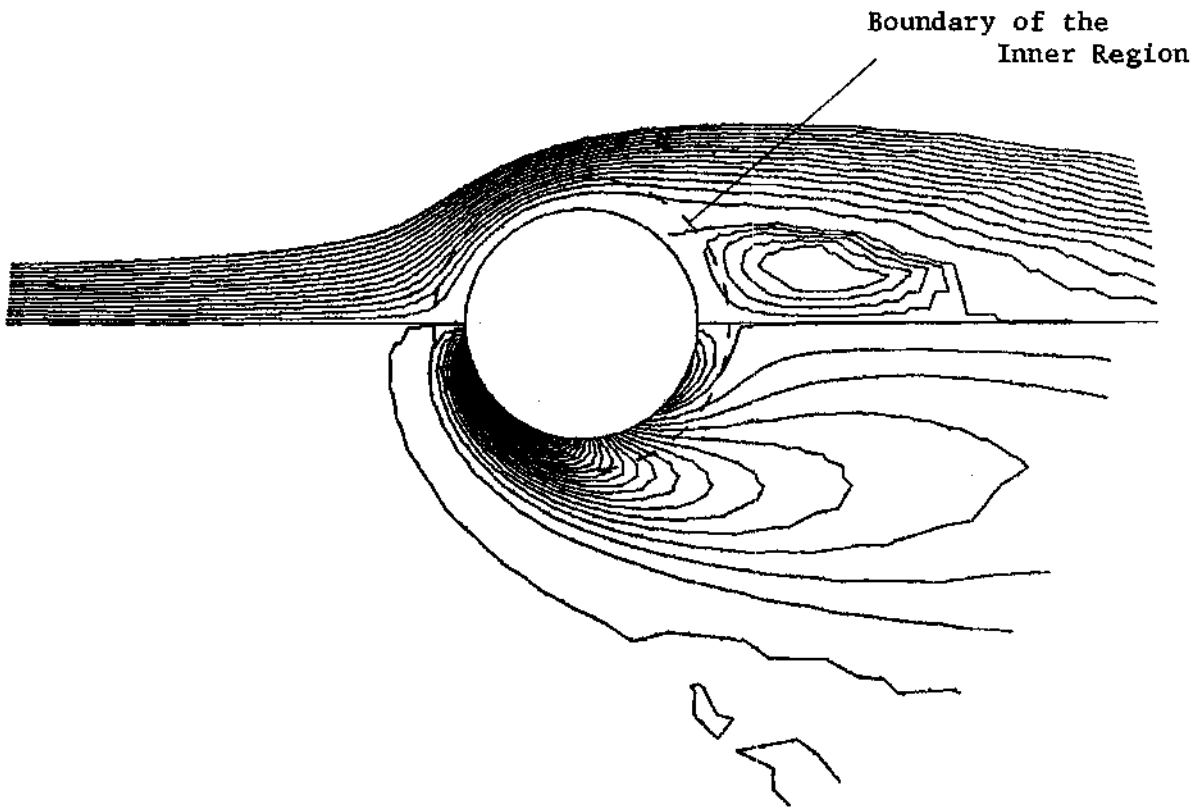

Figure 8. Streamlines and Constant Vorticity Contours For Viscous Flow Past a Circular Cylinder

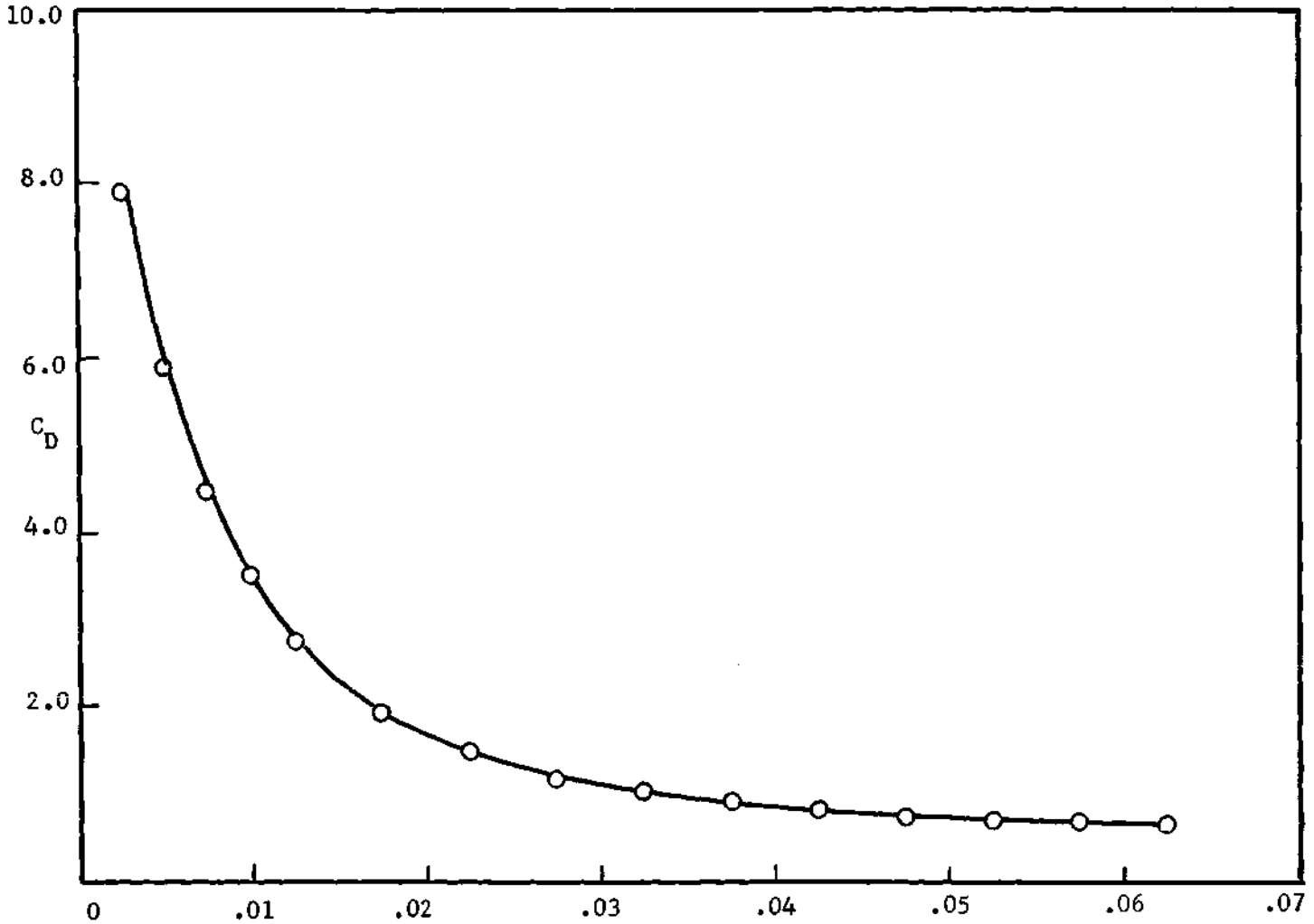

Figure 9. Joukowski 12°/. Airfoil at Zero Angle of Attack-Drag History for Early Time Levels

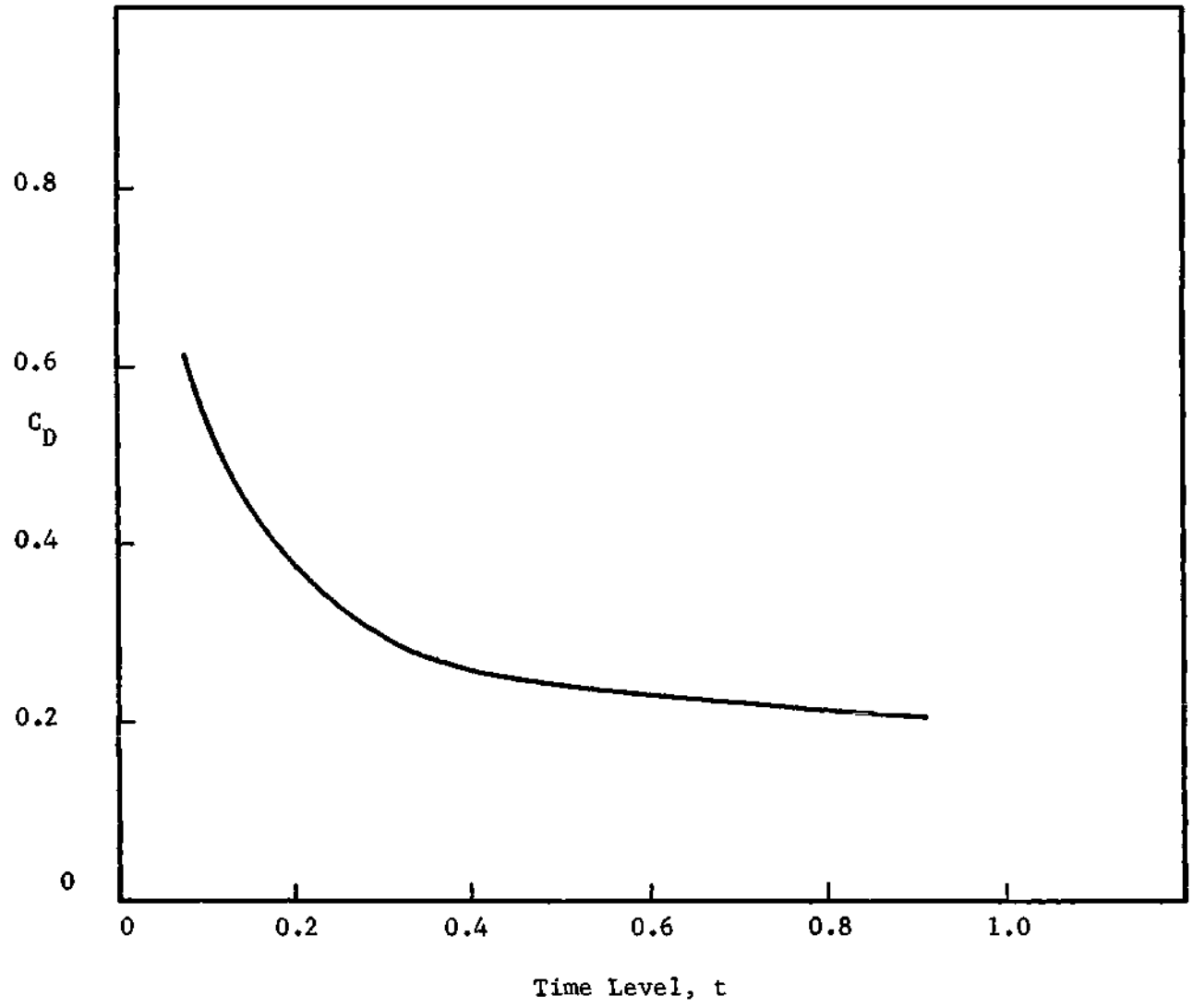

Figure 10, Joukowski 12°/. Airfoil at Zero Angle of Attack-Drag Variation at Later Time Levels

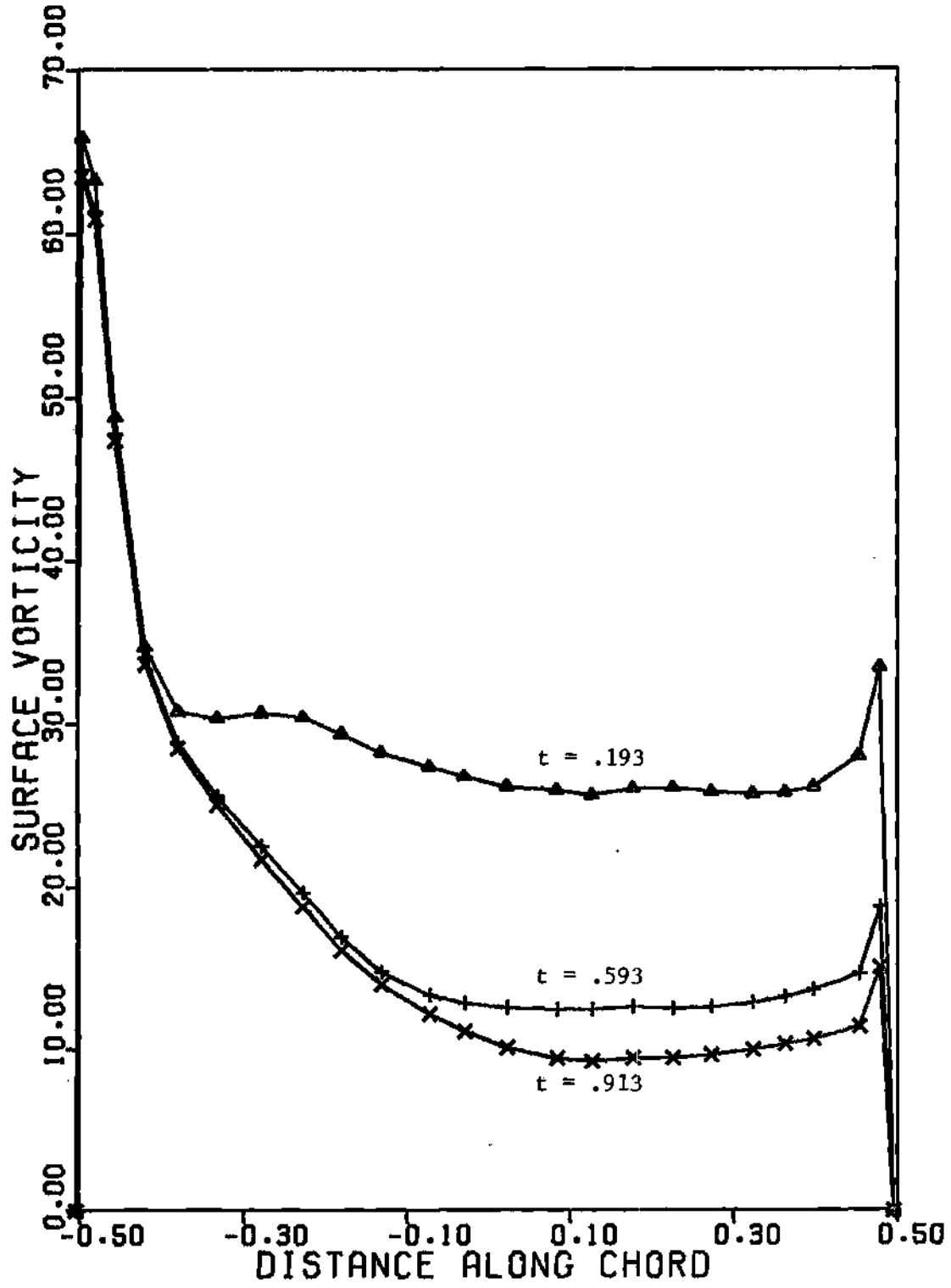

Figure 11. Joukowski 12°/. Airfoil at Zero Angle of Attack-Surface Vorticity Distribution at Selected Time Levels

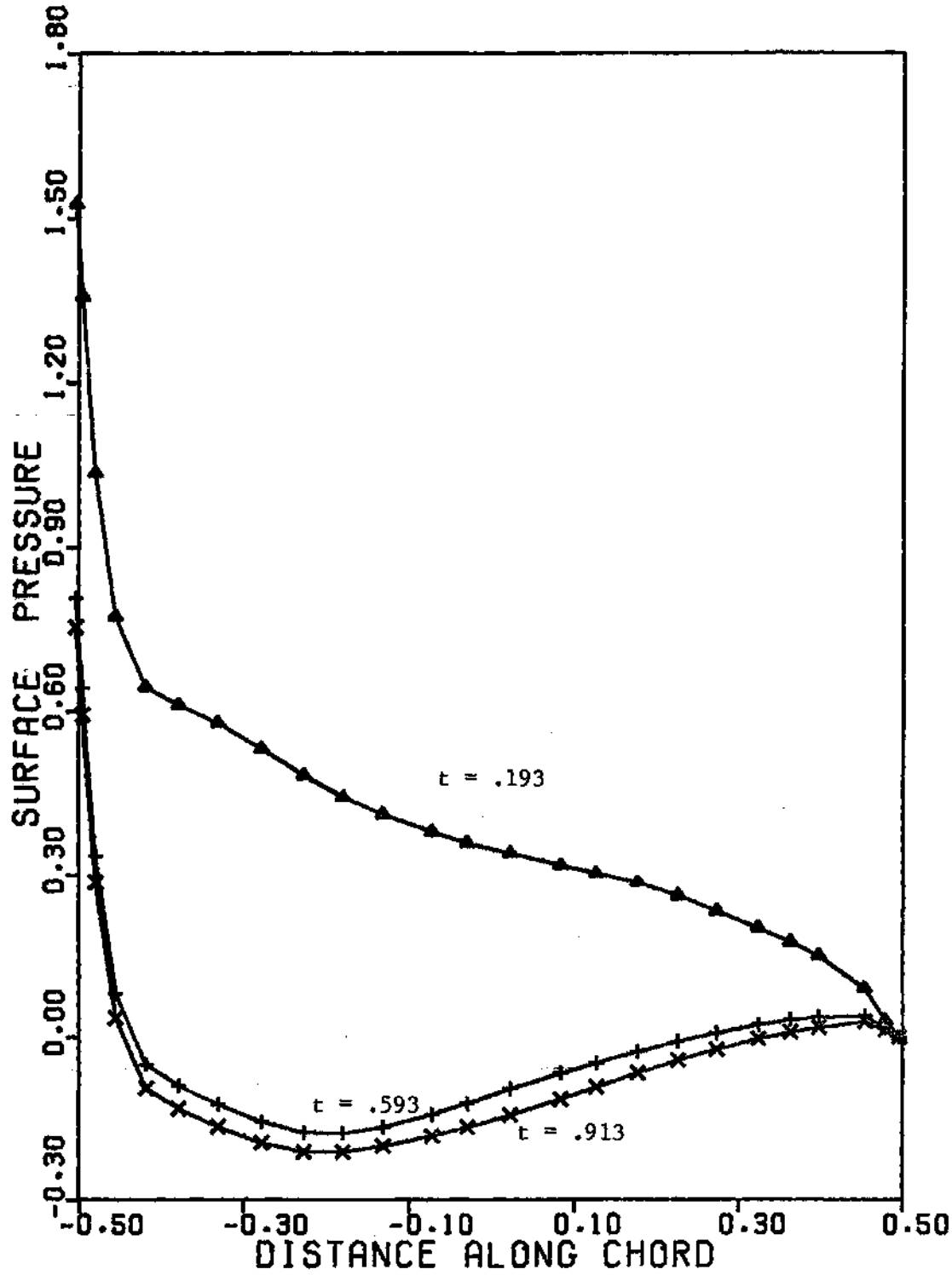

Figure 12. Joukowski 12'/. Airfoil at Zero Angle of Attack-Surface Pressure Distribution at Selected Time Levels

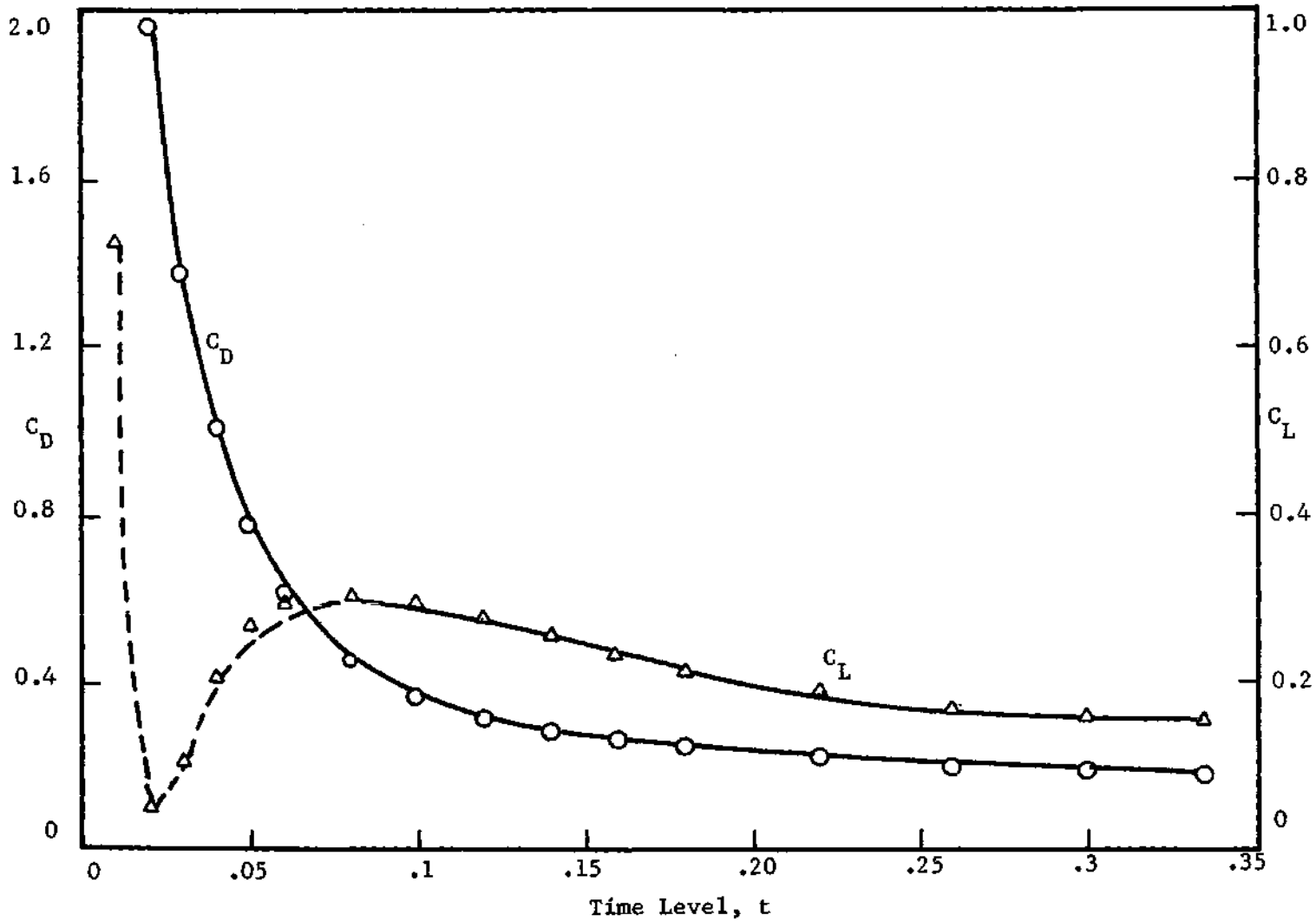

Figure 13. Joukowski 12°/. Airfoil at 3° Angle of Attack-Lift and Total Drag Variation at Early Time Levels

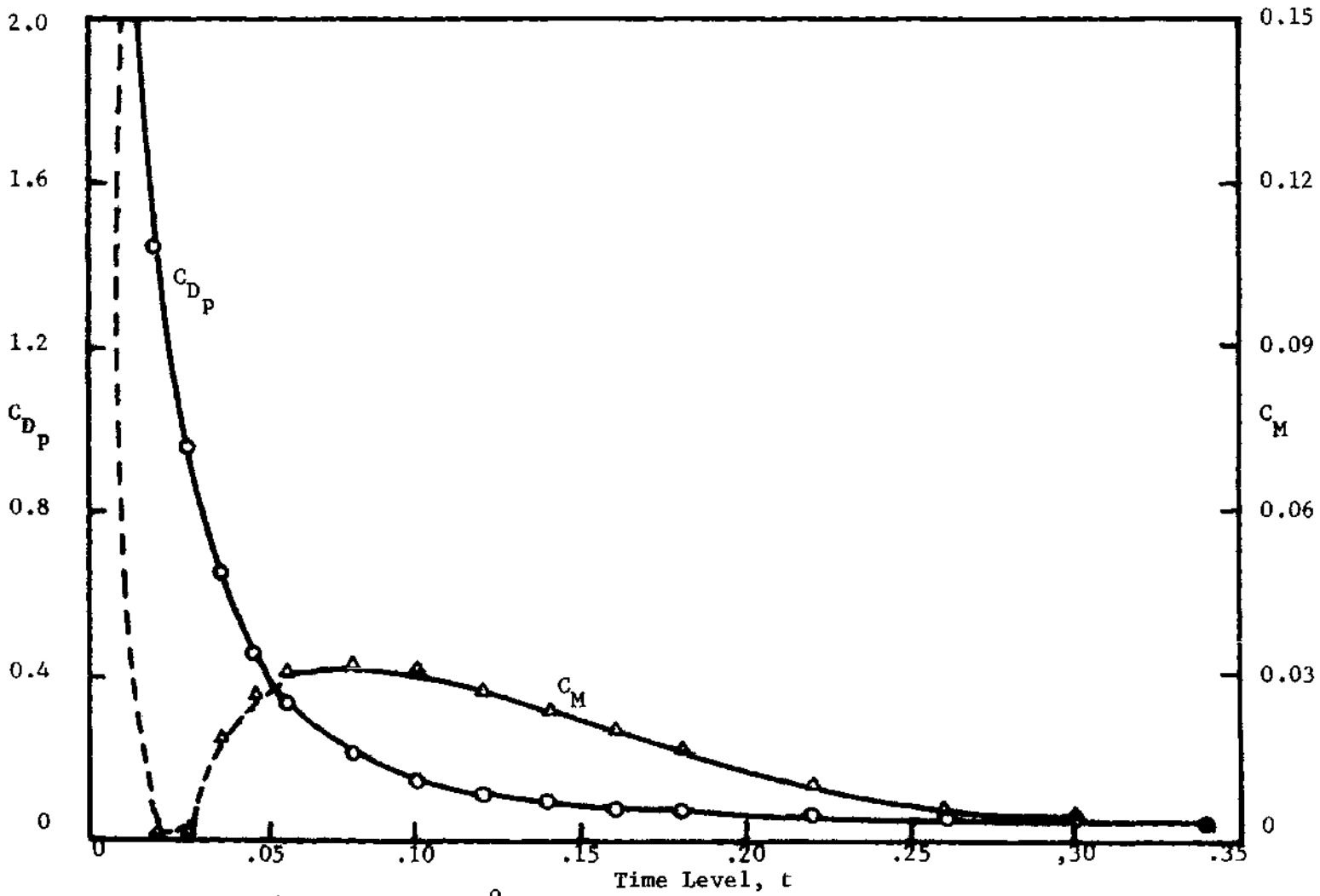

Figure 14. Joukowski 12*/. Airfoil at 3^{o} Angle of Attack-Pressure Drag and Moment Variation at Early Time Levels

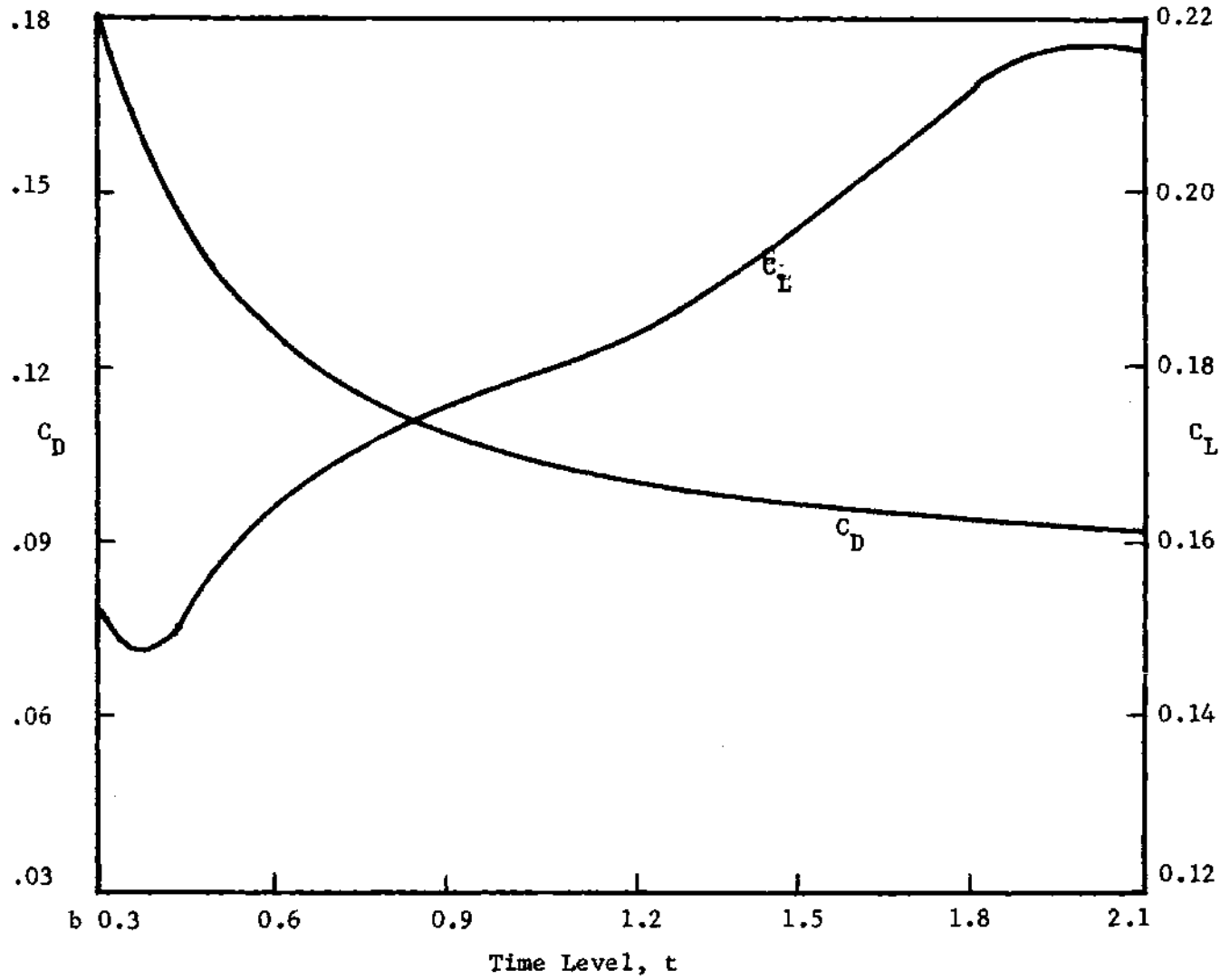

Figure 15. Joukowski 12'/. Airfoil at 3^{o}Angle of Attack-Lift and Drag Variation at Later Time Levels.

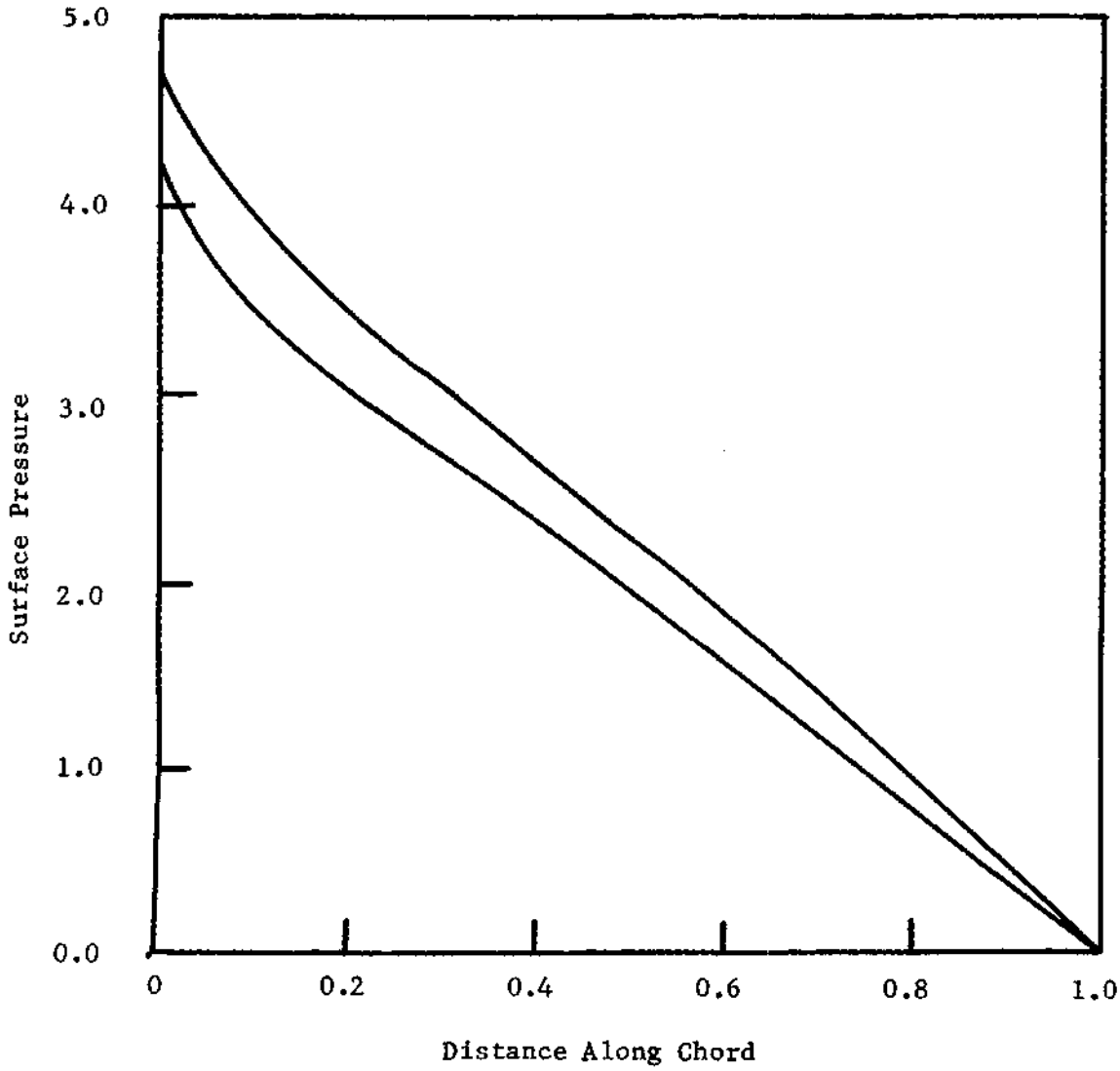

Figure 16. Joukowski 12%/. Airfoil at 3^{o} angle of Attack--Surface Pressure Distribution at t = .06

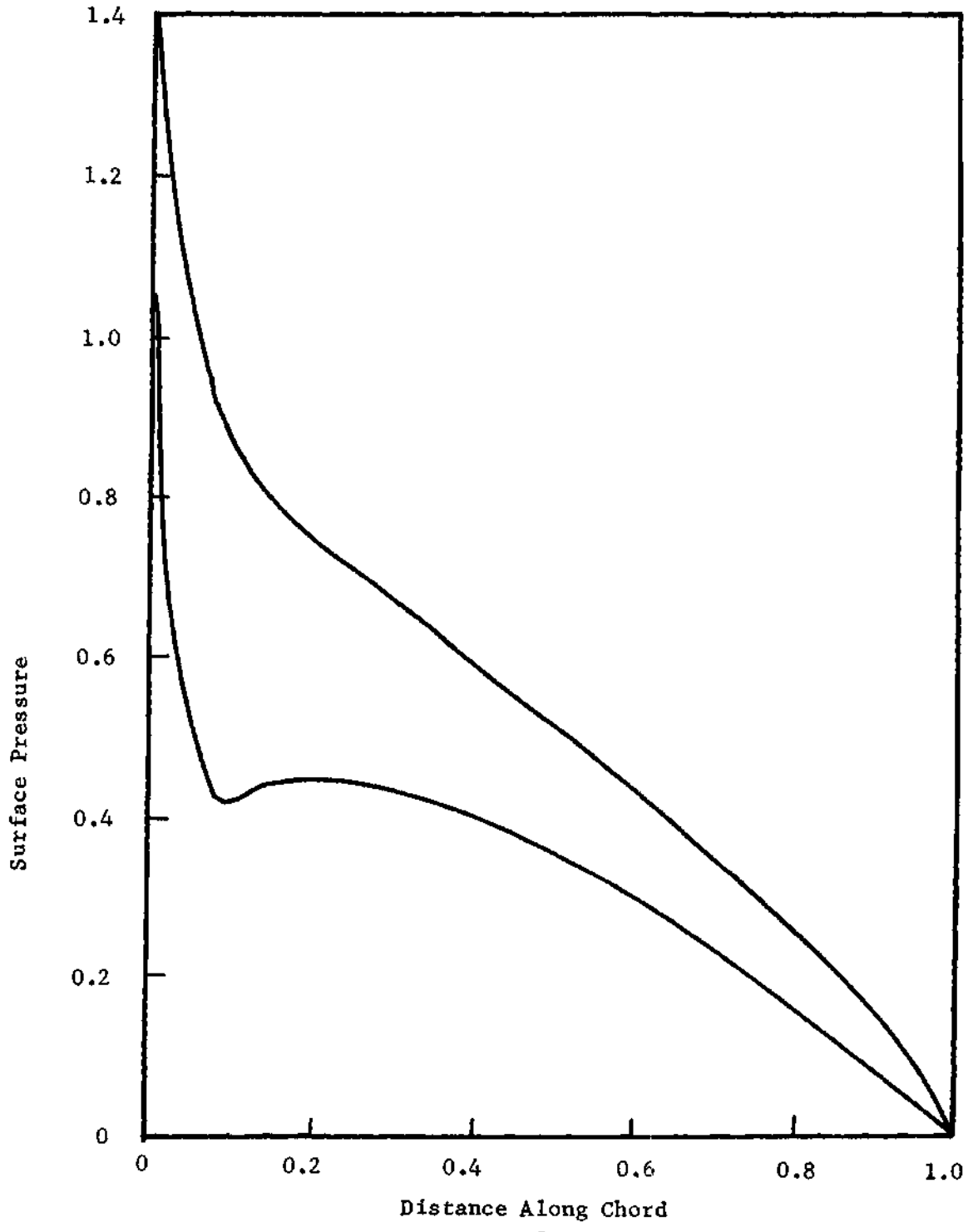

Figure 17. Joukowski 12%/. Airfoil at 3^{o} Angle of Attack--Surface Pressure Distribution at t = .18

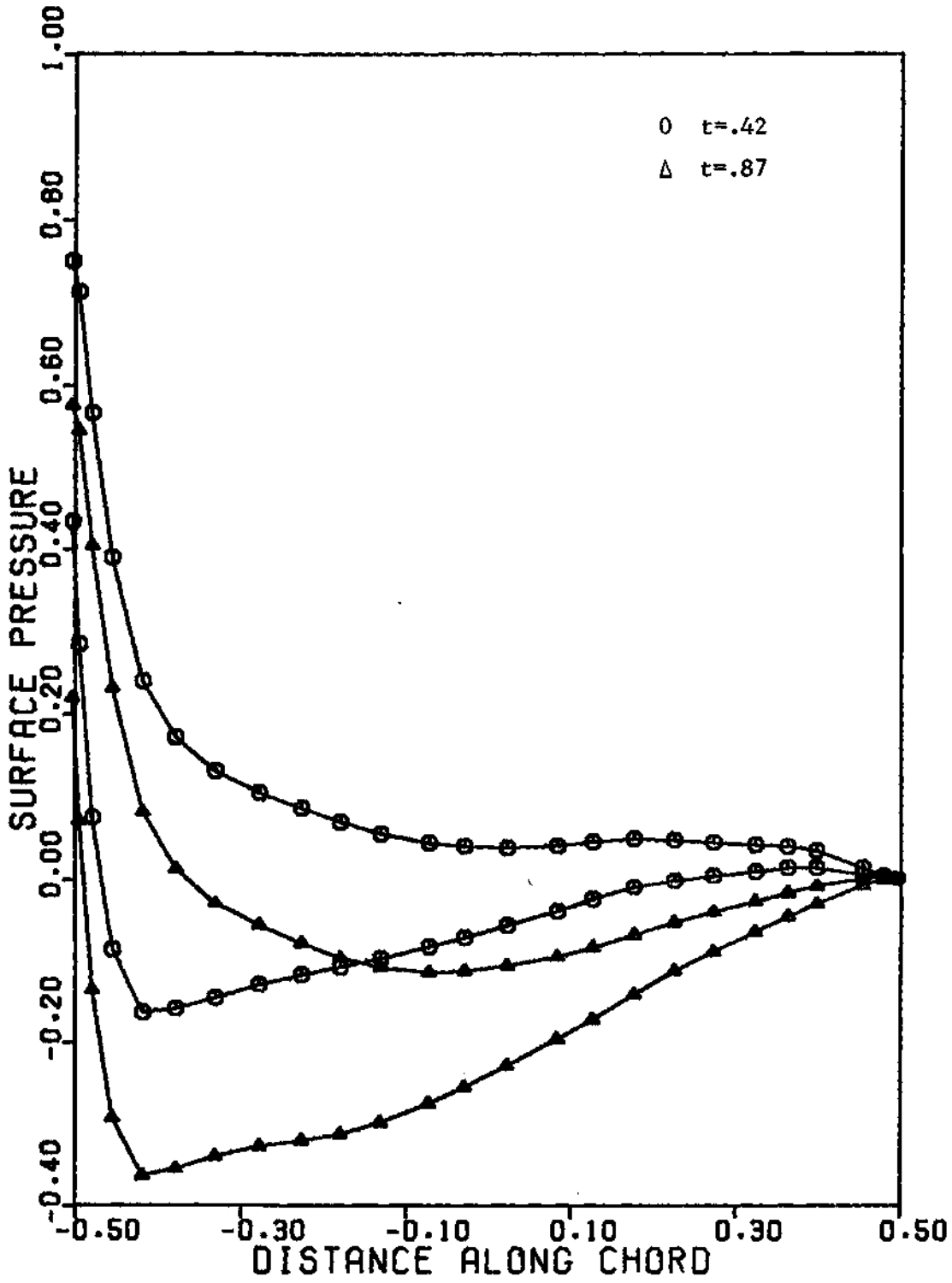

Figure 18. Joukowski 12%/. Airfoil at 3^{o} Angle of Attack--Surface Pressure Distribution at t = .42 and t = .87

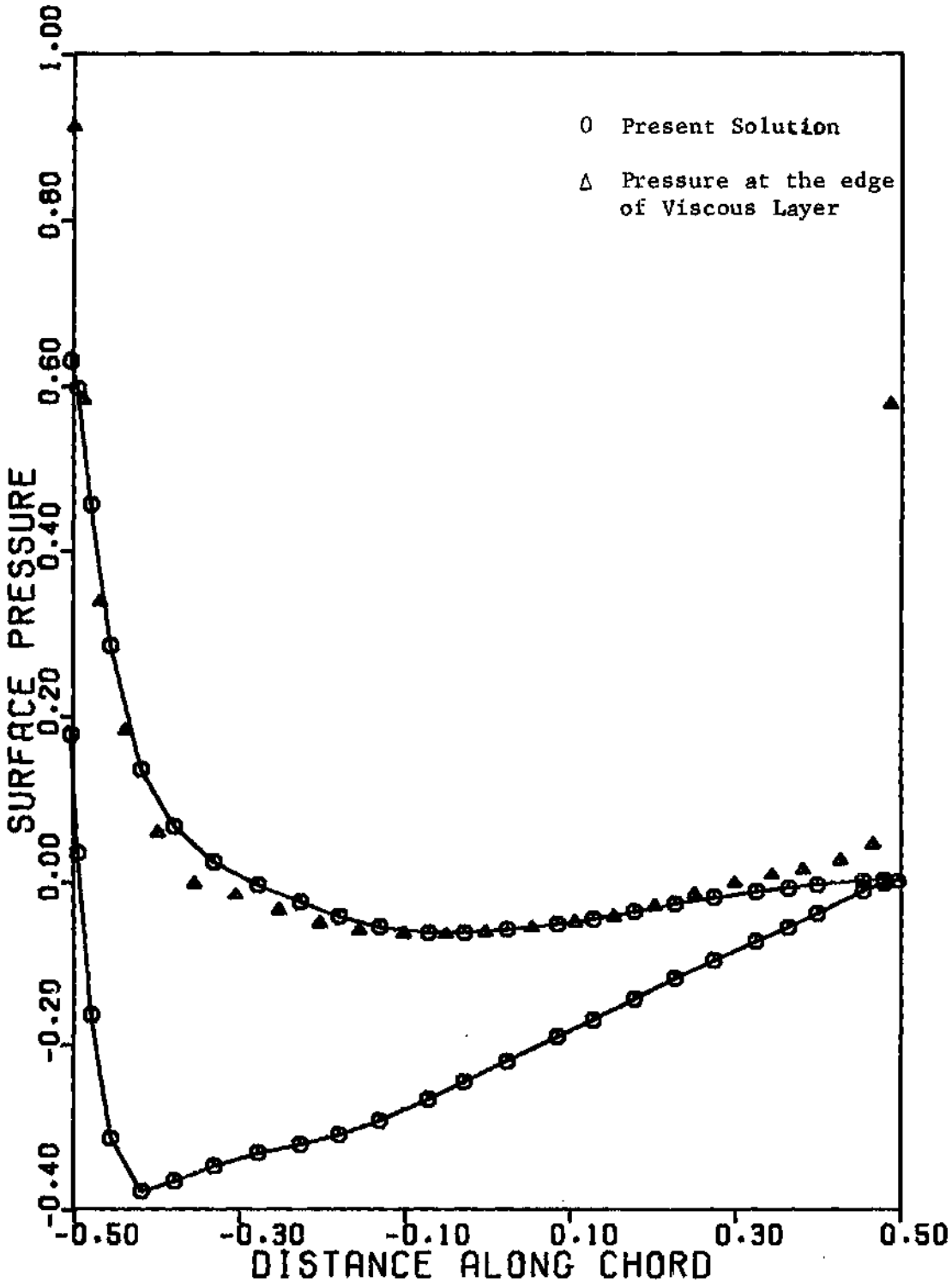

Figure 19. Joukowski 12%/.Airfoil at 3^{o} Angle of Attack--Surface Pressure Distribution at t = 2.07

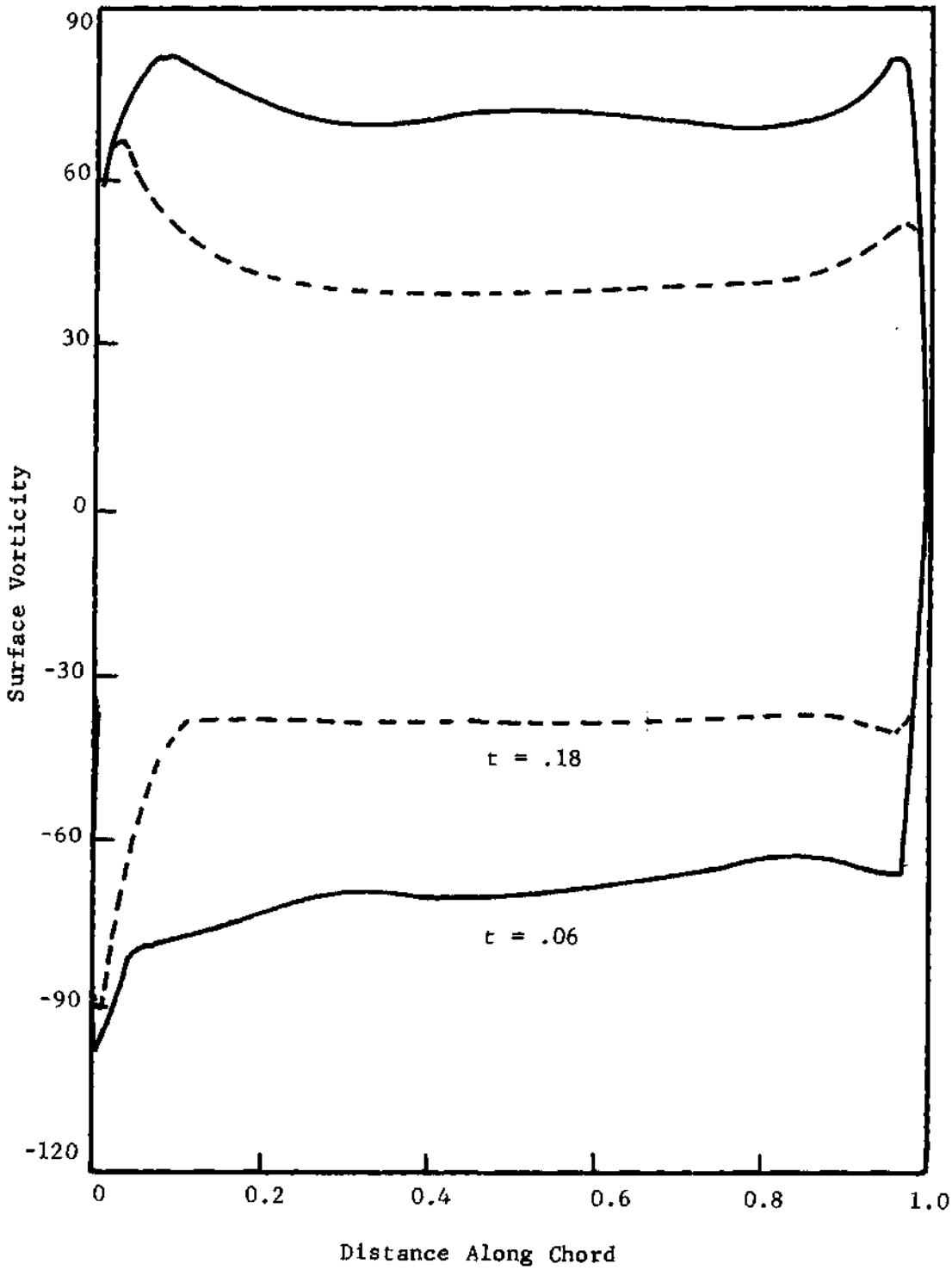

Figure 20. Joukowski 12%/.Airfoil at 3^{o} Angle of Attack--Surface Vorticity Distribution at t = .06 and t = .18

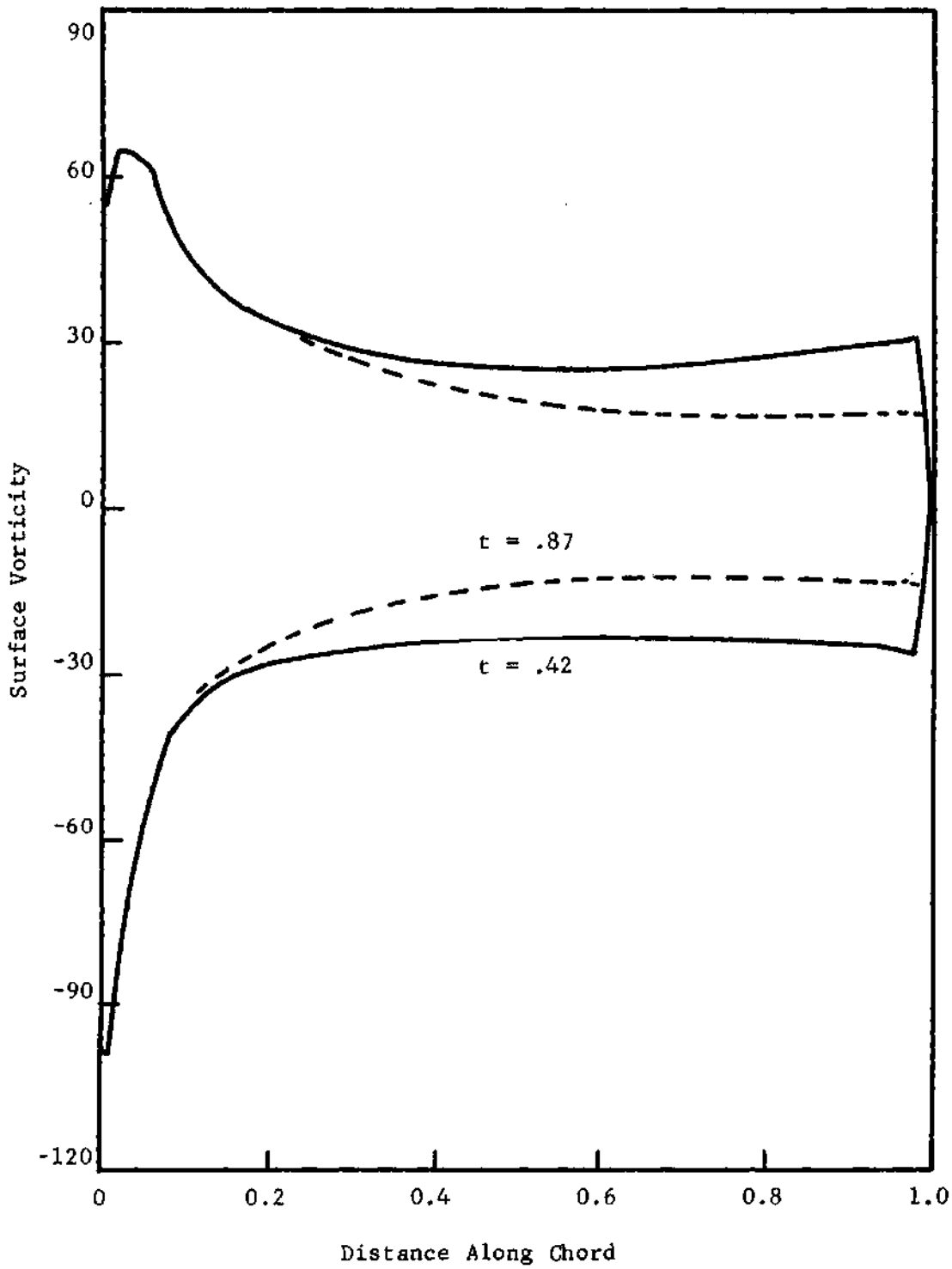

Figure 21. Joukowski 12'/.Airfoil at 3^{o} Angle of Attack--Surface Vorticity Distribution at t = .42 and t = .87

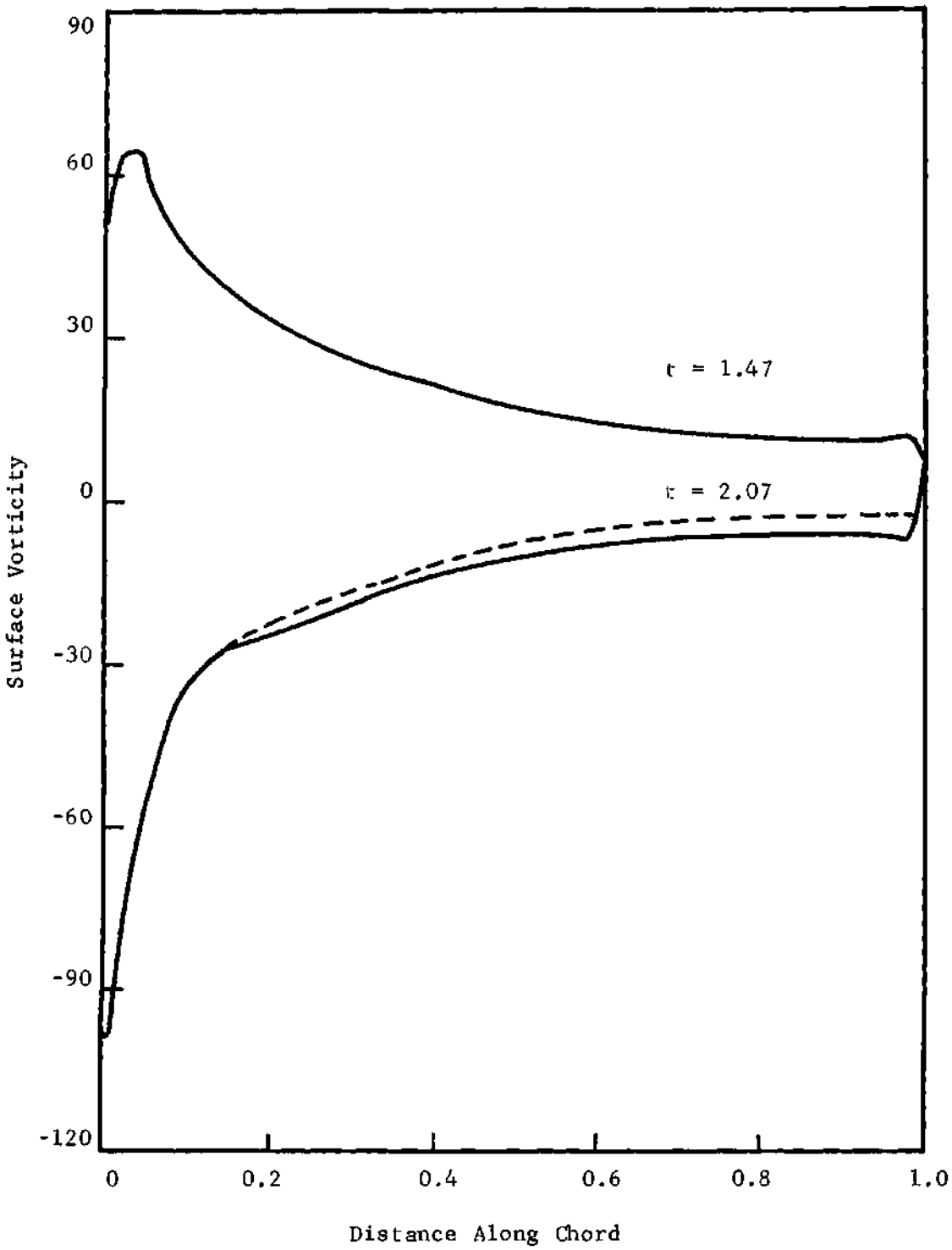

Figure 22. Joukowski 12%/.Airfoil at 3° Angle of Attack--Surface Vorticity Distribution at t = 1.47 and t = 2.07

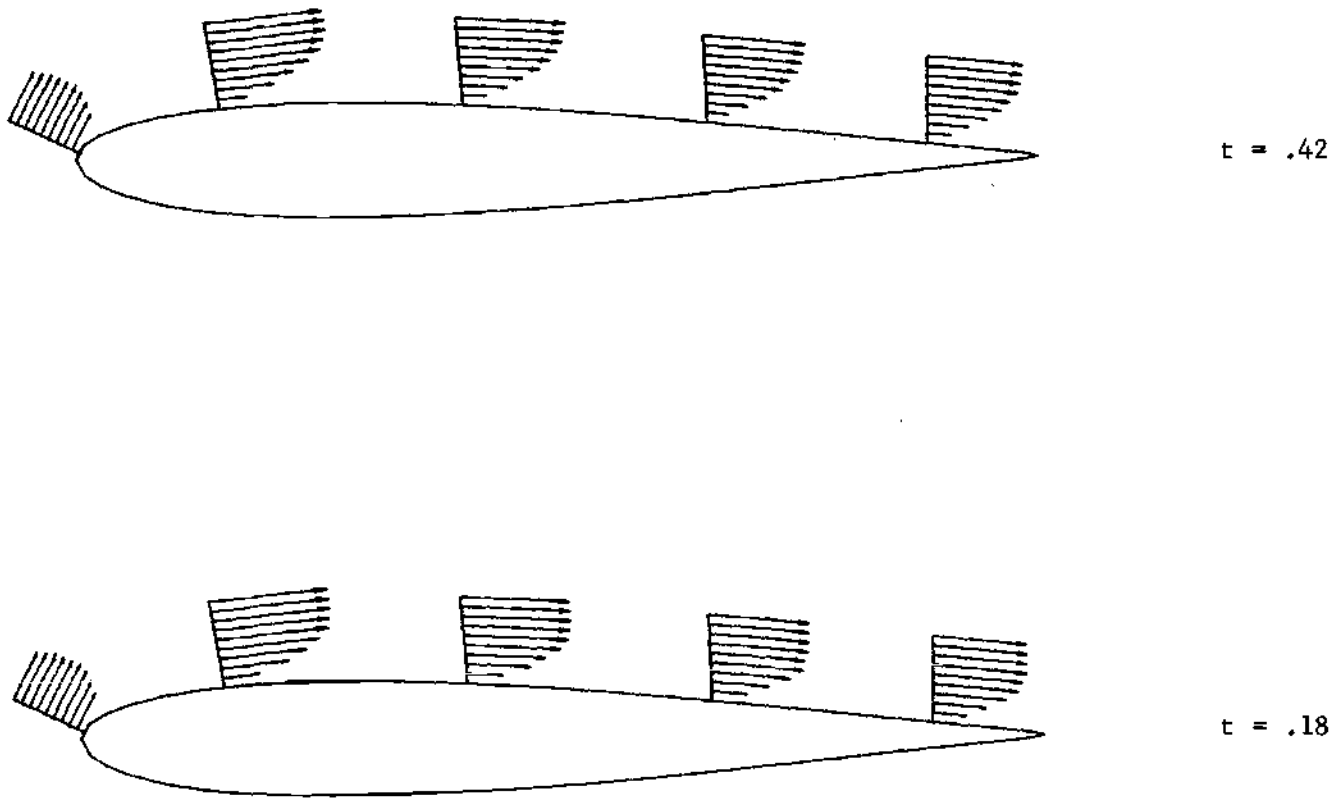

Figure 23. Joukowski 12'/.Airfoil at 3^{o} Angle of Attack - Velocity Profile at t = .18 and t = .42 at Selected Locations on the Upper Surface.

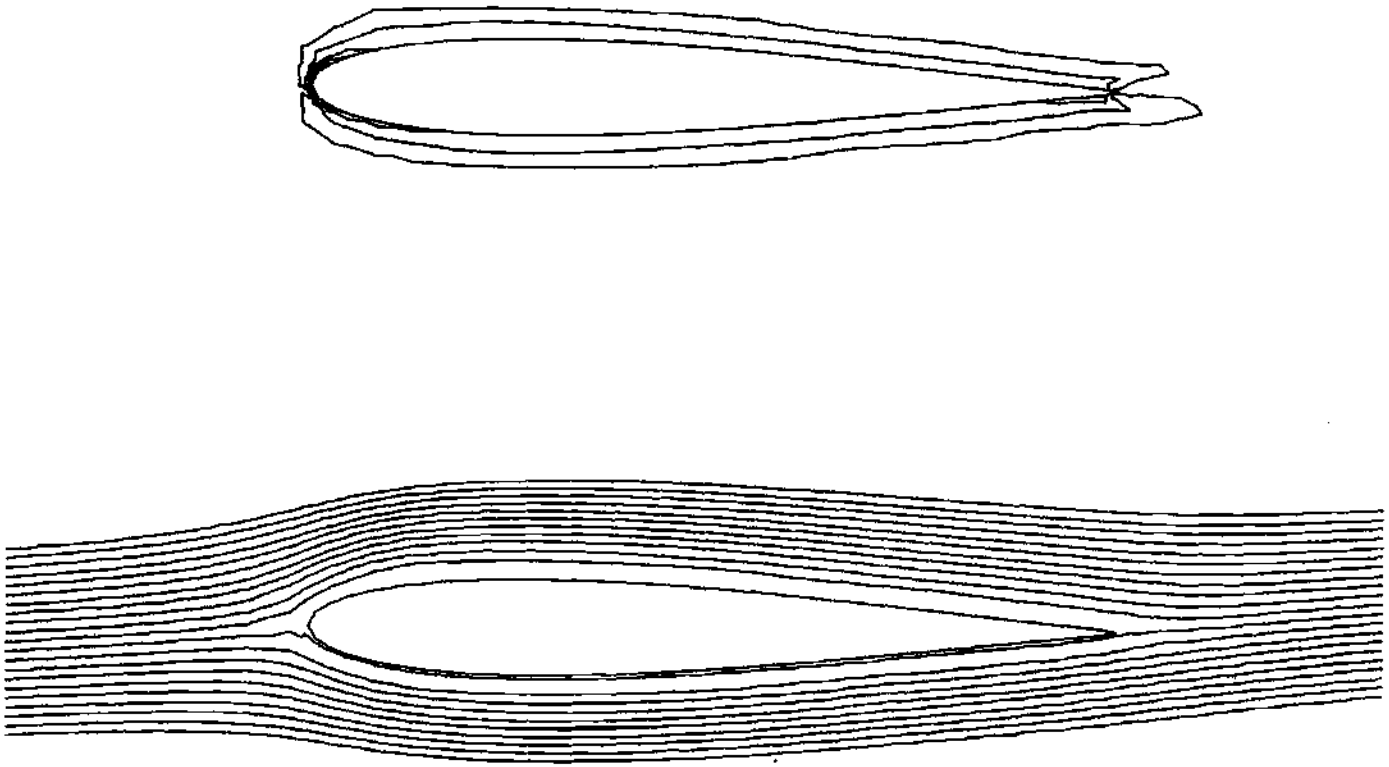

Figure 24. Joukowski 12'/.Airfoil at 3^{o} Angle of Attack - Streamlines and Constant Vorticity Contours at t = .18.

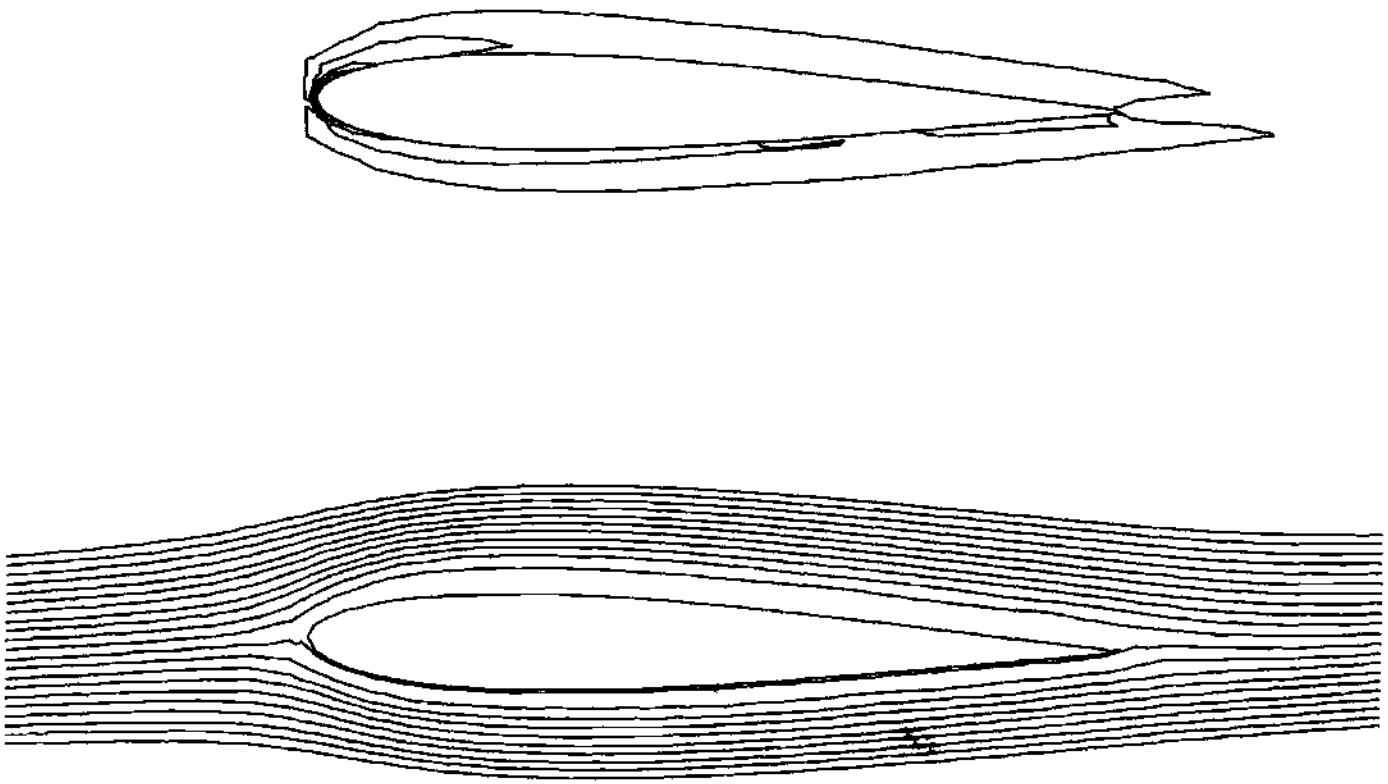

Figure 25. Joukowski 12%/.Airfoil at 3° Angle of Attack--Streamlines and Constant Vorticity Contours at t = .42

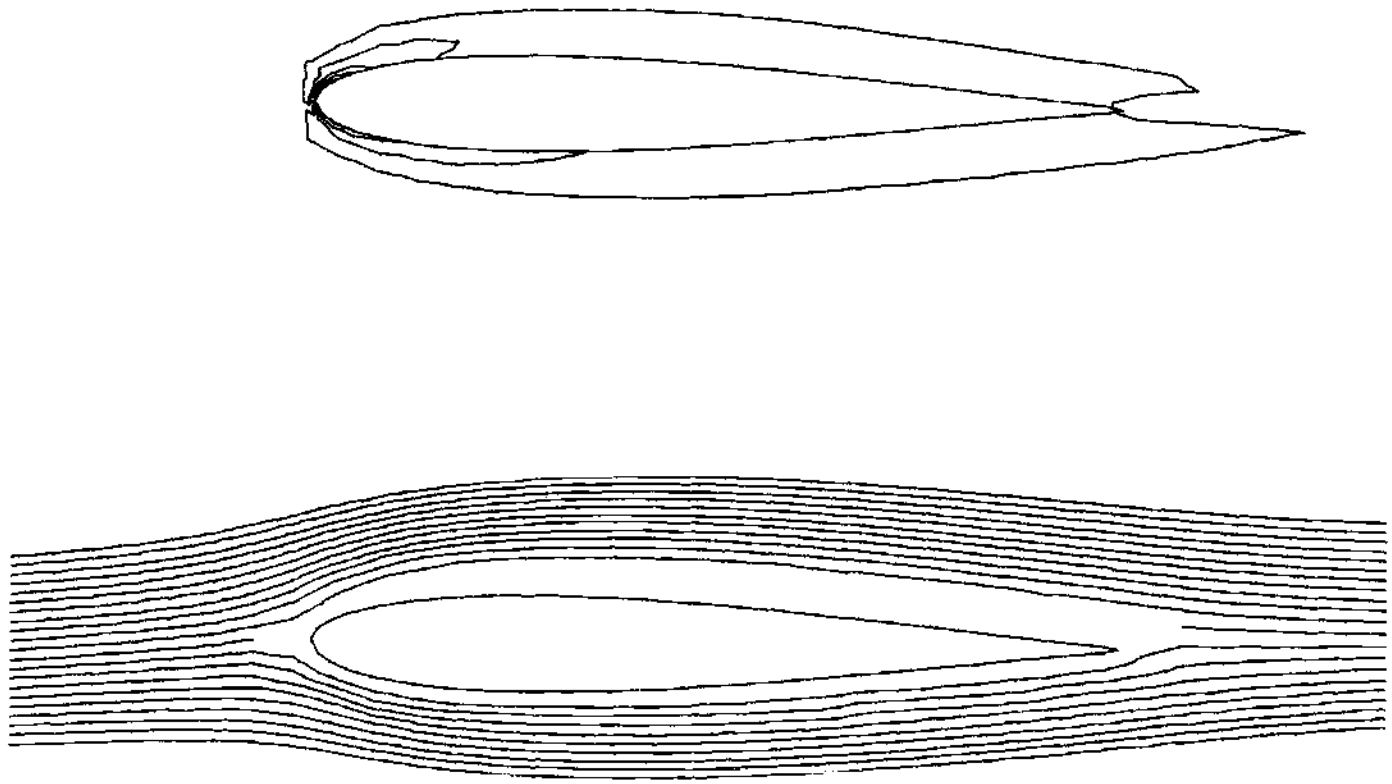

Figure 26. Joukowski 12% Airfoil at 3° Angle of Attack-- Streamlines and Constant Vorticity Contours at t = 0.87

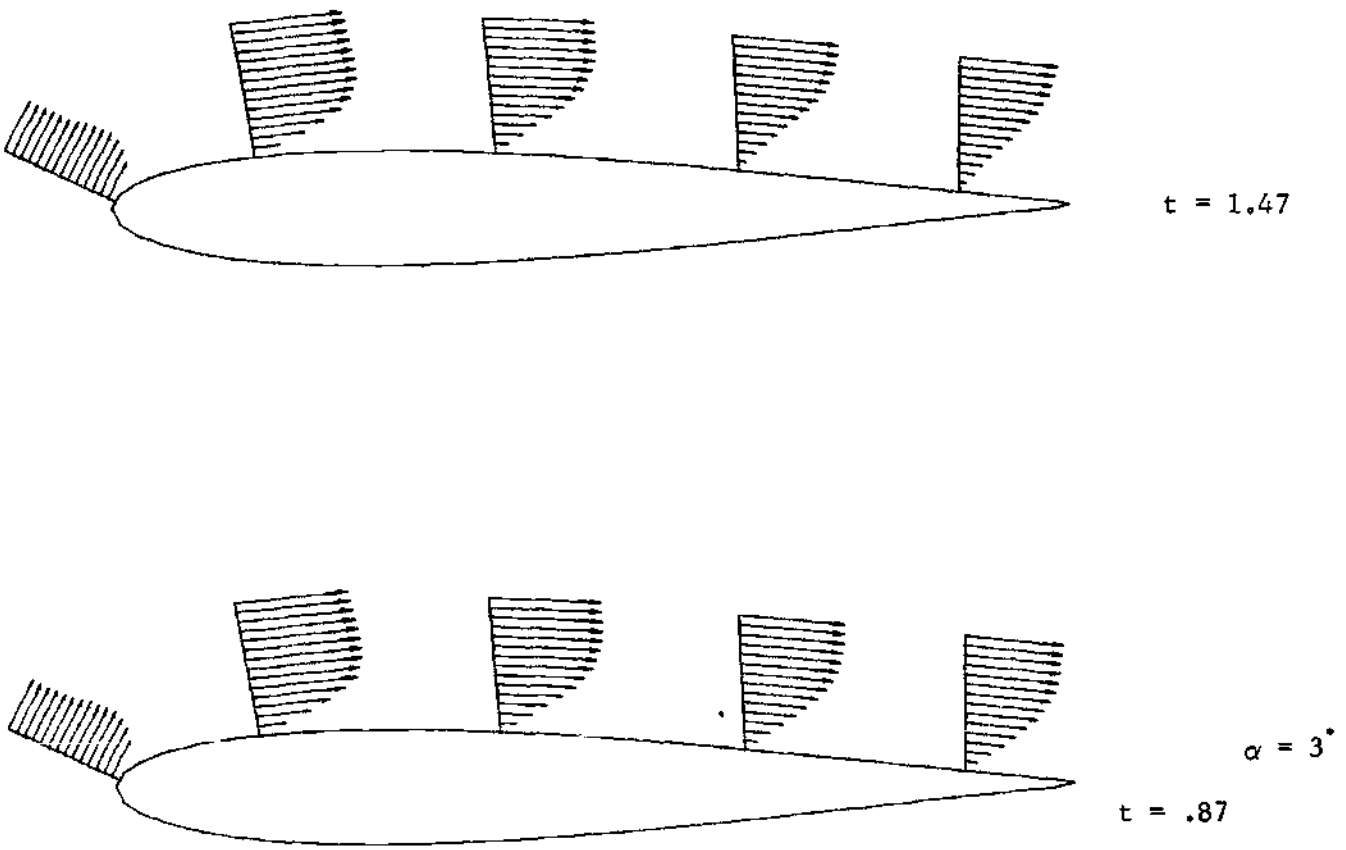

Figure 27. Joukowski 12°/. Airfoil at 3° Angle of Attack--Velocity Profiles at t=.87 and t=1.47 at Selected Locations on the Upper Surface

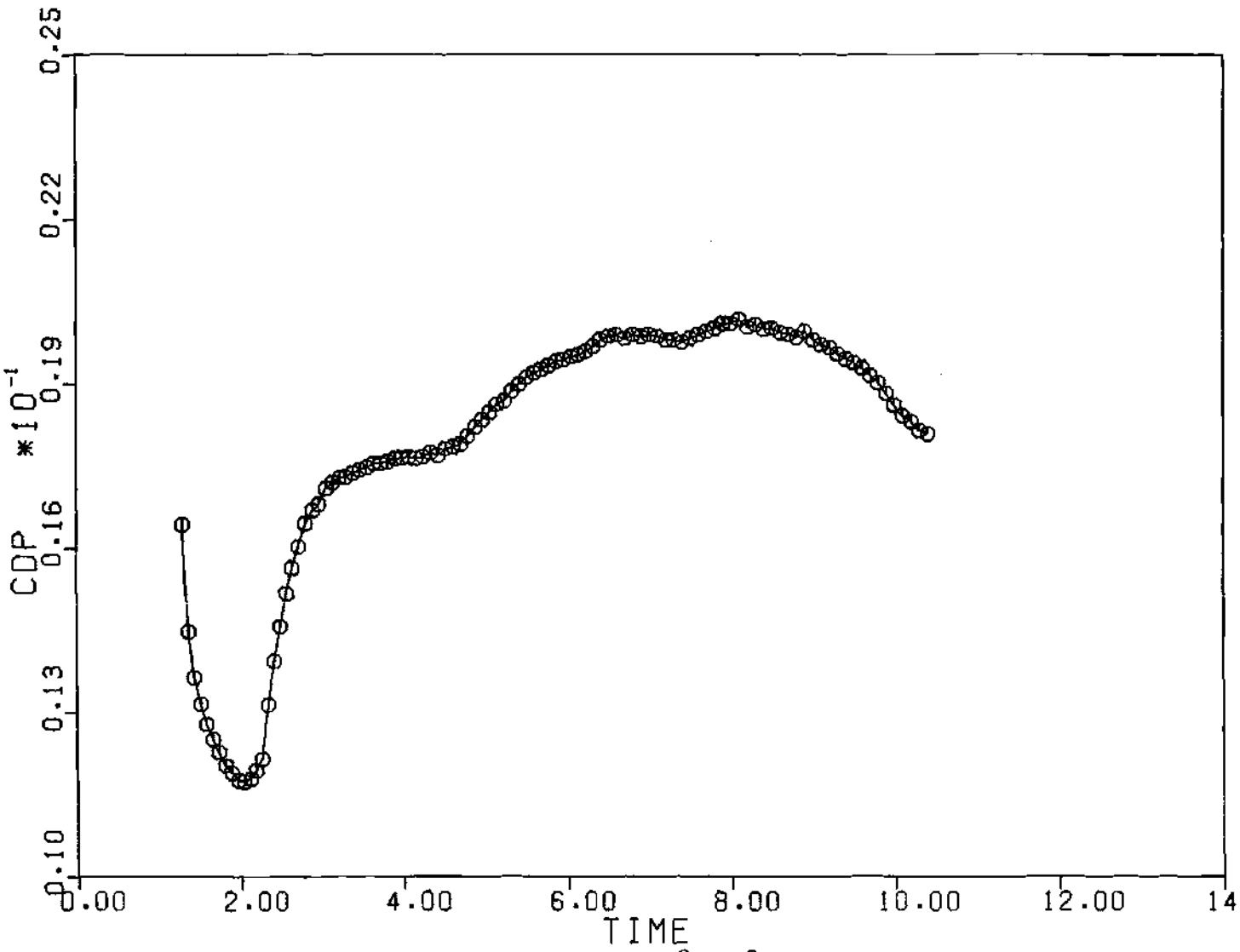

Figure 28. Joukowski 12% Airfoil ($\alpha = 3^{\circ} + 1^{\circ} \sin .6t$)--Pressure Drag History

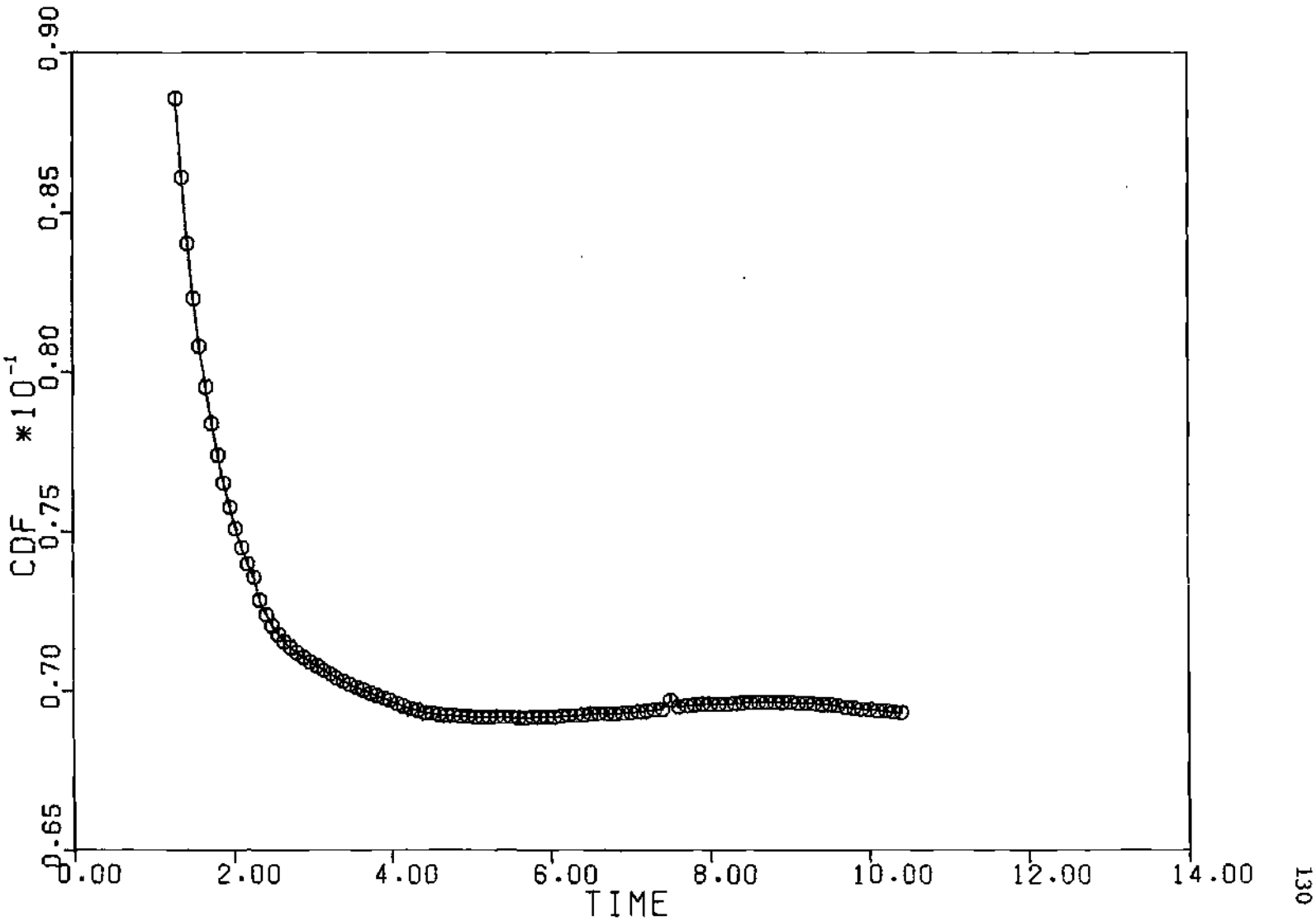

Figure 29. Joukowski 12% Airfoil ($\alpha = 3^{\circ} + 1^{\circ} \sin .6t$)--Viscous Drag History

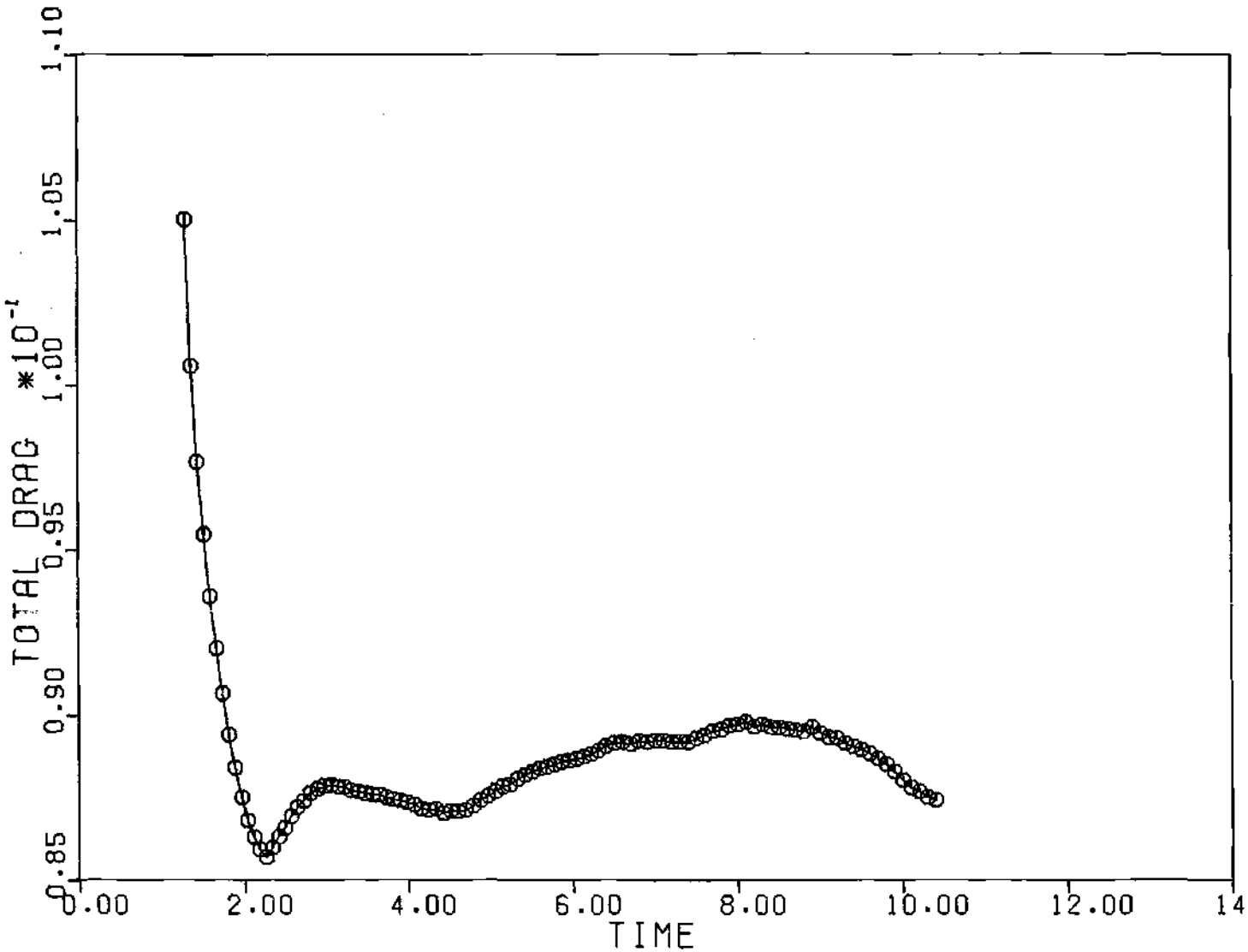

Figure 30. Joukowski 12% Airfoil ($\alpha = 3^{o} + 1^{o}$ sin .6t)--Total Drag History

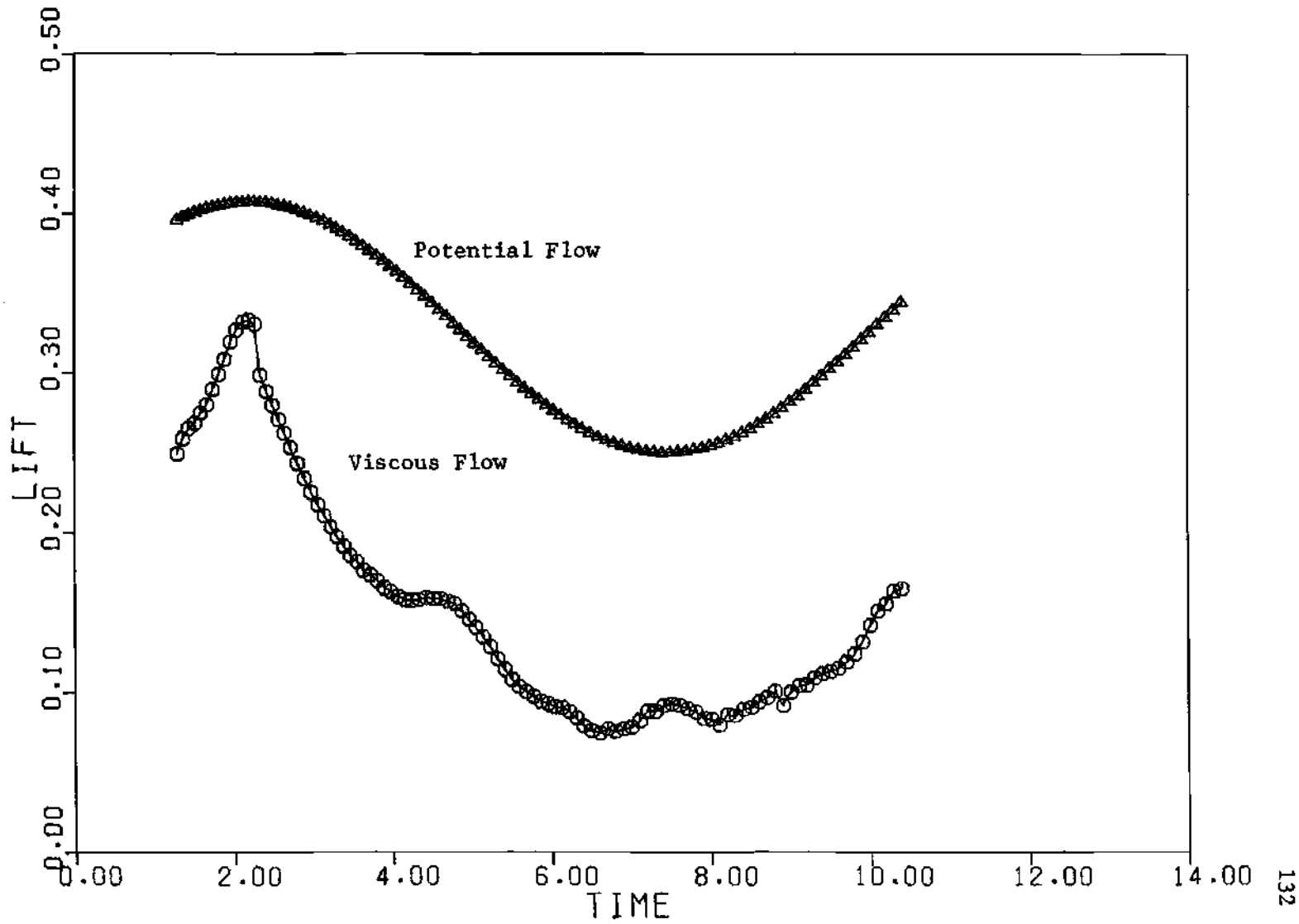

Figure 31. Joukowski 12% Airfoil ($\alpha = 3^{\circ} + 1^{\circ} \sin 6t$)--Lift History

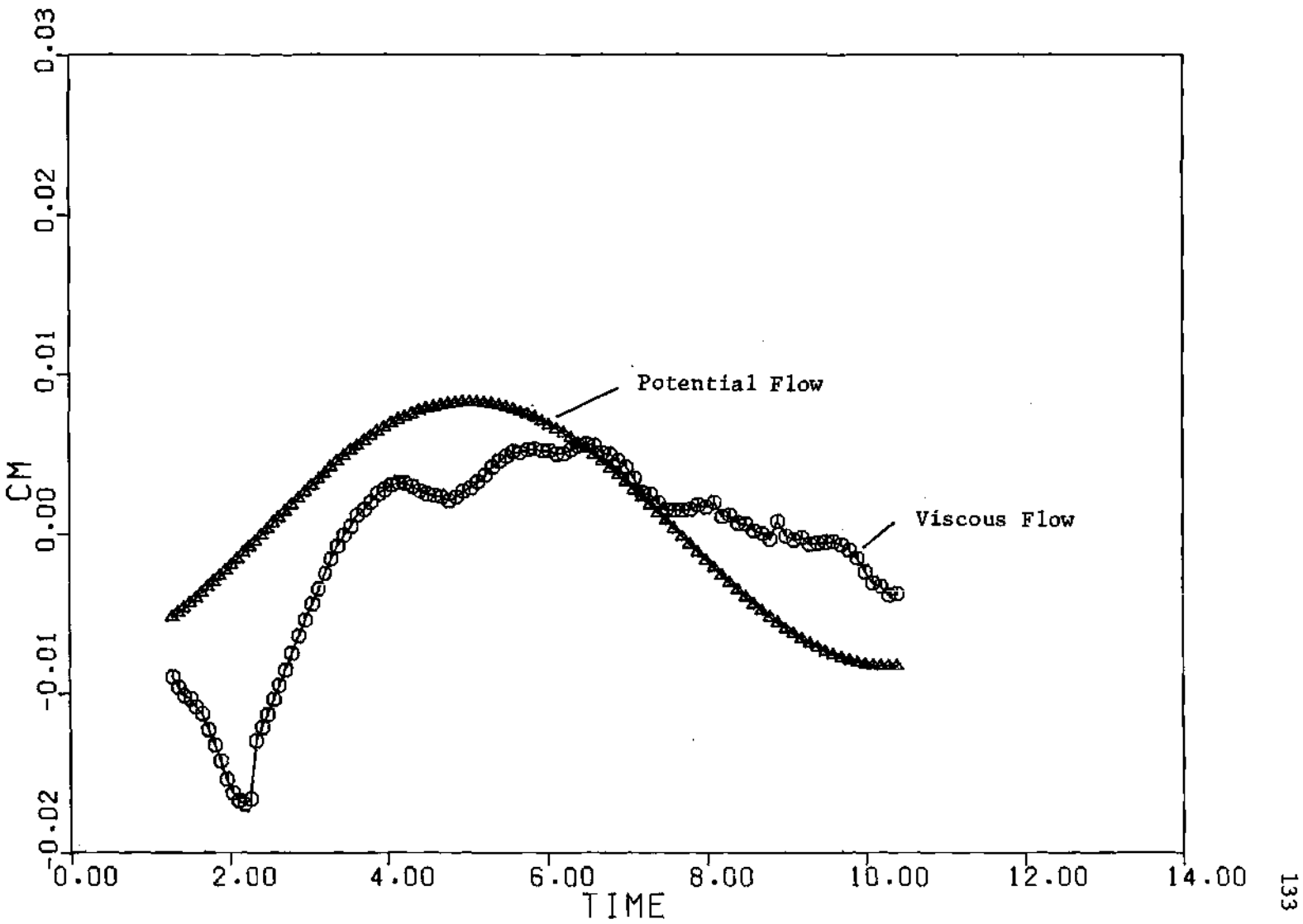

Figure 32. Joukowski 12% Airfoil ($\alpha = 3^{o} + 1^{o} \sin .6t$)--Moment History

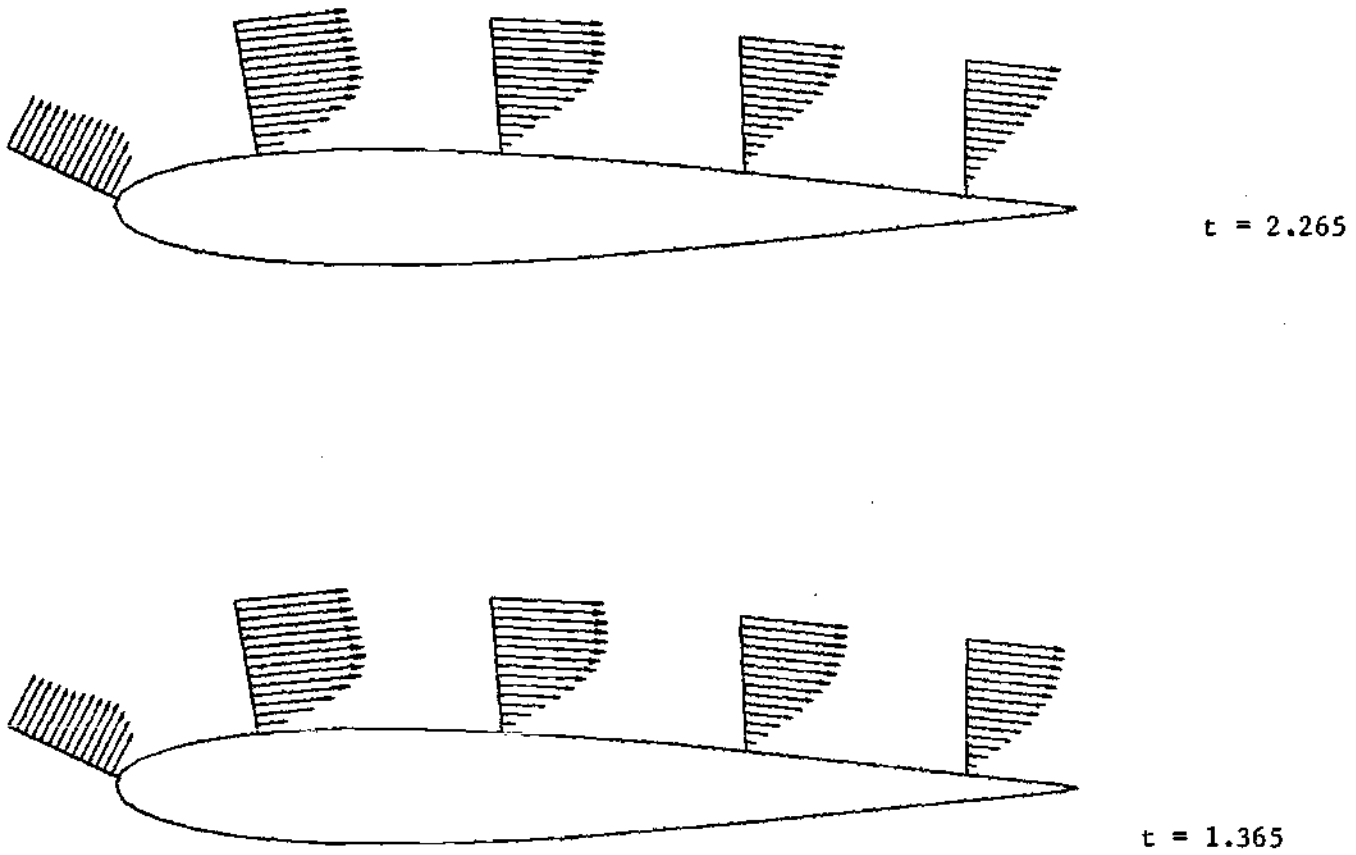

Figure 33. Joukowski 12'/. Airfoil ($\alpha = 3^{o} + 1^{o} \sin .6t$)--Velocity Profiles at t=1.365 and t=2.265 at Selected Locations on the Upper Surface

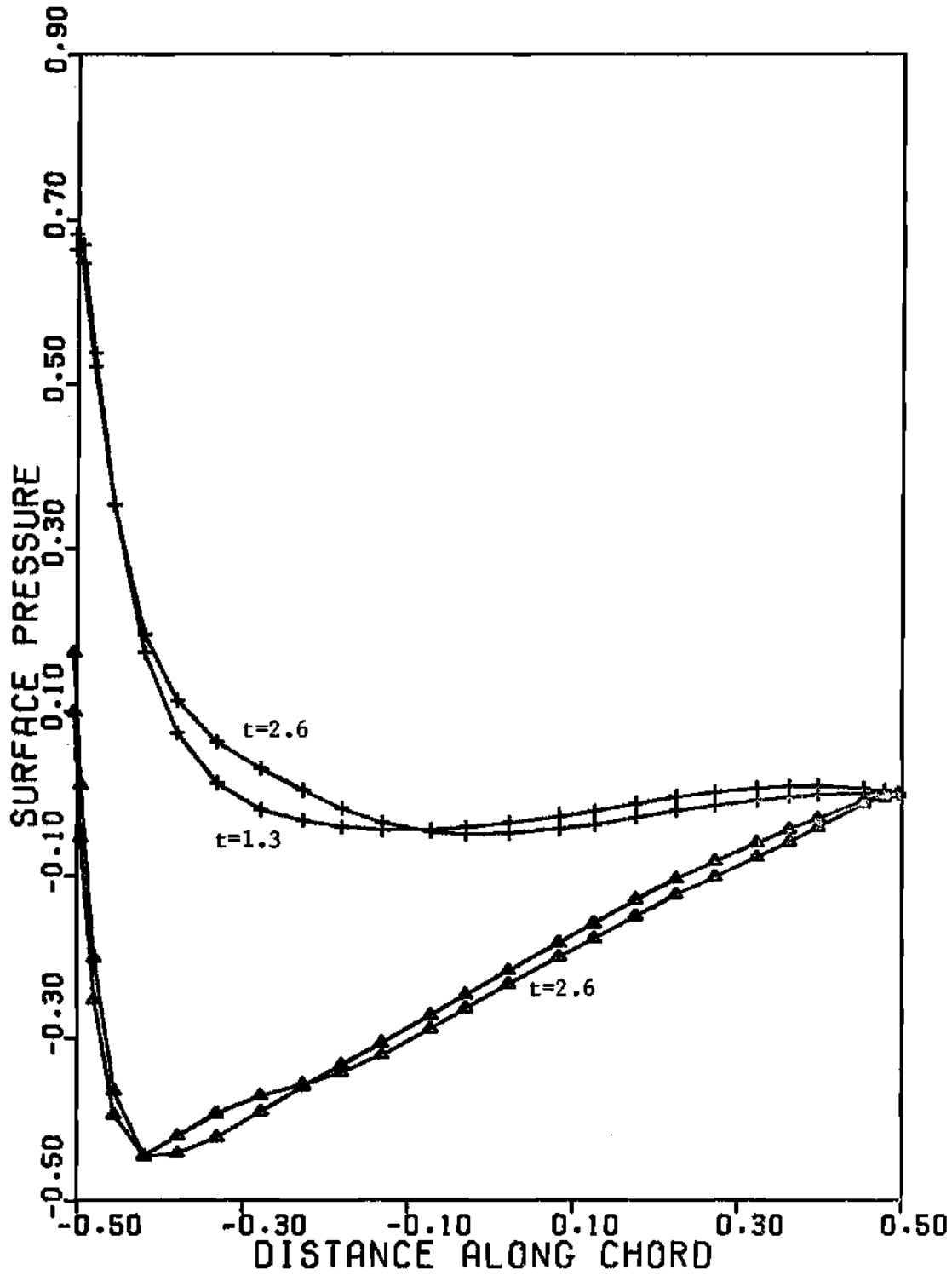

Figure 34. Joukowski 12%/. Airfoil ($\alpha = 3^{\circ} + 1^{\circ} \sin .6t$)--Surface Pressure Distribution at t=1.3 and t=2.6

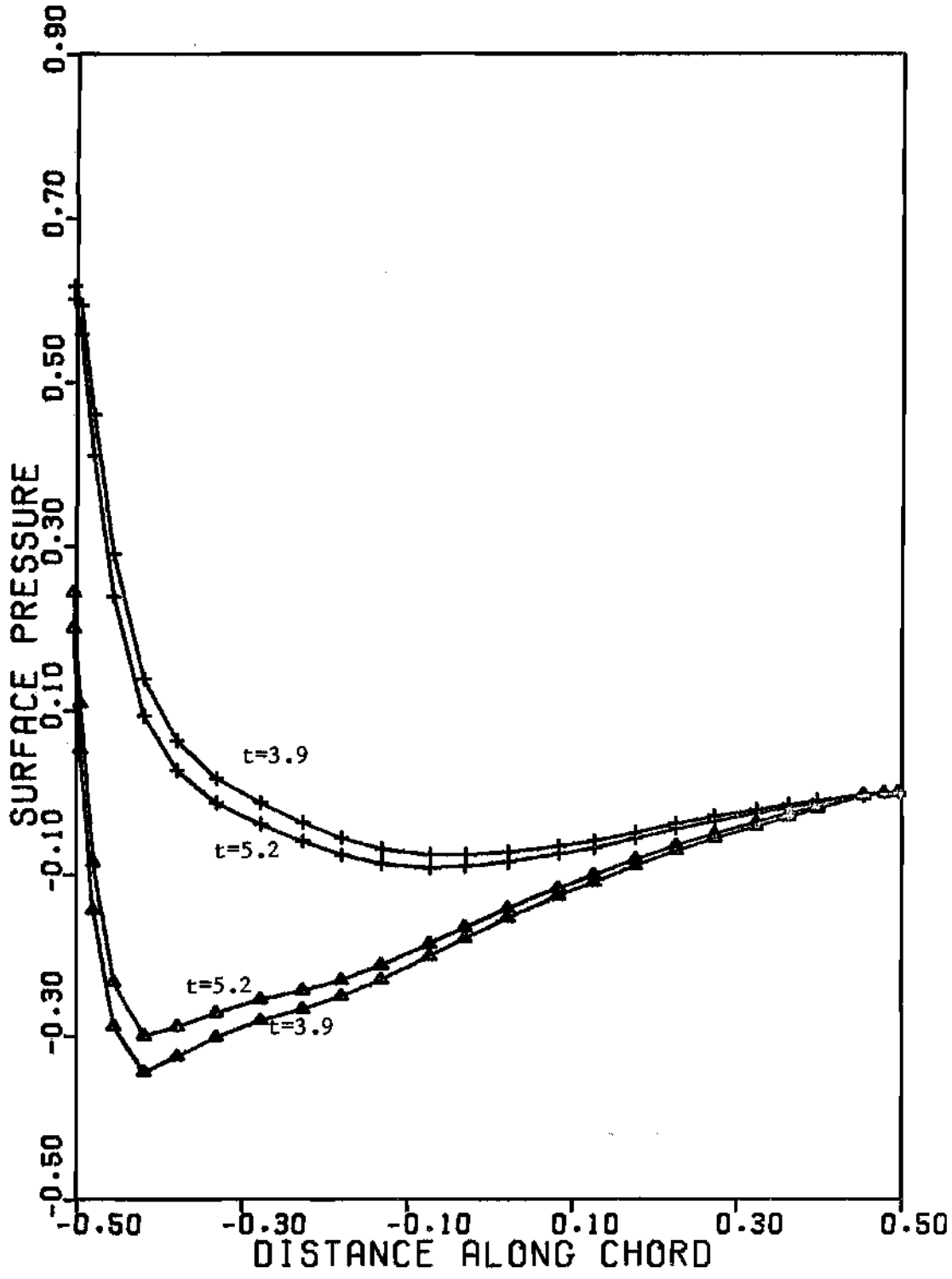

Figure 35. Joukowski 12%/. Airfoil ($\alpha = 3^{o} + 1^{o} \sin .6t$--Surface Pressure Distribution at t=3.9 and 5.2

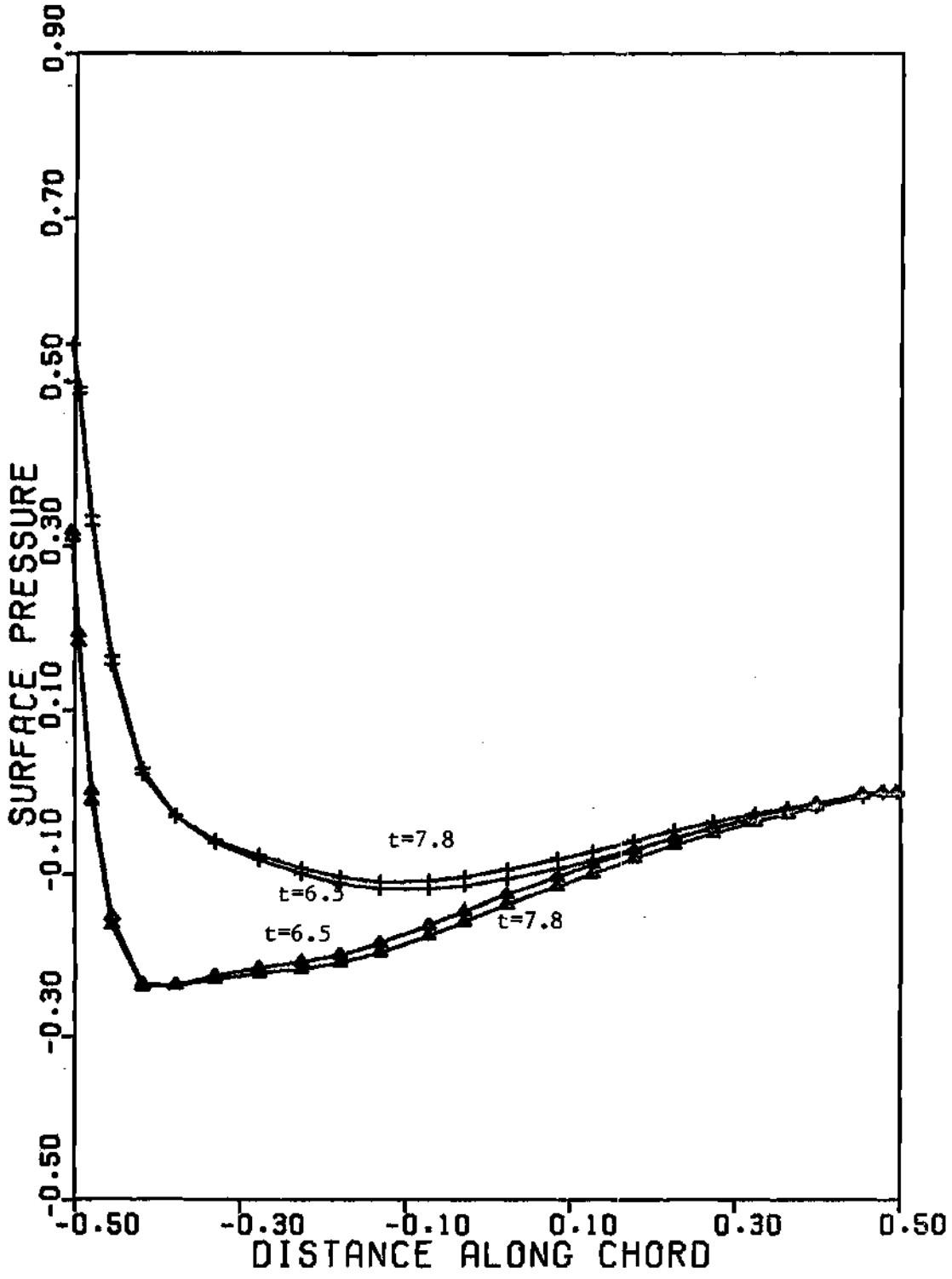

Figure 36. Joukowski 12% airfoil ($\alpha = 3^{\circ} + 1^{\circ} \sin 6t$)--Surface Pressure Distribution at t=6.5 and t=7.8

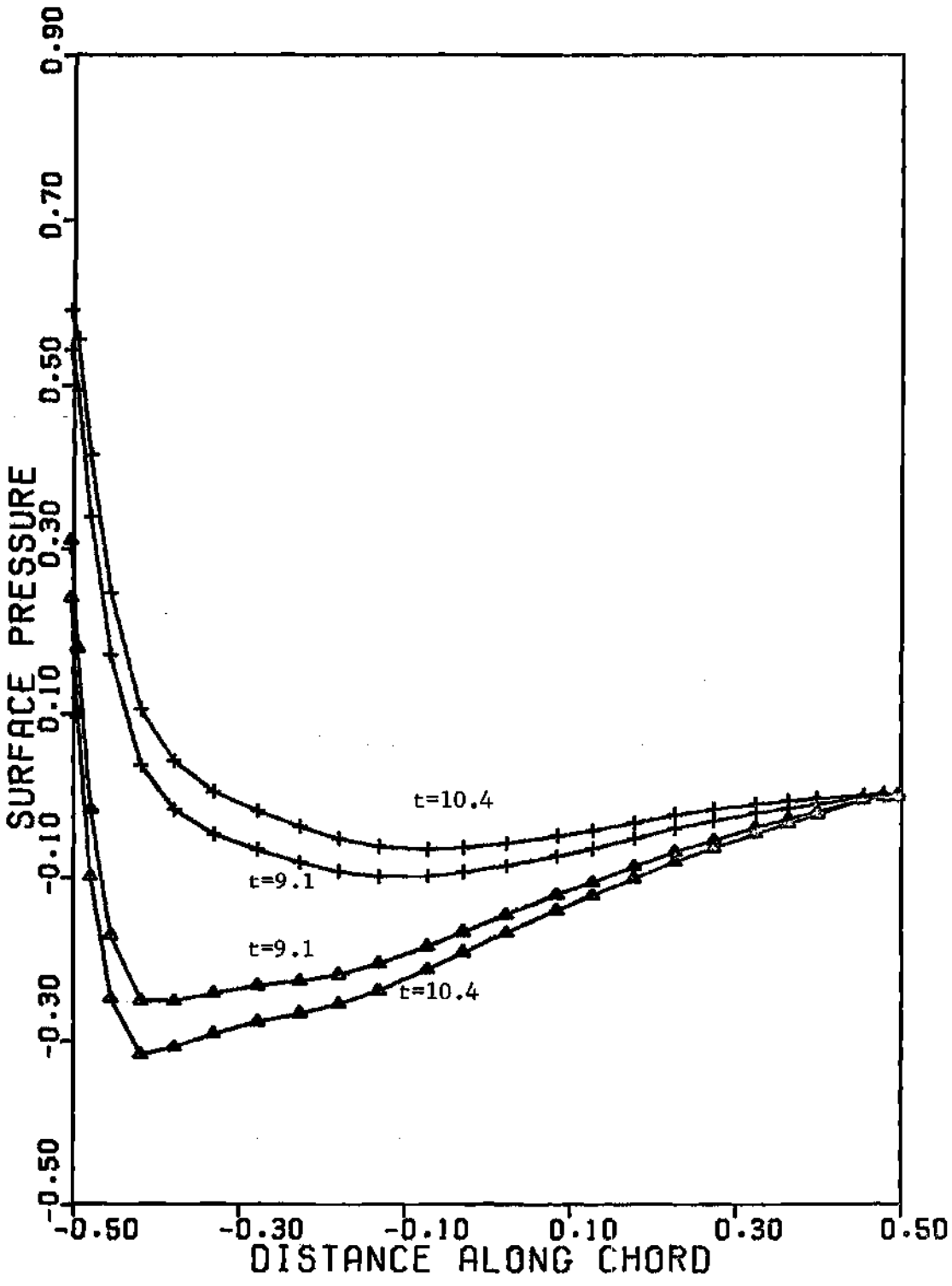

Figure 37. Joukowski 12% Airfoil ($\alpha = 3^{\circ} + 1^{\circ}$ sin.6t)--Surface Pressure Distribution at t=9.1 and t=10.4

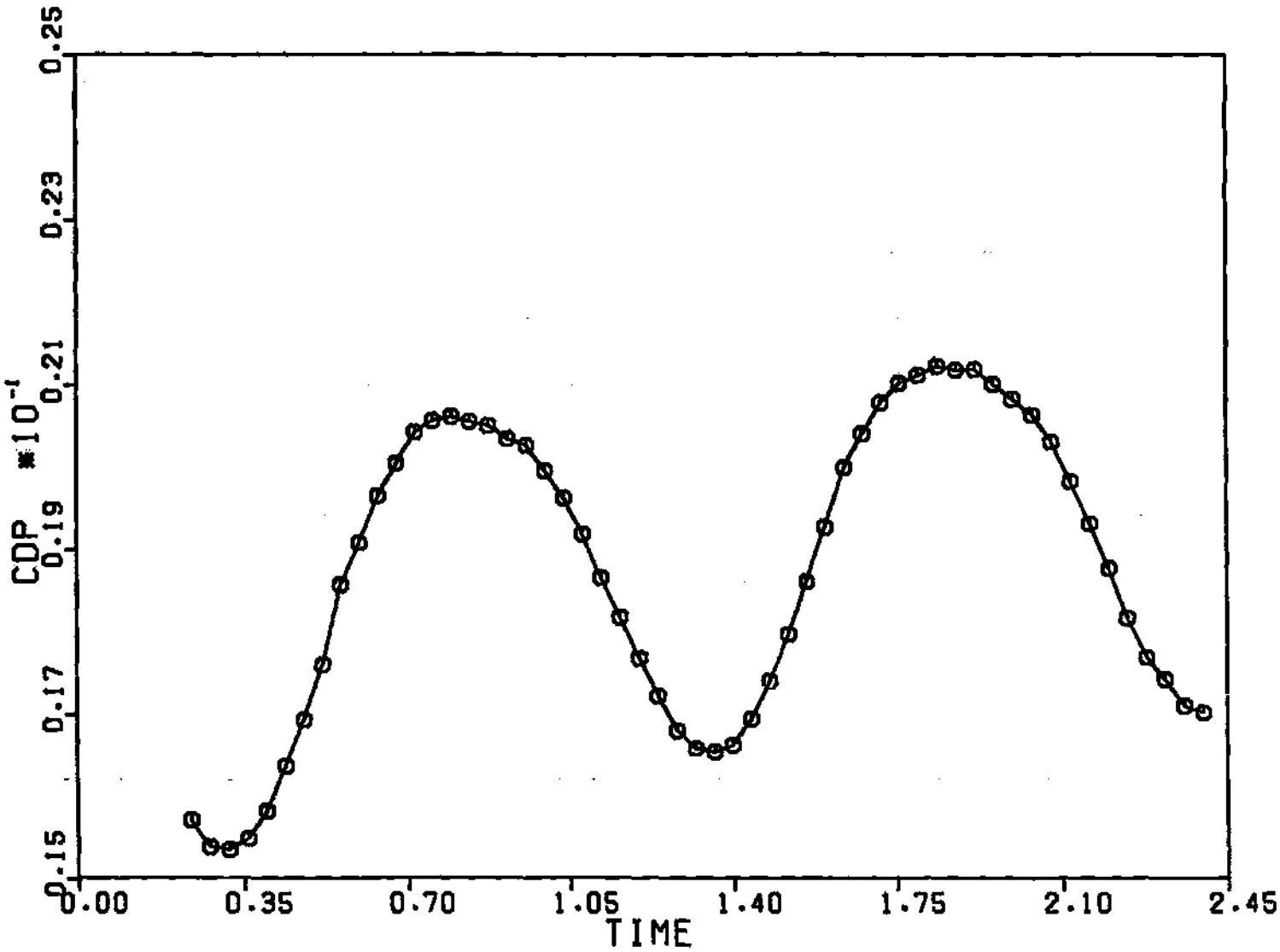

Figure 38. Joukowski 12% Airfoil ($\alpha = 3^{\circ} + 1^{\circ} \sin 6t$)--Pressure Drag History

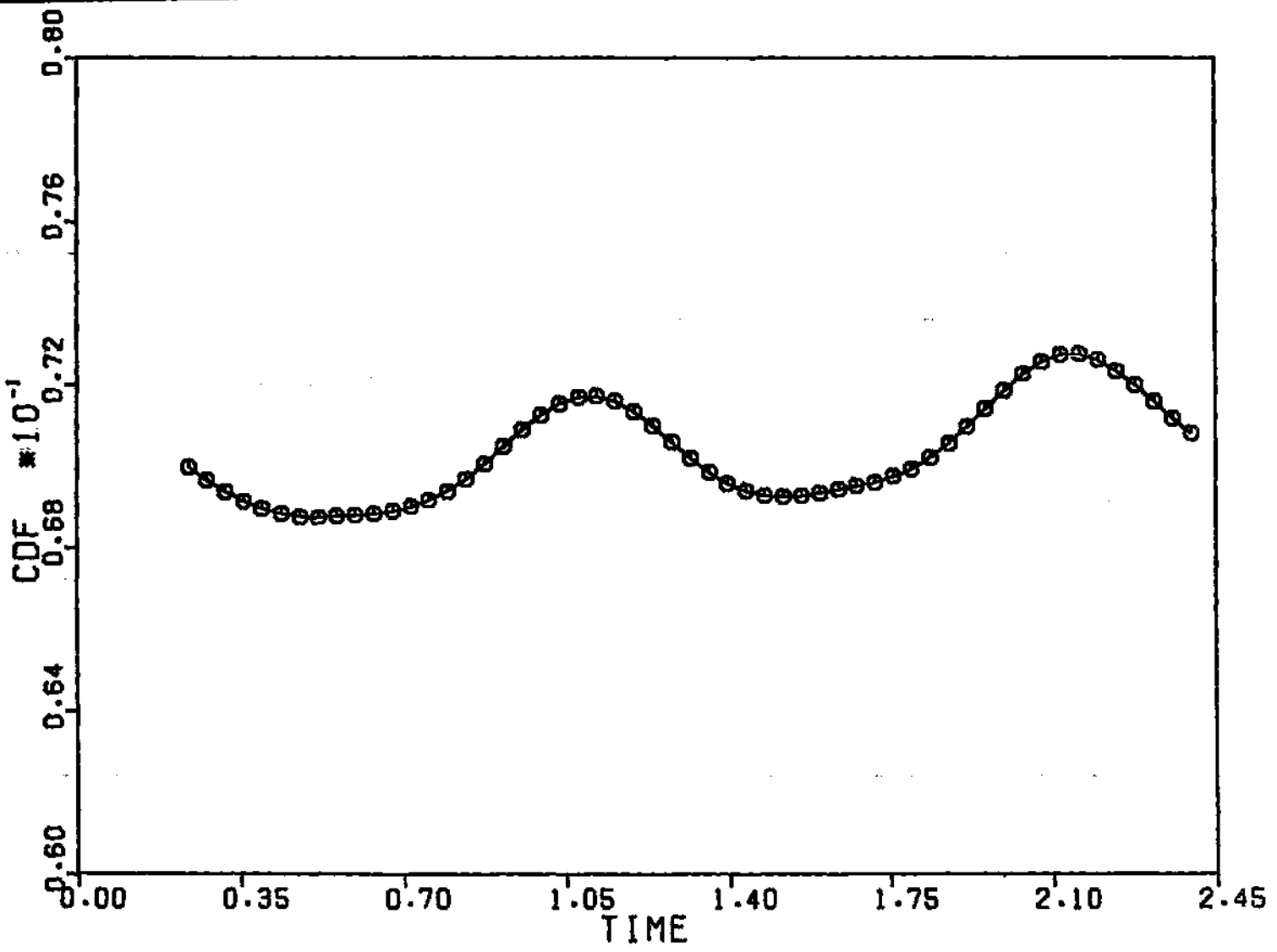

Figure 39. Joukowski 12% Airfoil ($\alpha = 3^{\circ} + 1^{\circ} \sin 6t$)--Viscous Drag History

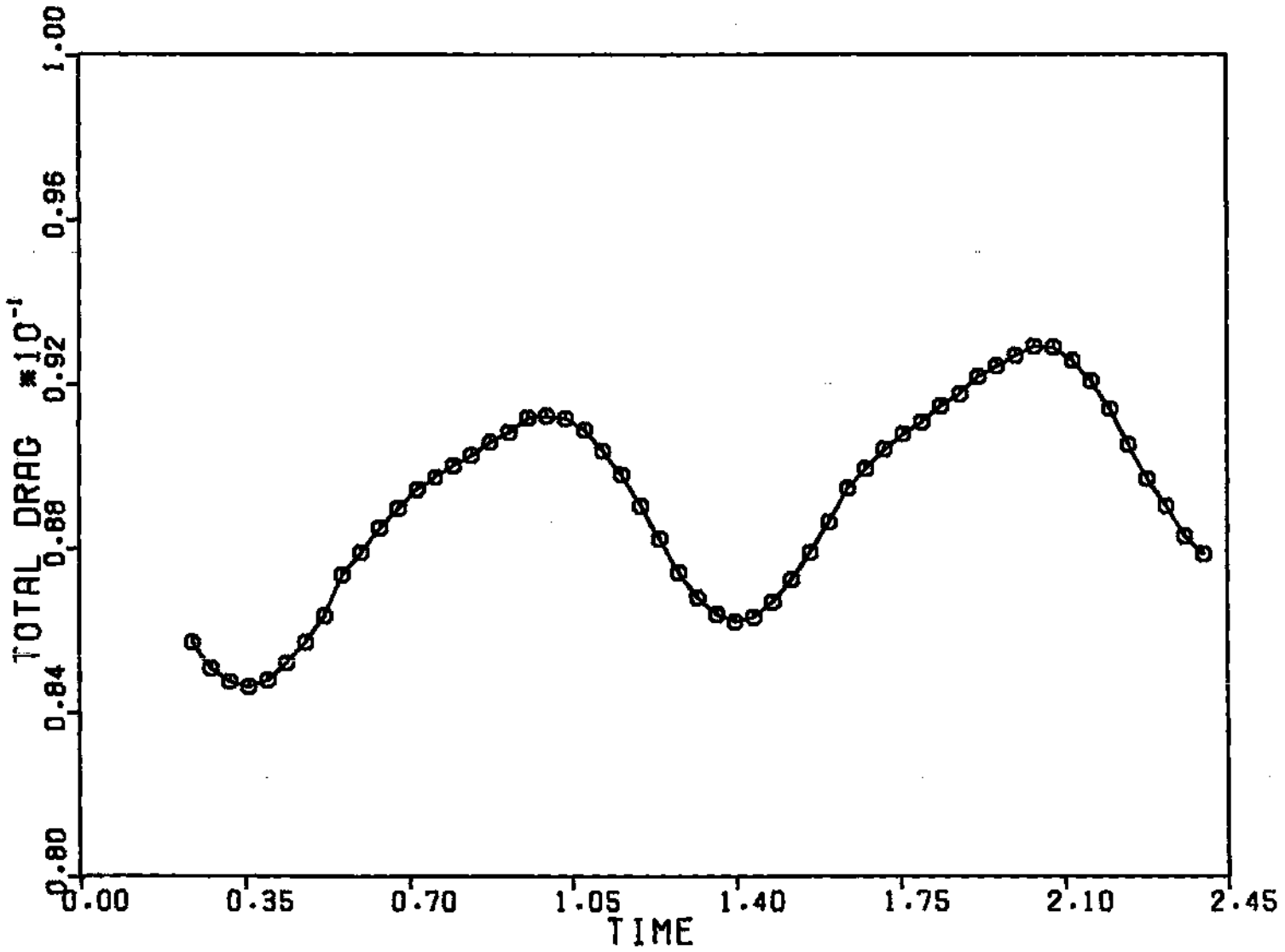

Figure 40. Joukowski 12% Airfoil ($\alpha = 3^{\circ} + 1^{\circ} \sin 6t$)--Total Drag History

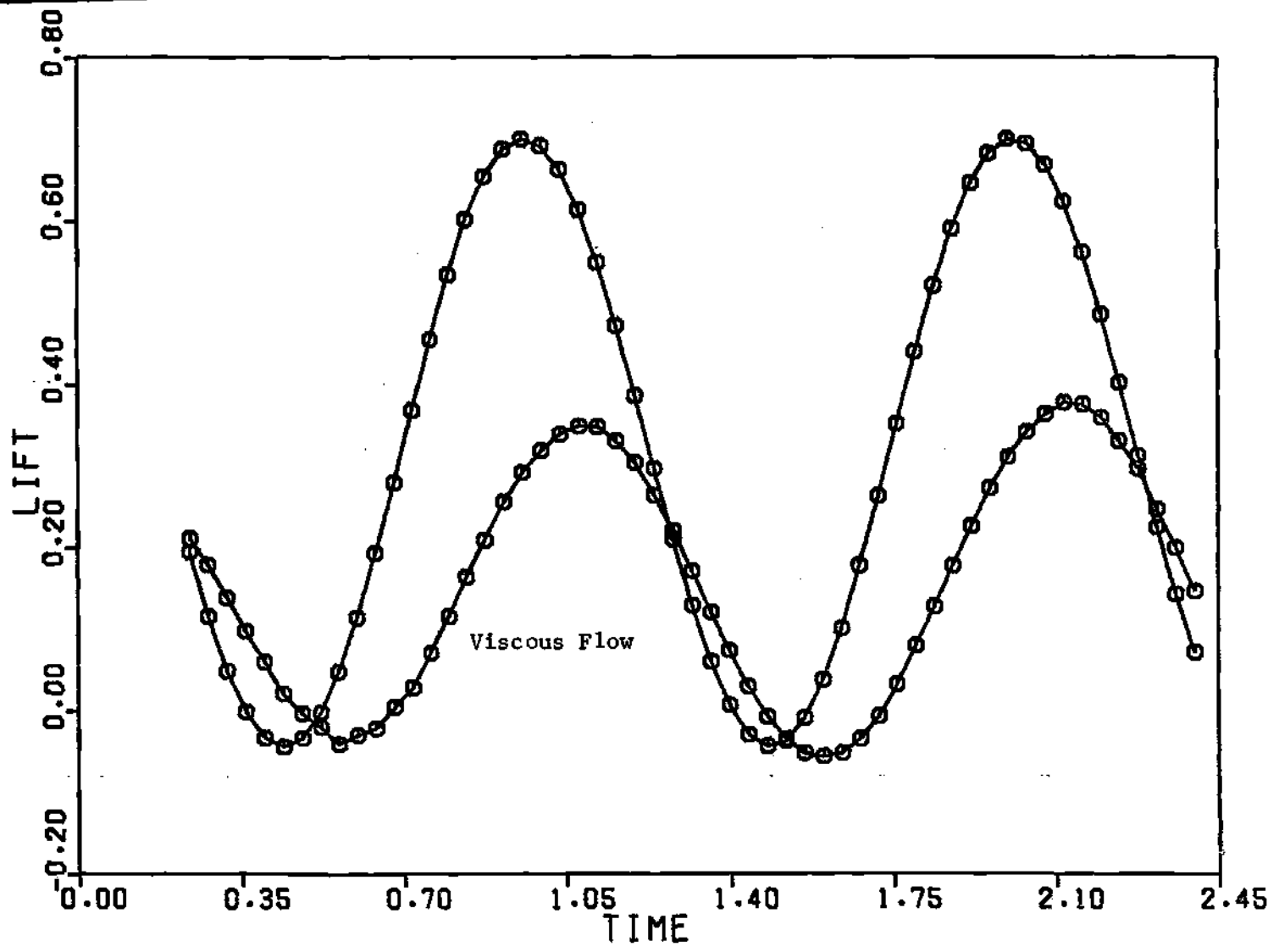

Figure 41. Joukowski 12% Airfoil ($\alpha = 3^{o} + 1^{o} \sin 6t$)--Lift History

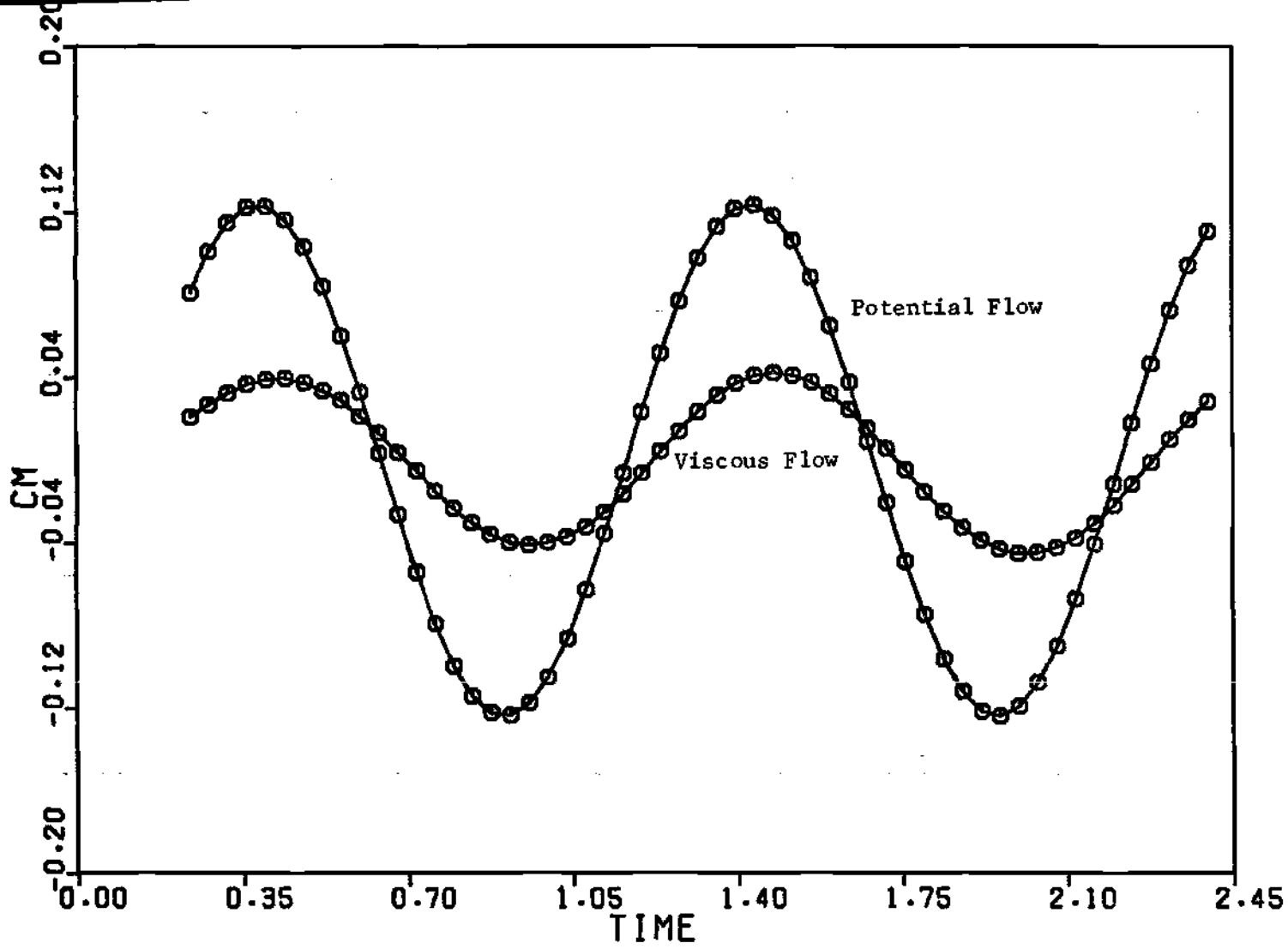

Figure 42. Joukowski 12% Airfoil ($\alpha = 3^{\circ} + 1^{\circ} \sin 6t$)--Moment History

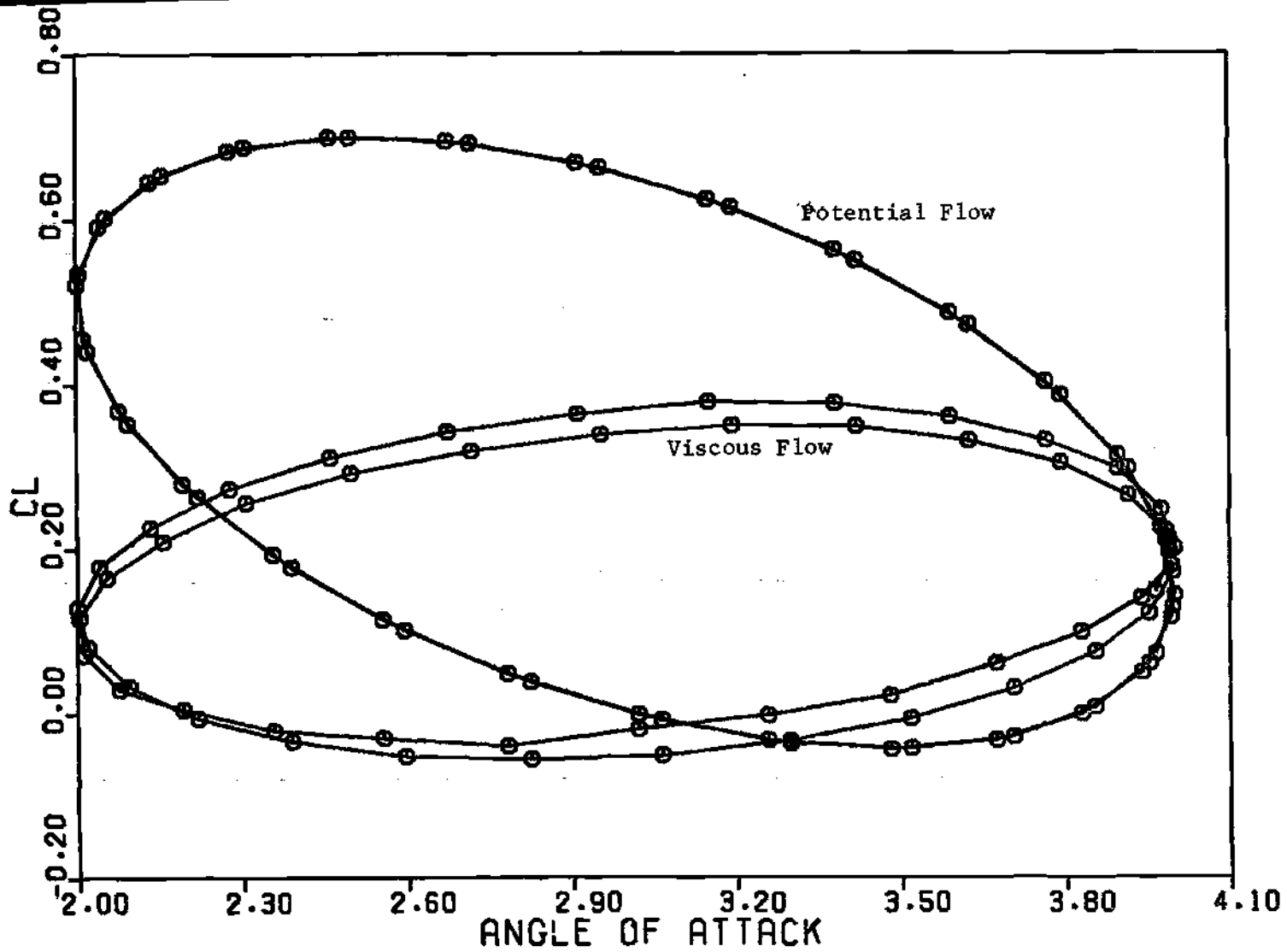

Figure 43. Joukowski 12% Airfoil ($\alpha = 3^{\circ} + 1^{\circ} \sin 6t$)--Lift Hystersis

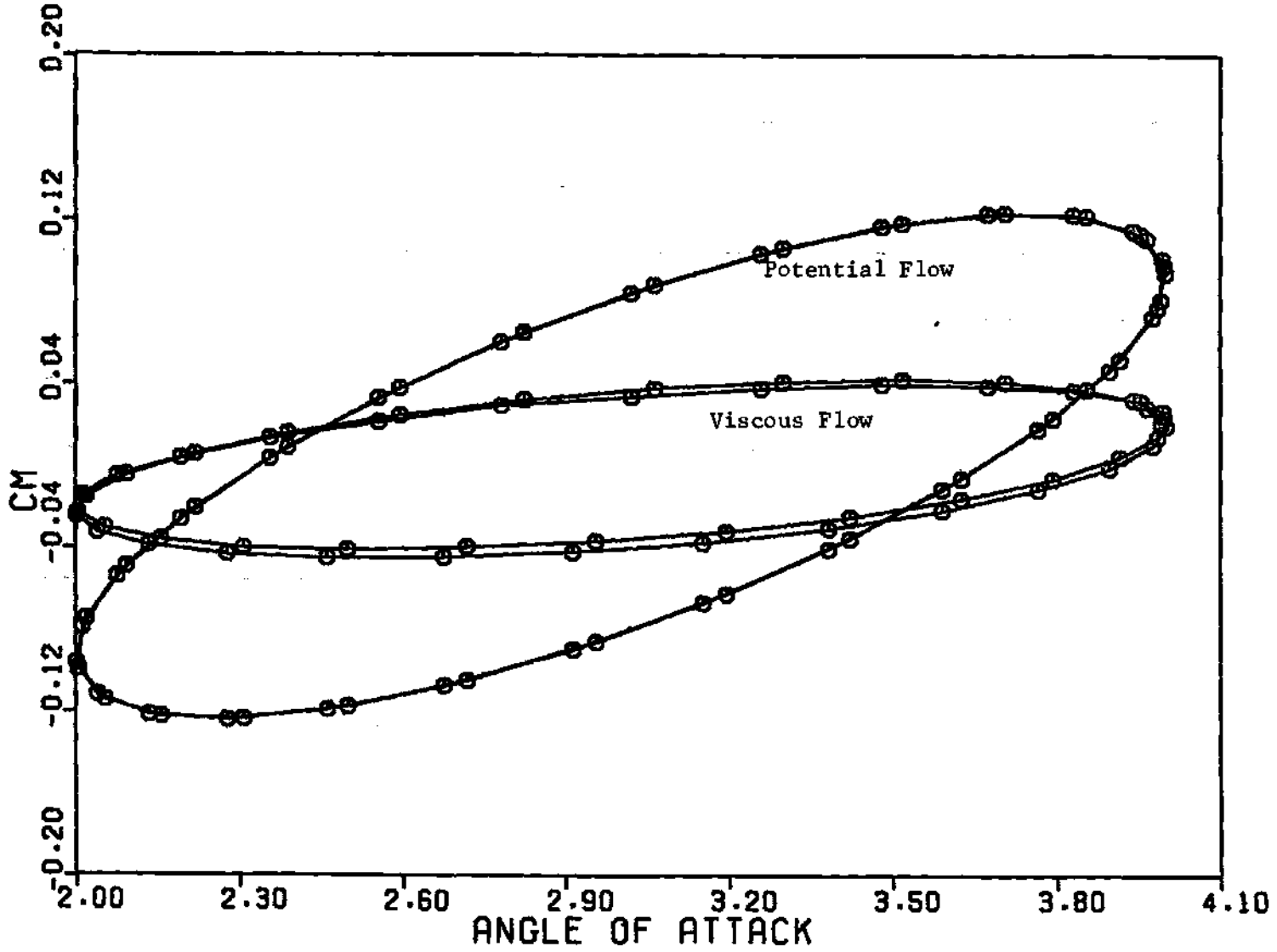

Figure 44. Joukowski 12% Airfoil ($\alpha = 3^{o} + 1^{o} \sin 6t$)--Moment Hysteresis

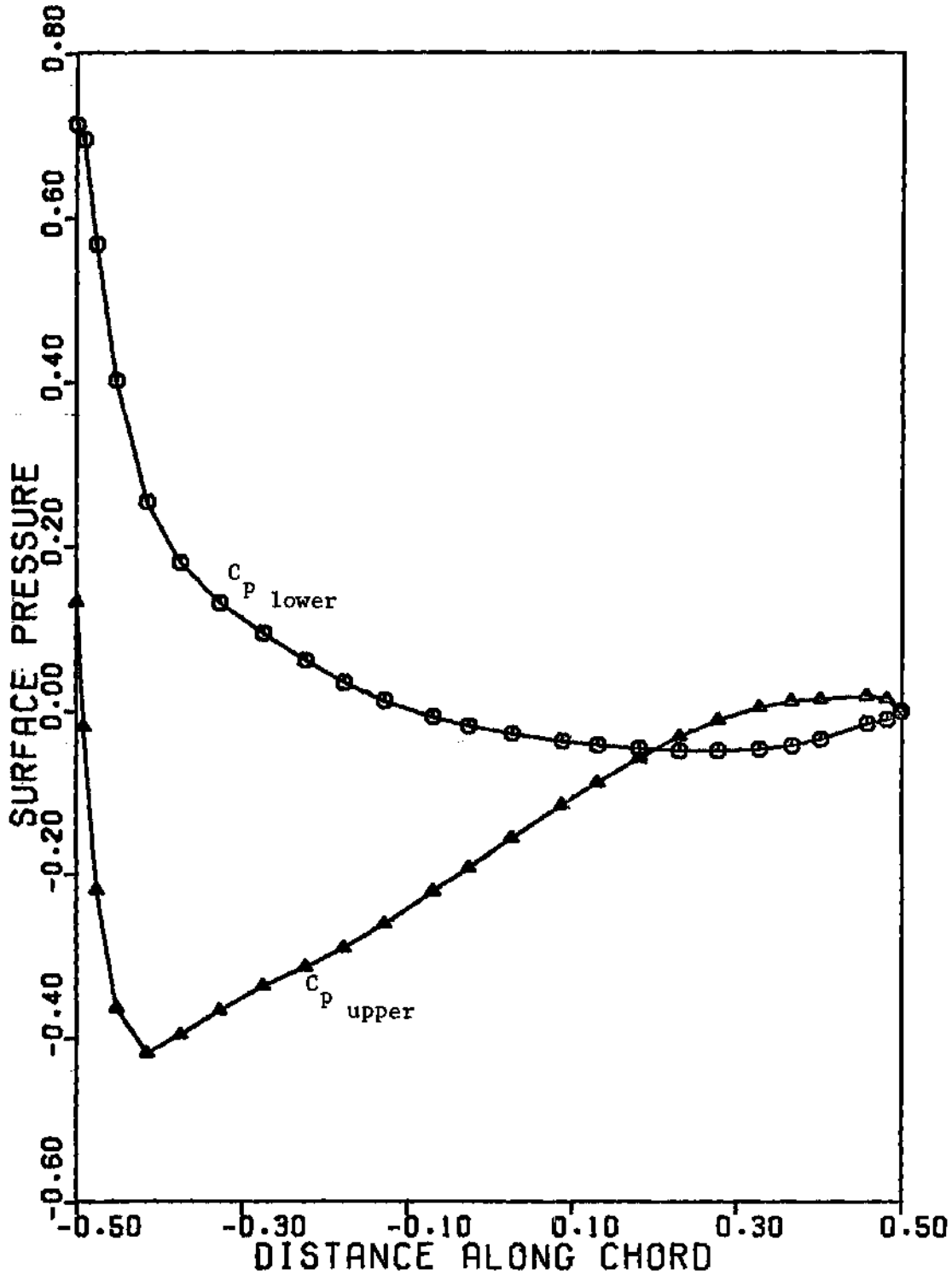

Figure 45. Joukowski 12% Airfoil ($\alpha = 3^{o} + 1^{o} \sin 6t$)--Surface Pressure Distribution at $t = 1.28$

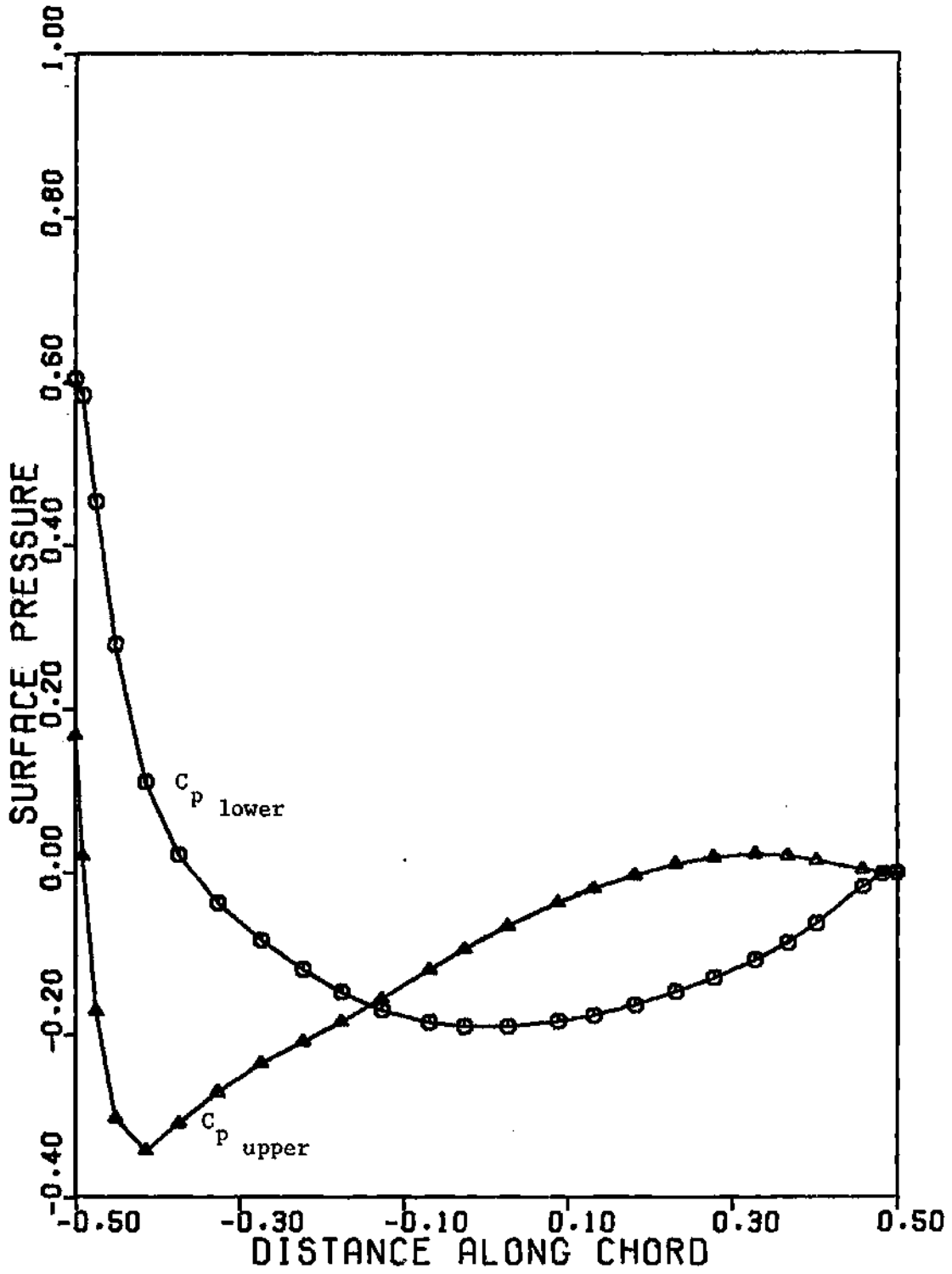

Figure 46. Joukowski 12% Airfoil ($\alpha = 3^{\circ} + 1^{\circ} \sin 6t$)--Surface Pressure Distribution at t = 1.64

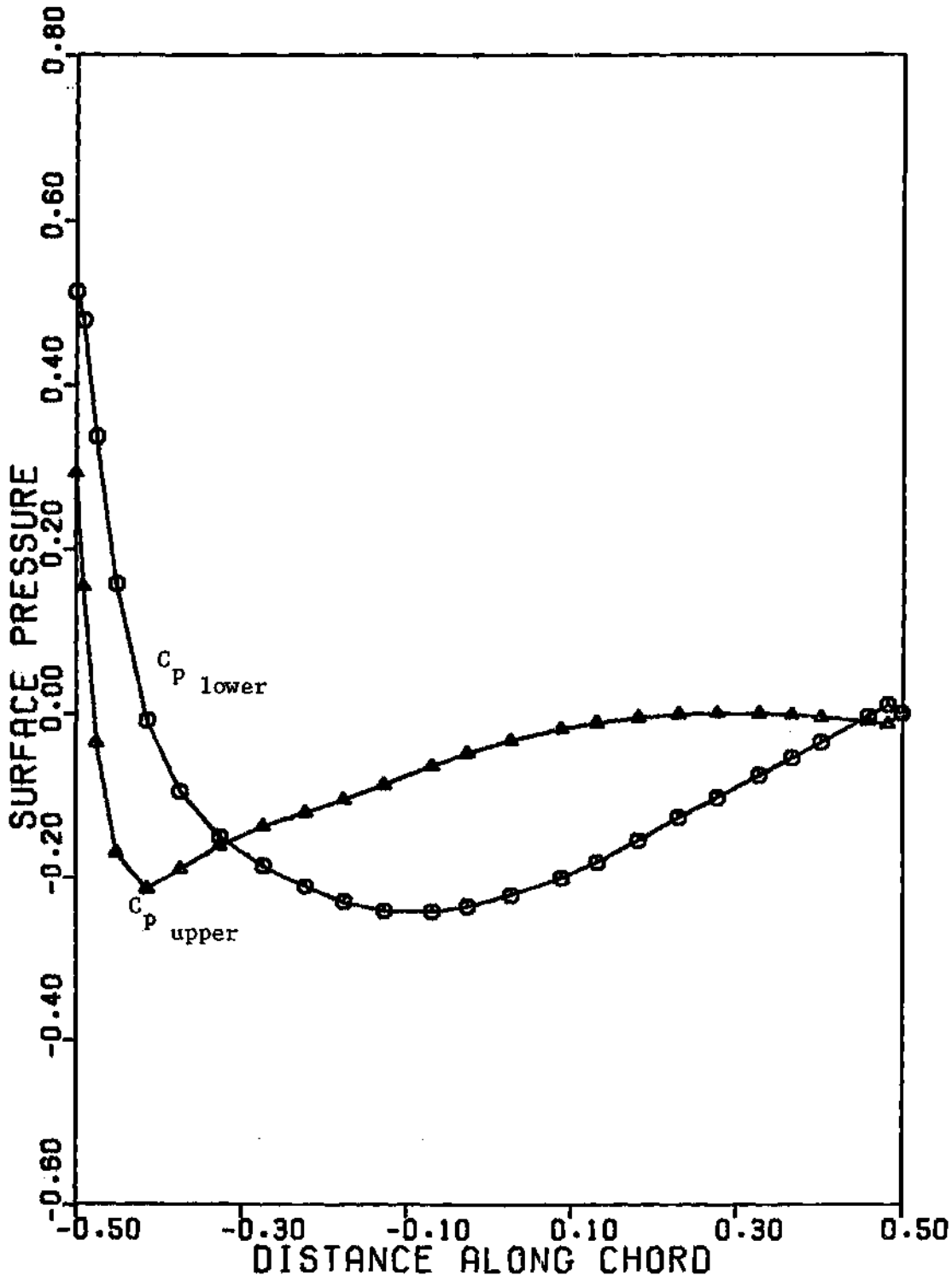

Figure 47. Joukowski 12% Airfoil ($\alpha = 3^{\circ} + 1^{\circ} \sin 6t$)--Surface Pressure Distribution at t = 1.6

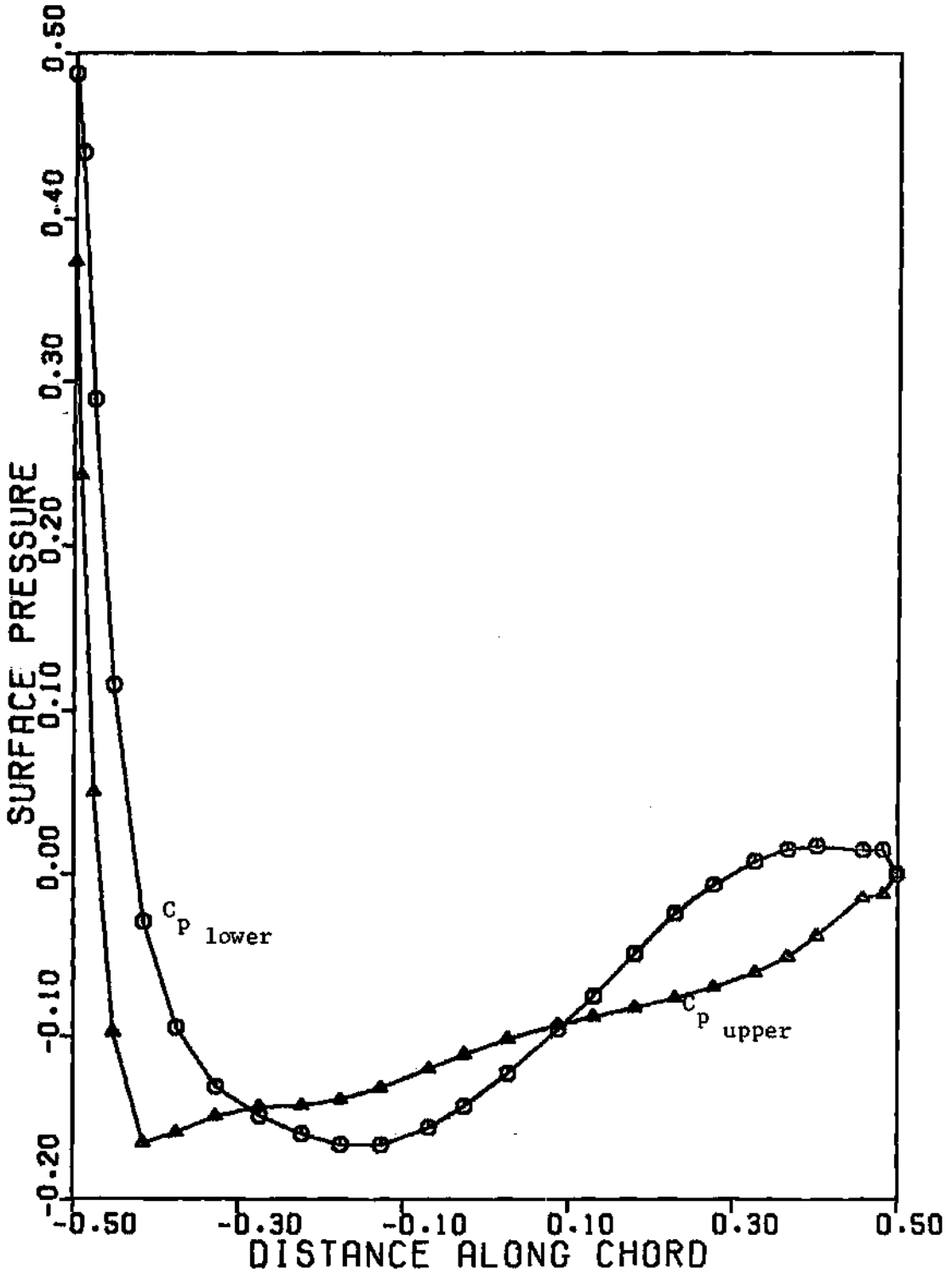

Figure 48. Joukowski 12% Airfoil ($\alpha = 3^\circ + 1^\circ \sin 6t$)--Surface Pressure Distribution at t = 1.76

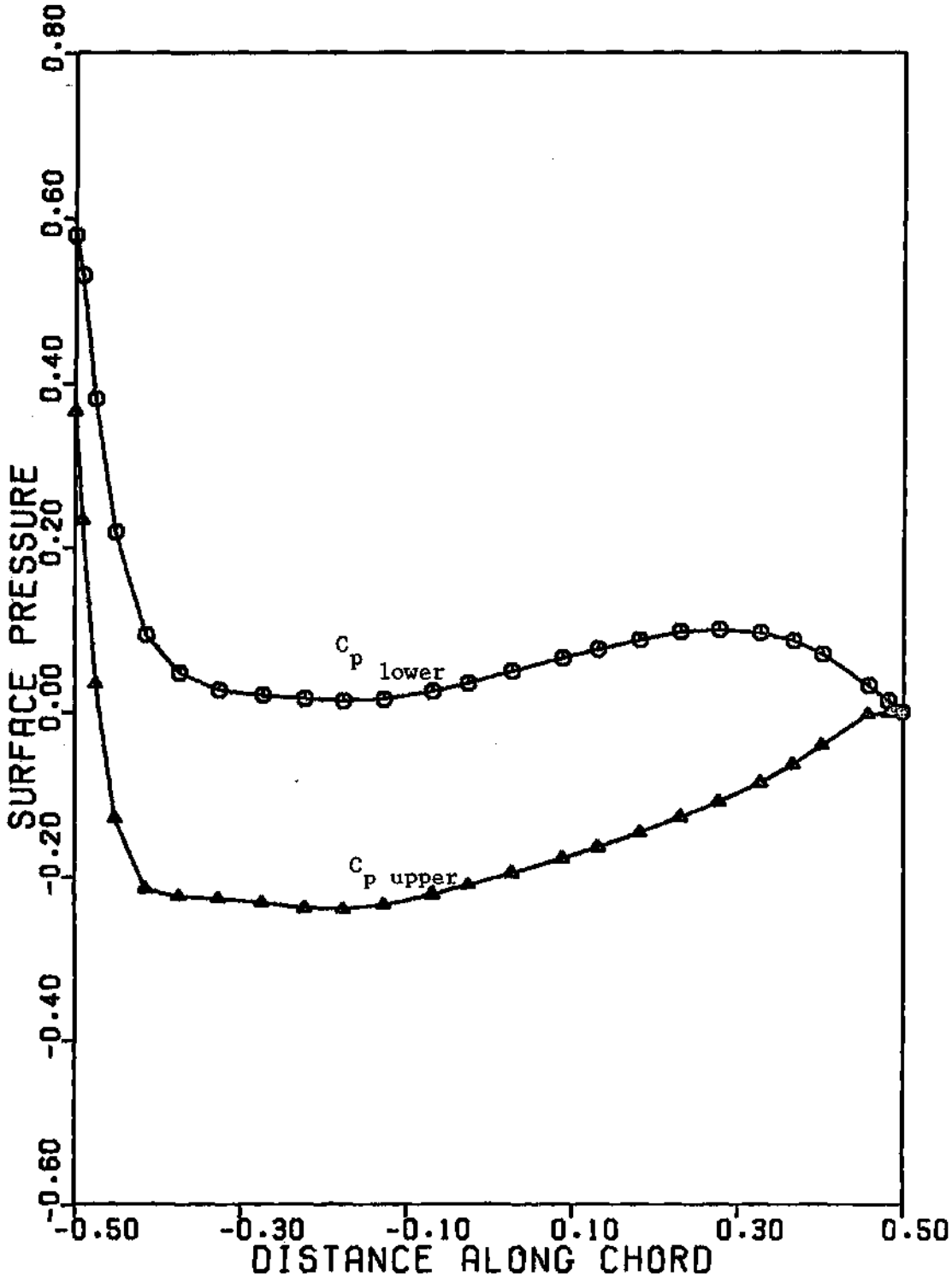

Figure 49. Joukowski 12% Airfoil ($\alpha = 3^{o} + 1^{o} \sin 6t$)--Surface Pressure Distribution at t = 1.92

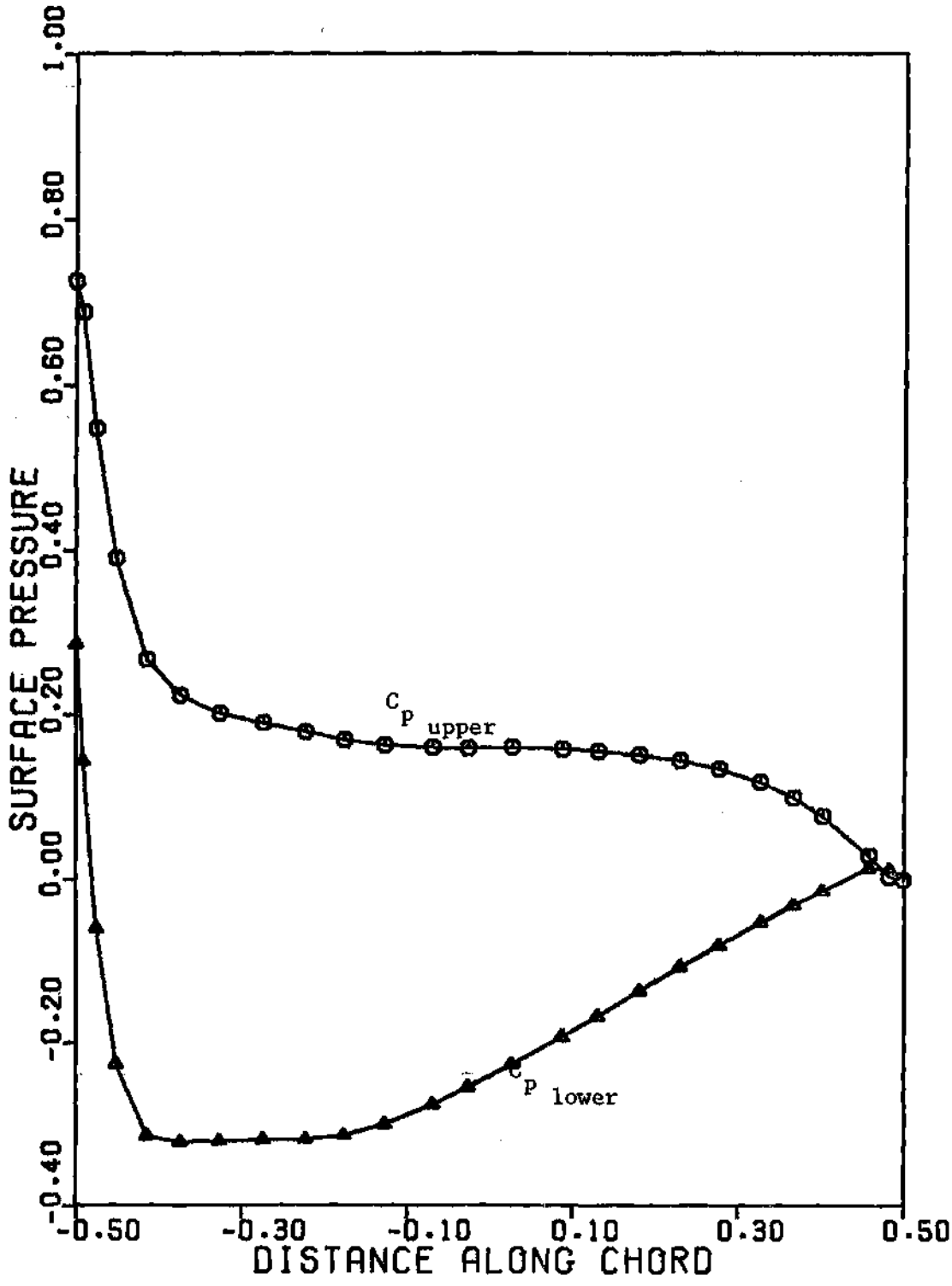

Figure 50. Joukowski 12% Airfoil ($\alpha = 3^{o} + 1^{o} \sin 6t$)--Surface Pressure Distribution at t = 2.08

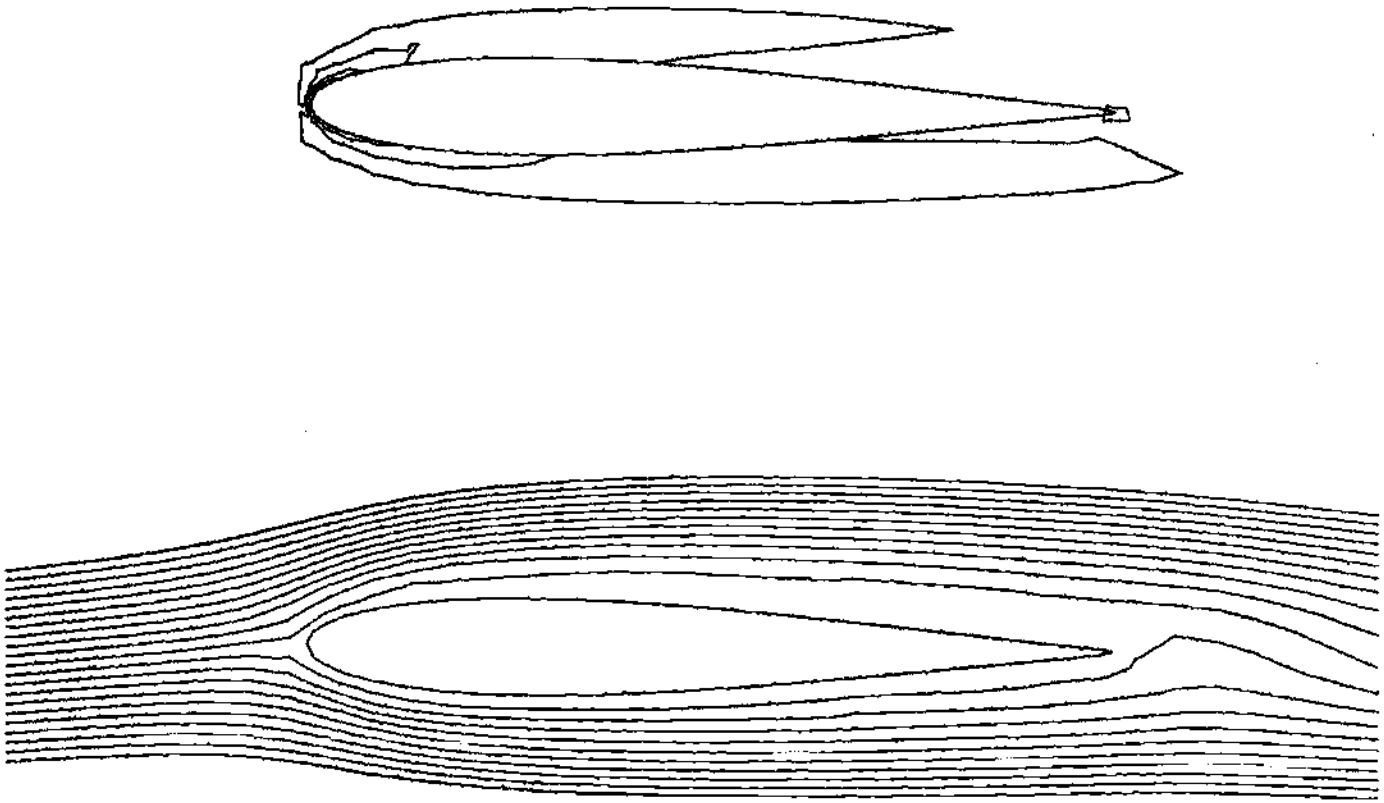

Figure 51. Joukowski 12% Airfoil ($\alpha = 3^{\circ} + 1^{\circ} \sin 6t$)--Streamlines and Constant Vorticity Contours at $t = 0.68$

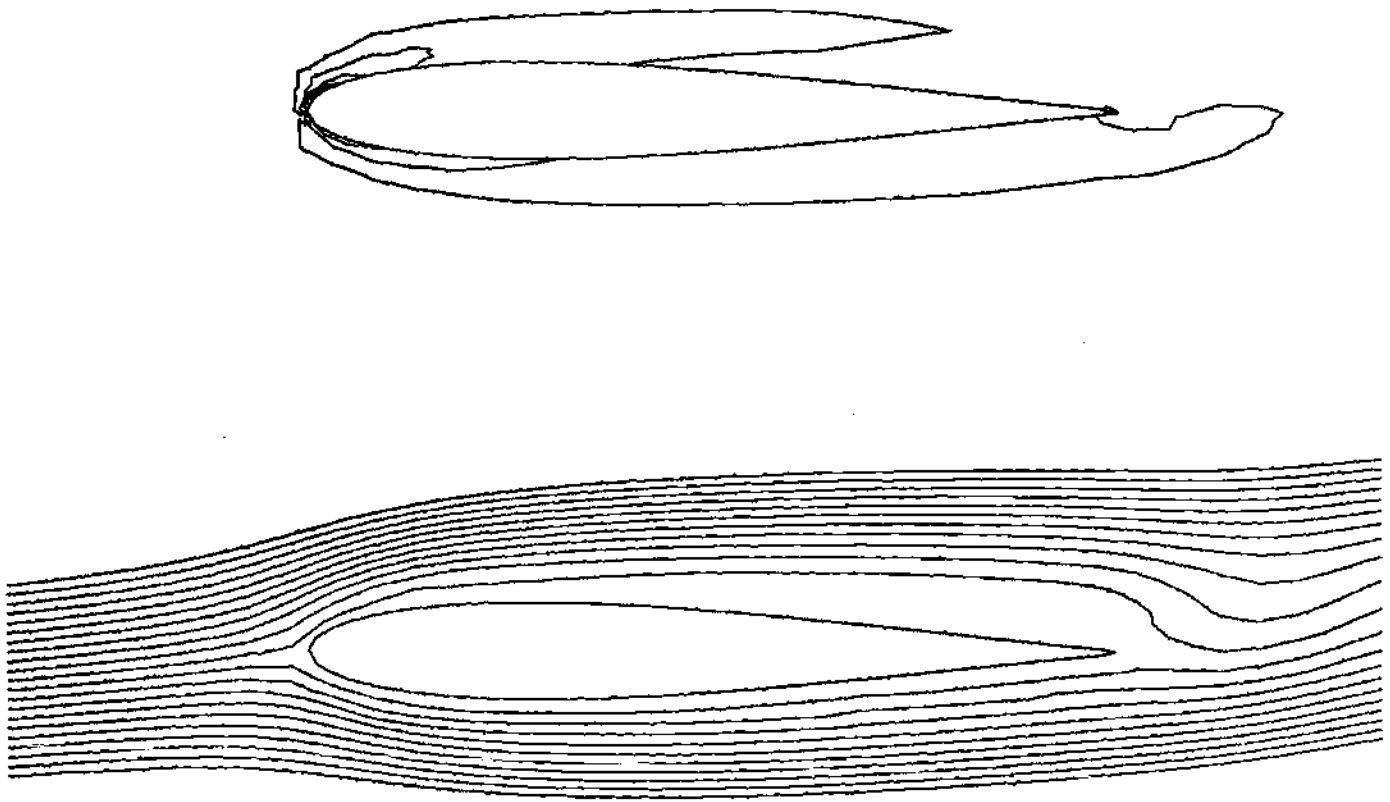

Figure 52. Joukowski 12% Airfoil ($\alpha = 3^{\circ} + 1^{\circ} \sin 6t$)--Streamlines and Constant Vorticity Contours at t = 1.28

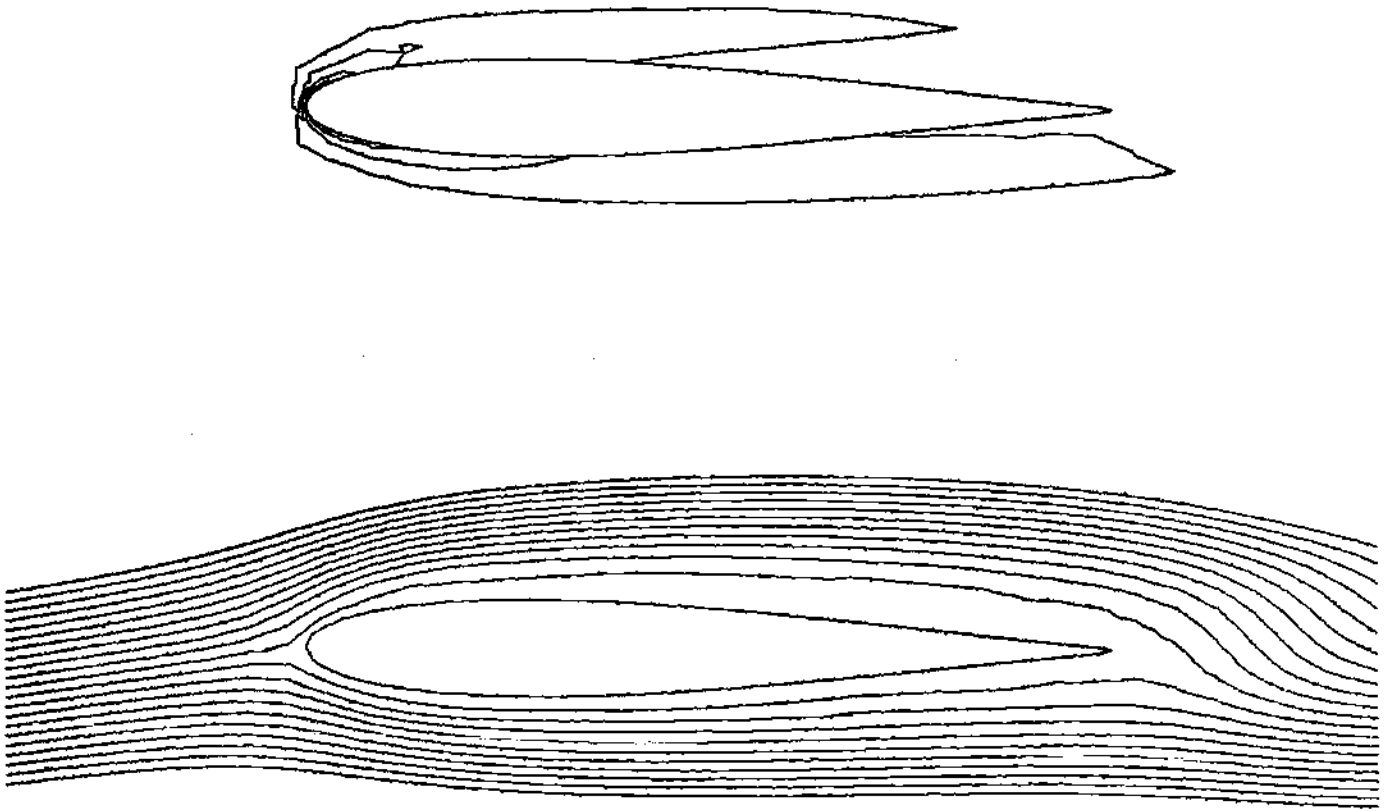

Figure 53. Joukowski 12% Airfoil ($\alpha = 3^{o} + 1^{o} \sin 6t$)--Streamlines and Constant Vorticity Contours at t = 1.56

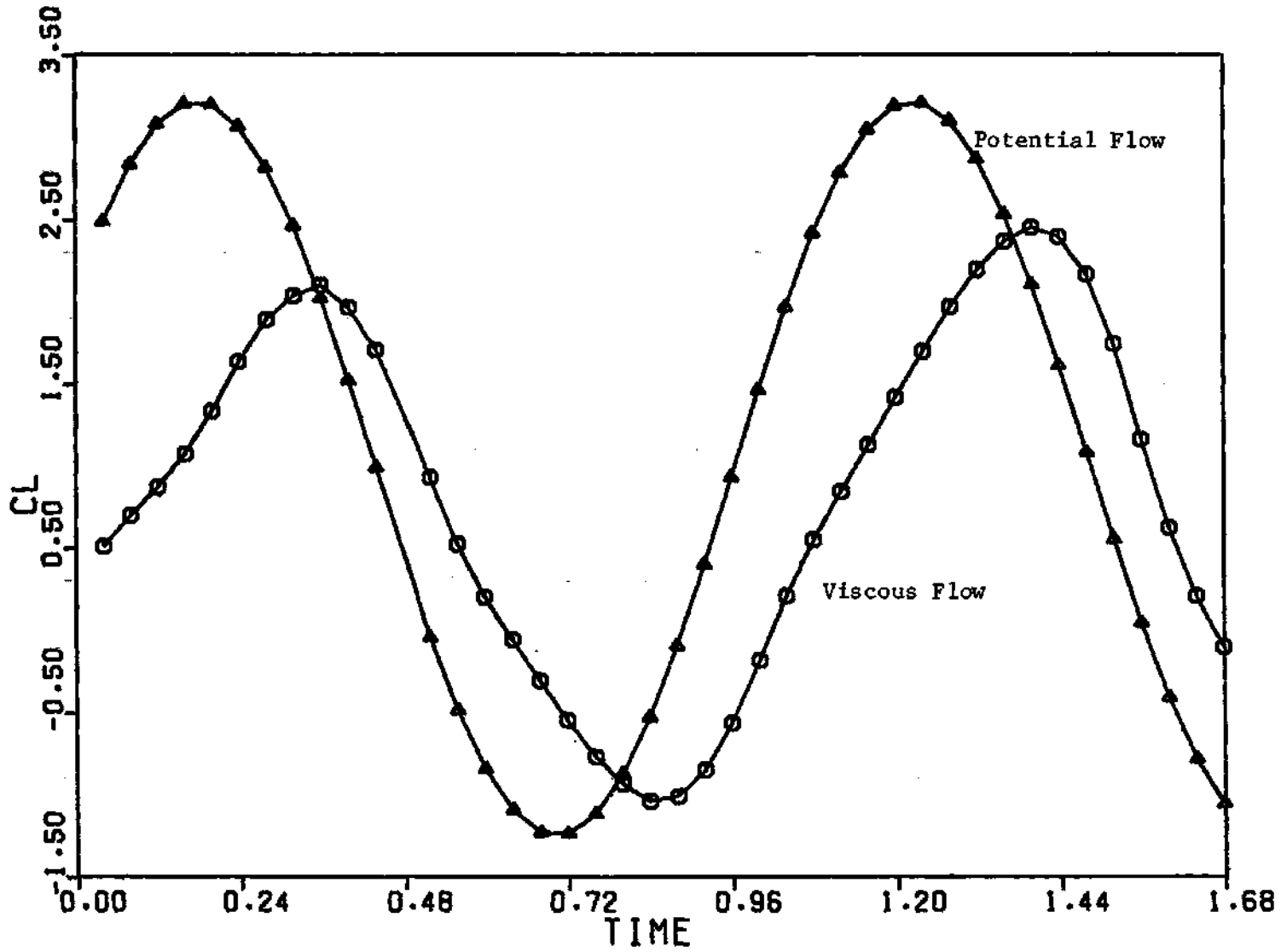

Figure 54. Joukowski 12% Airfoil ($\alpha = 9^{o} - 6^{o} \cos 6t$)--Lift History

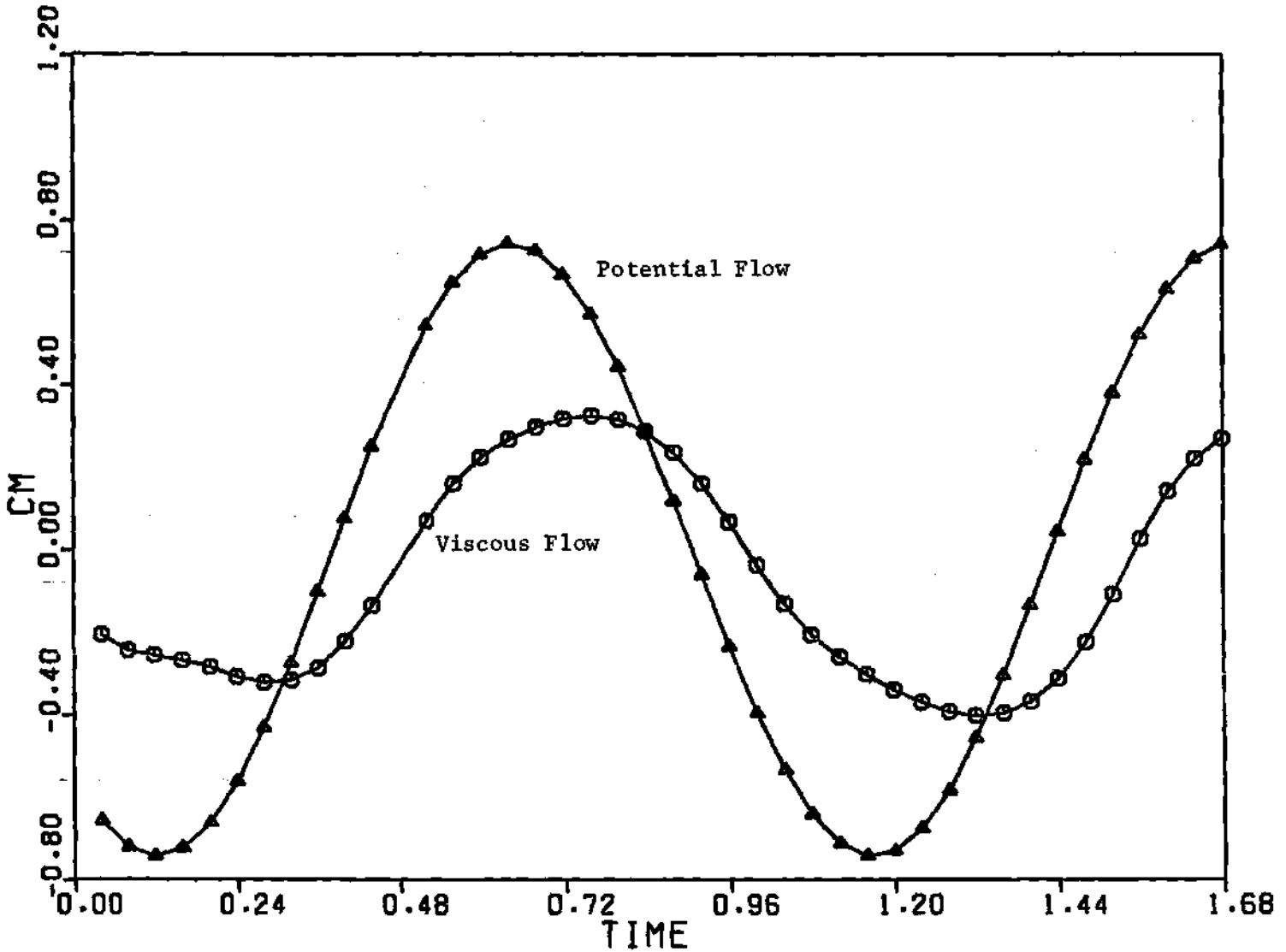

Figure 55. Joukowski 12% Airfoil ($\alpha = 9^{\circ} - 6^{\circ} \cos 6t$)--Moment History

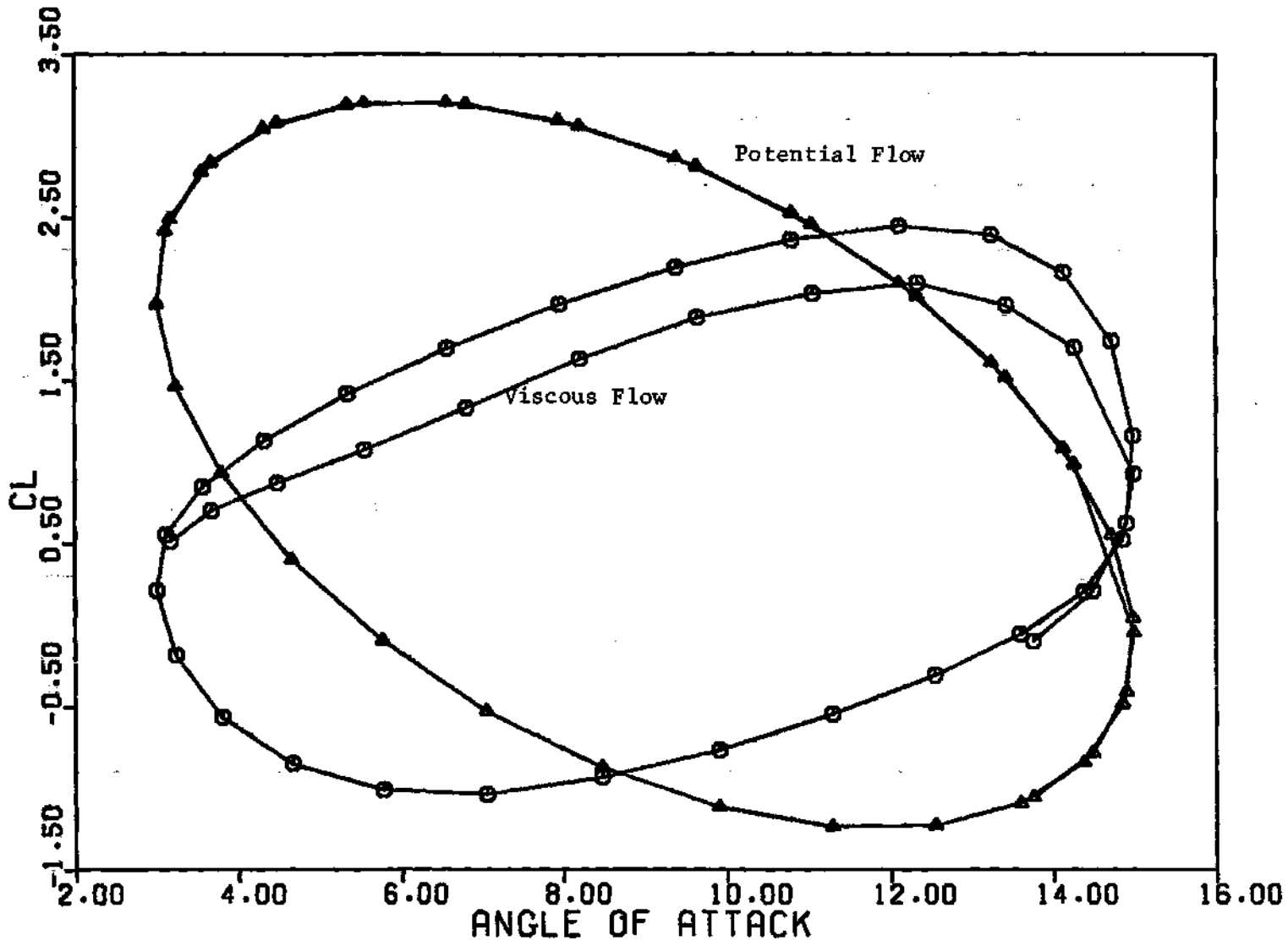

Figure 56. Joukowski 12% Airfoil ($\alpha = 9^{o} - 6^{o} \cos 6t$)--Lift Hysteresis

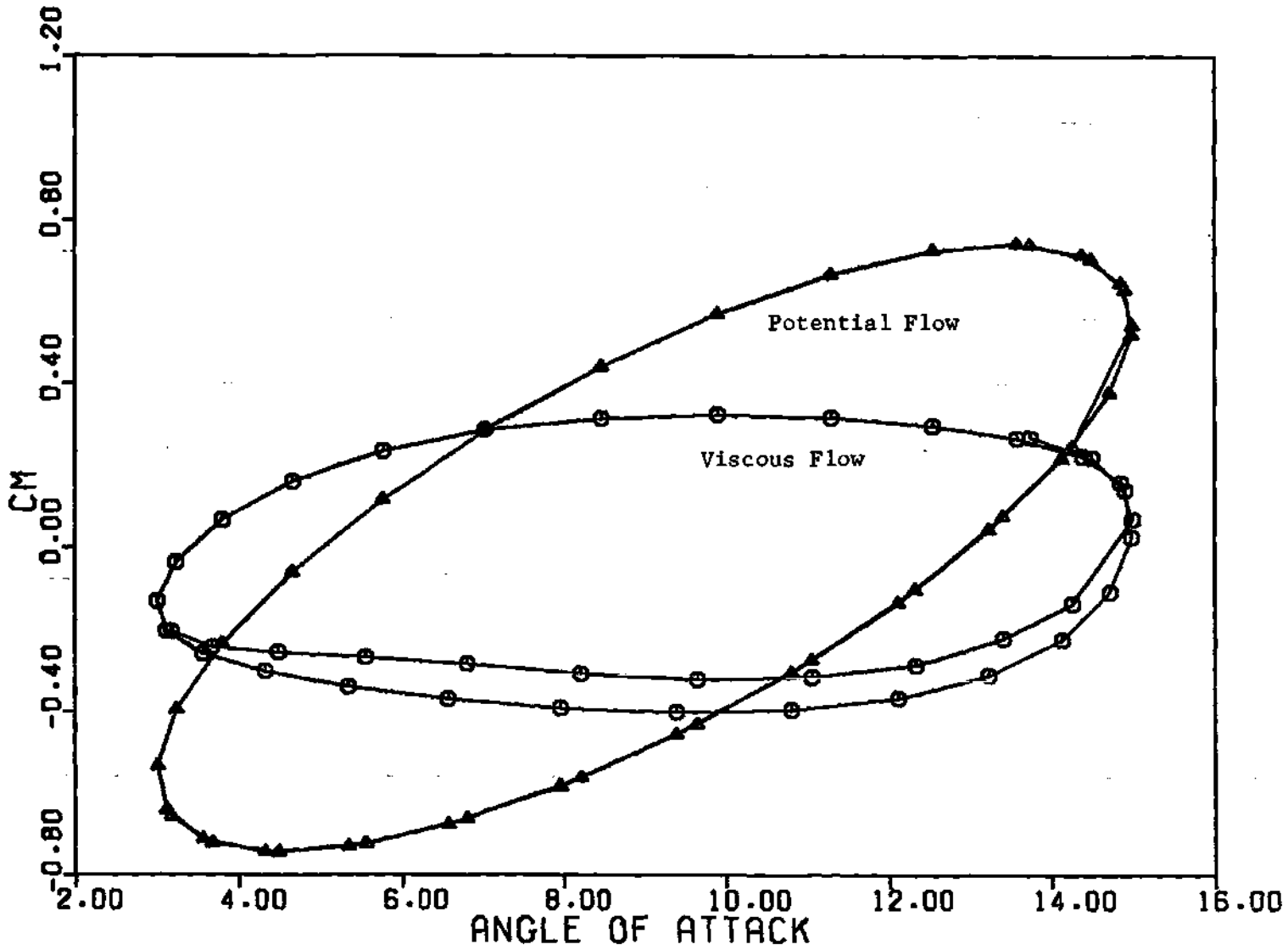

Figure 57. Joukowski 12% Airfoil ($\alpha = 9^{\circ} - 6^{\circ} \cos 6t$)--Moment Hysteresis

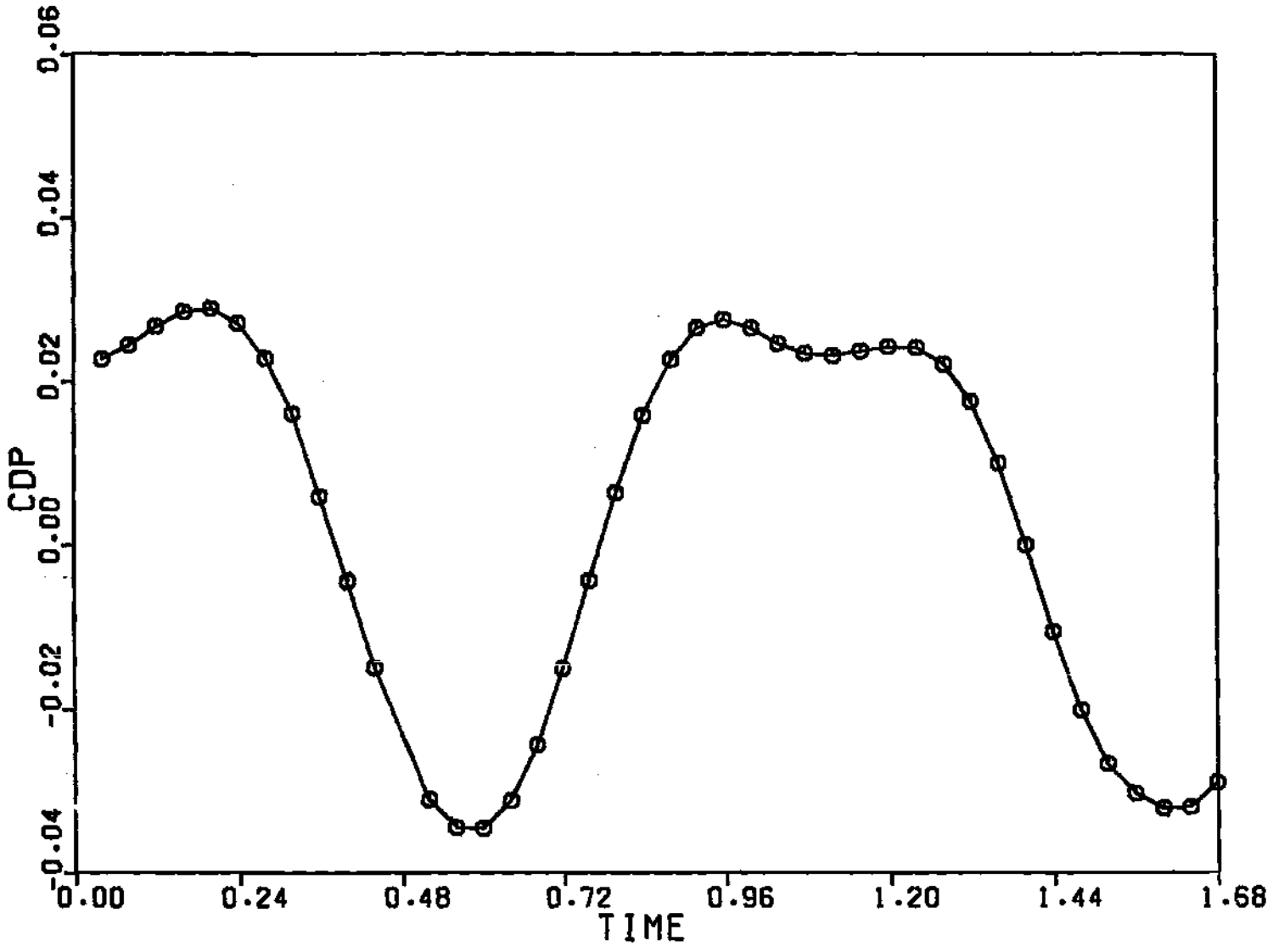

Figure 58. Joukowski 12% Airfoil ($\alpha = 9^{\circ} - 6^{\circ} \cos 6t$)--Pressure Drag History

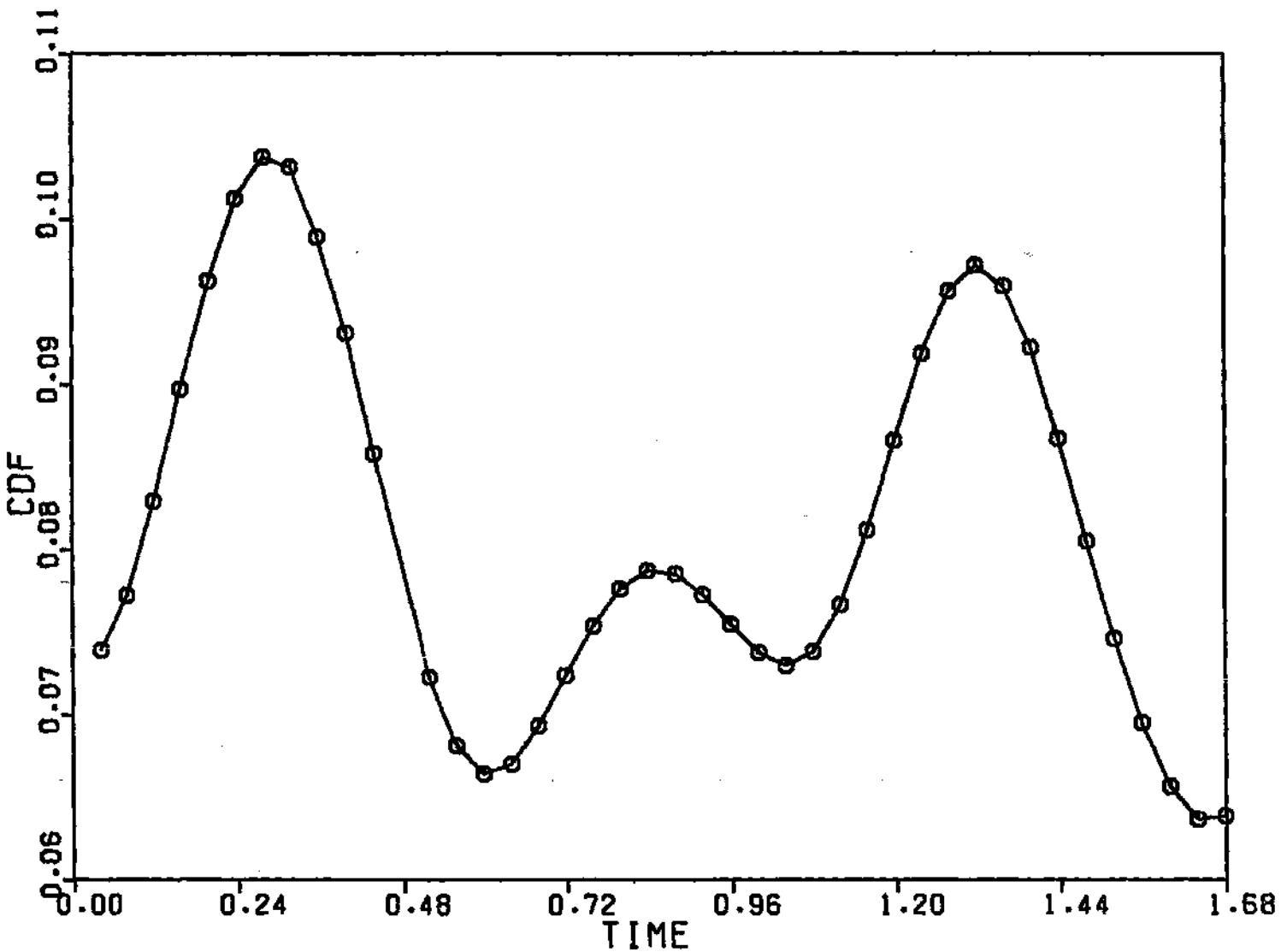

Figure 59. Joukowski 12% Airfoil ($\alpha = 9^{\circ} - 6^{\circ} \cos 6t$)--Viscous Drag History

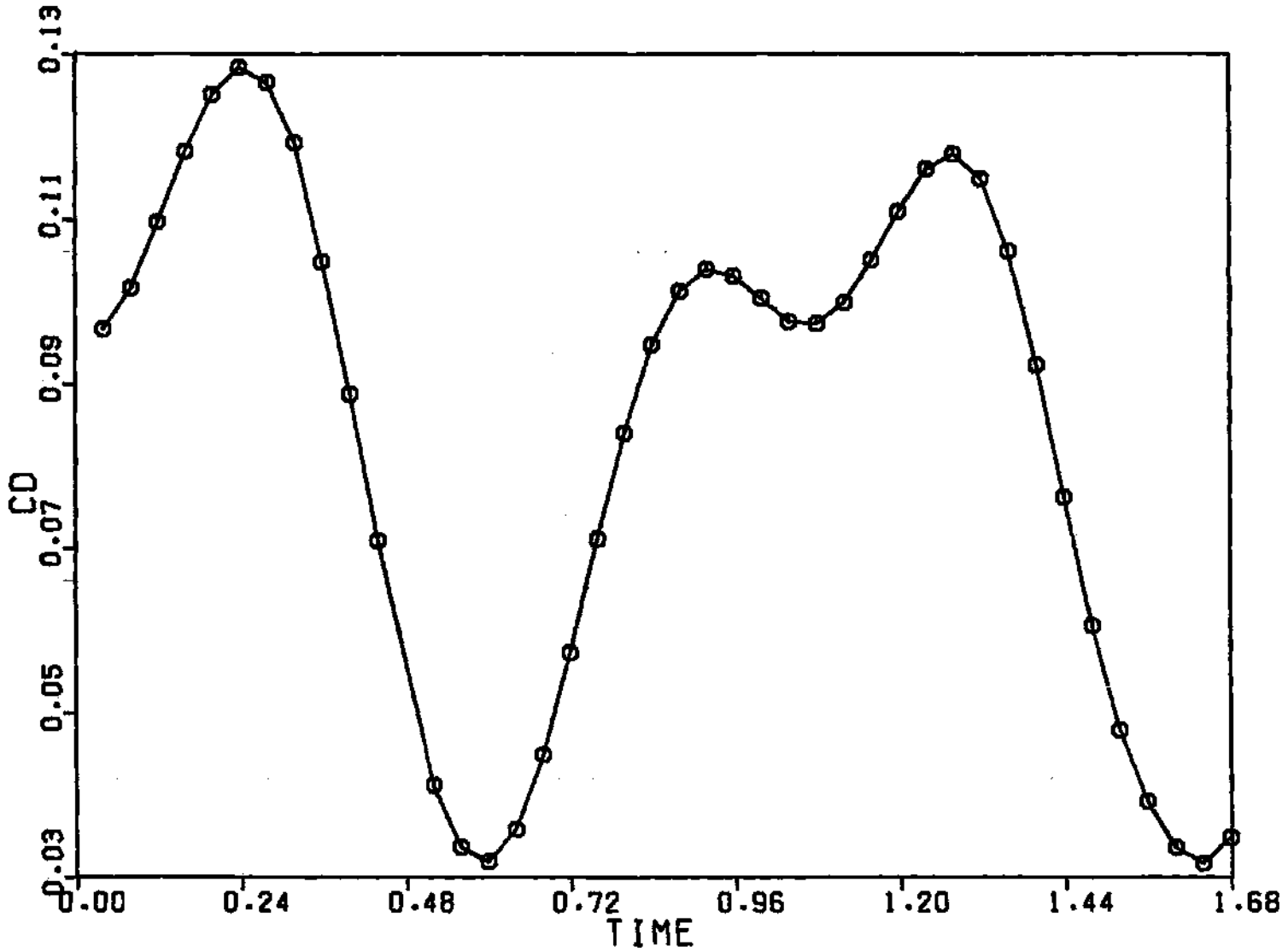

Figure 60. Joukowski 12% Airfoil ($\alpha = 9^{\circ} - 6^{\circ} \cos 6t$)--Total Drag History

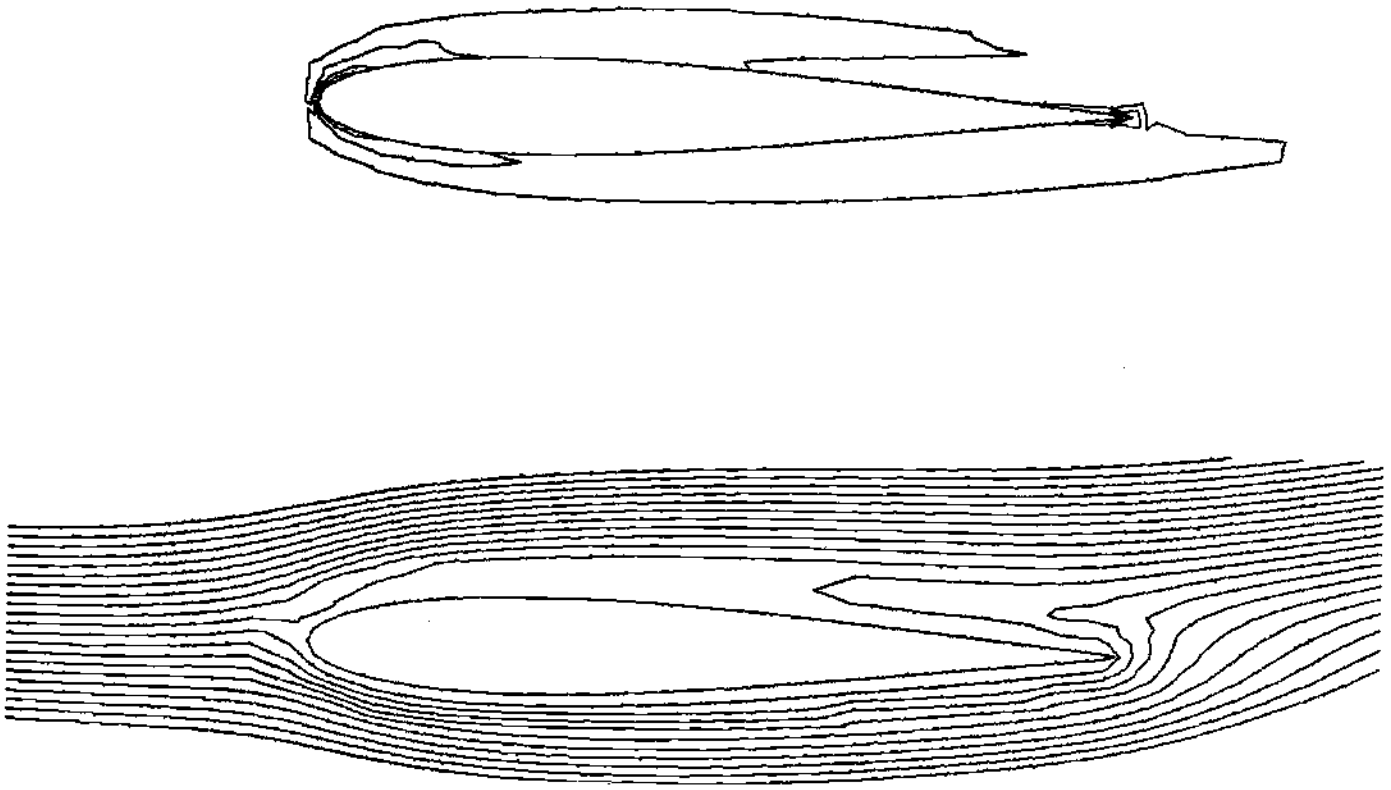

Figure 61. Joukowski 12% Airfoil ($\alpha = 9^{\circ} - 6^{\circ} \cos 6t$)--Streamlines and Constant Vorticity Contours at t = .04

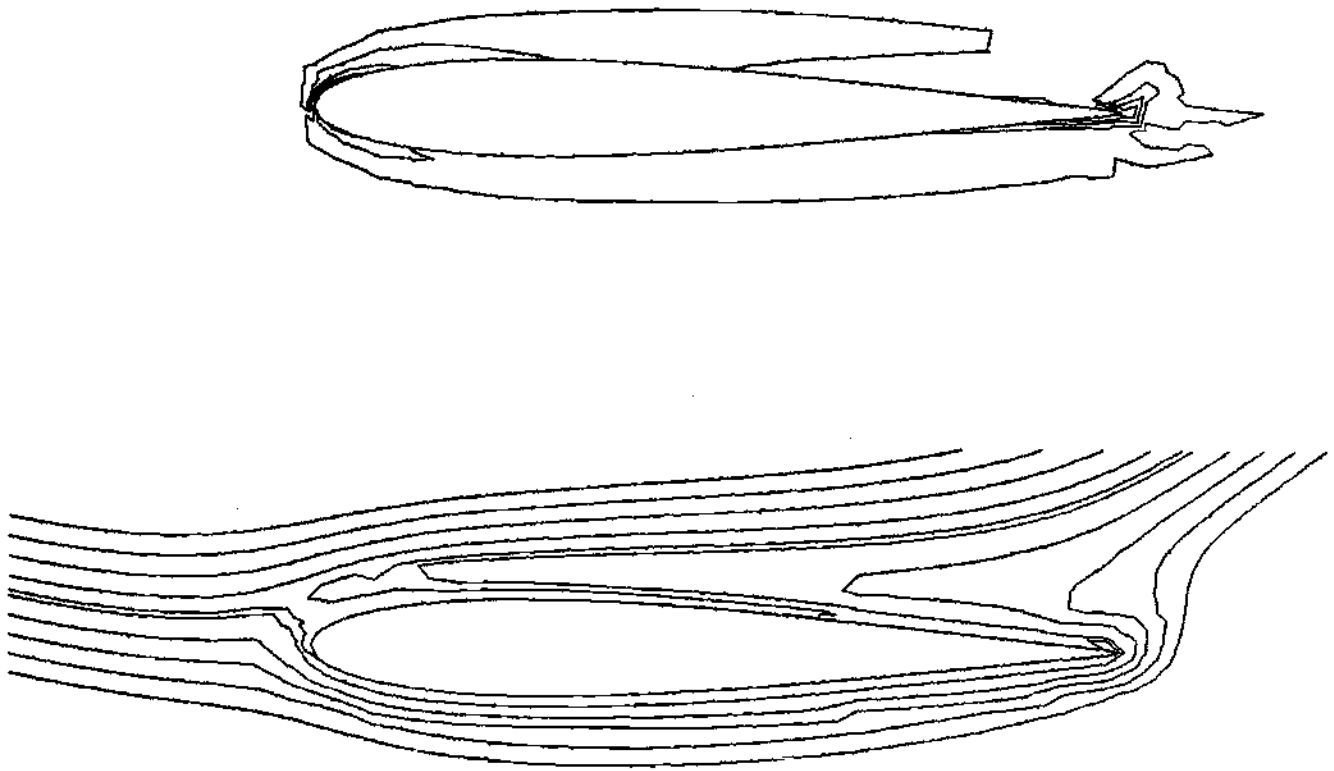

Figure 62. Joukowski 12% Airfoil ($\alpha = 9^{\circ} - 6^{\circ} \cos 6t$)--Streamlines and Constant Vorticity Contours at t = .16

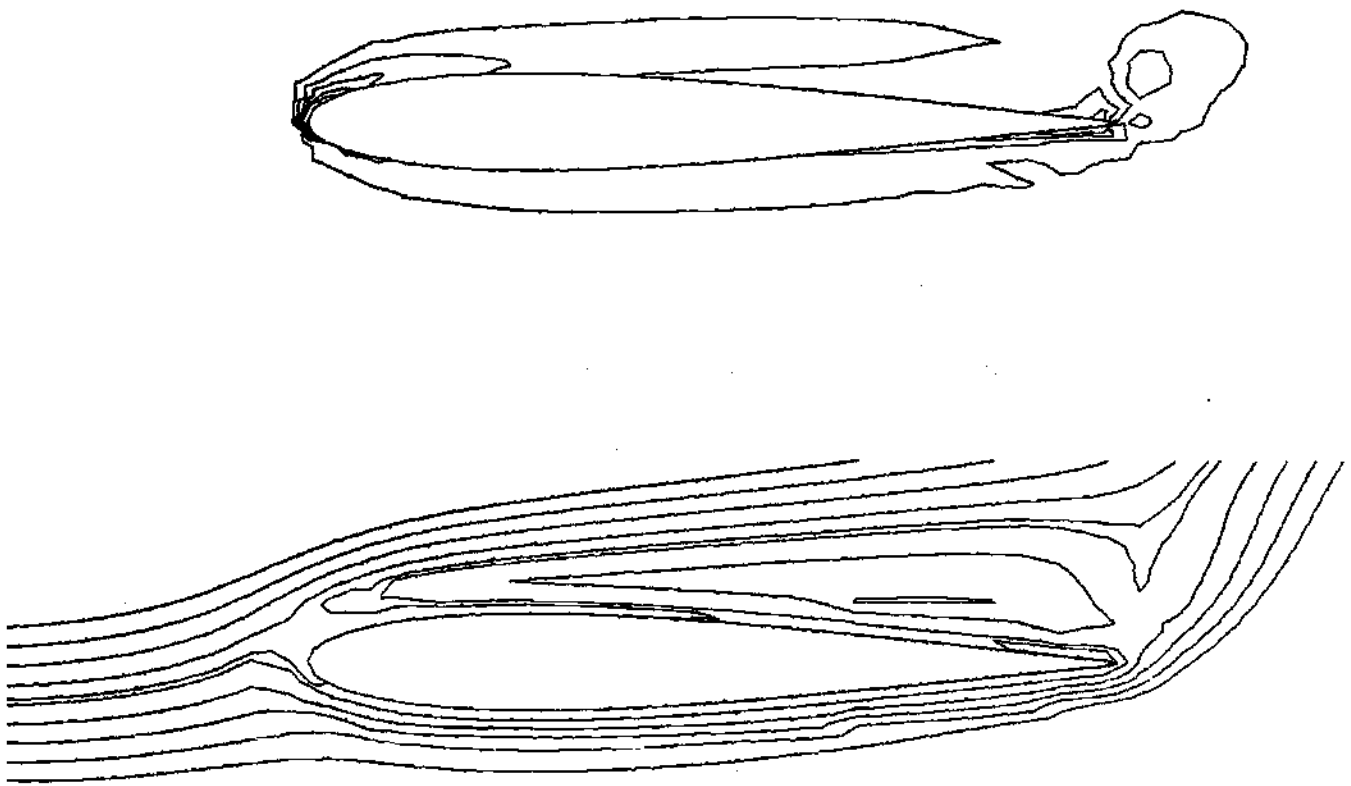

Figure 63. Joukowski 12% Airfoil ($\alpha = 9^{\circ} - 6^{\circ} \cos 6t$)--Streamlines and Constant Vorticity Contours at t = 0.4

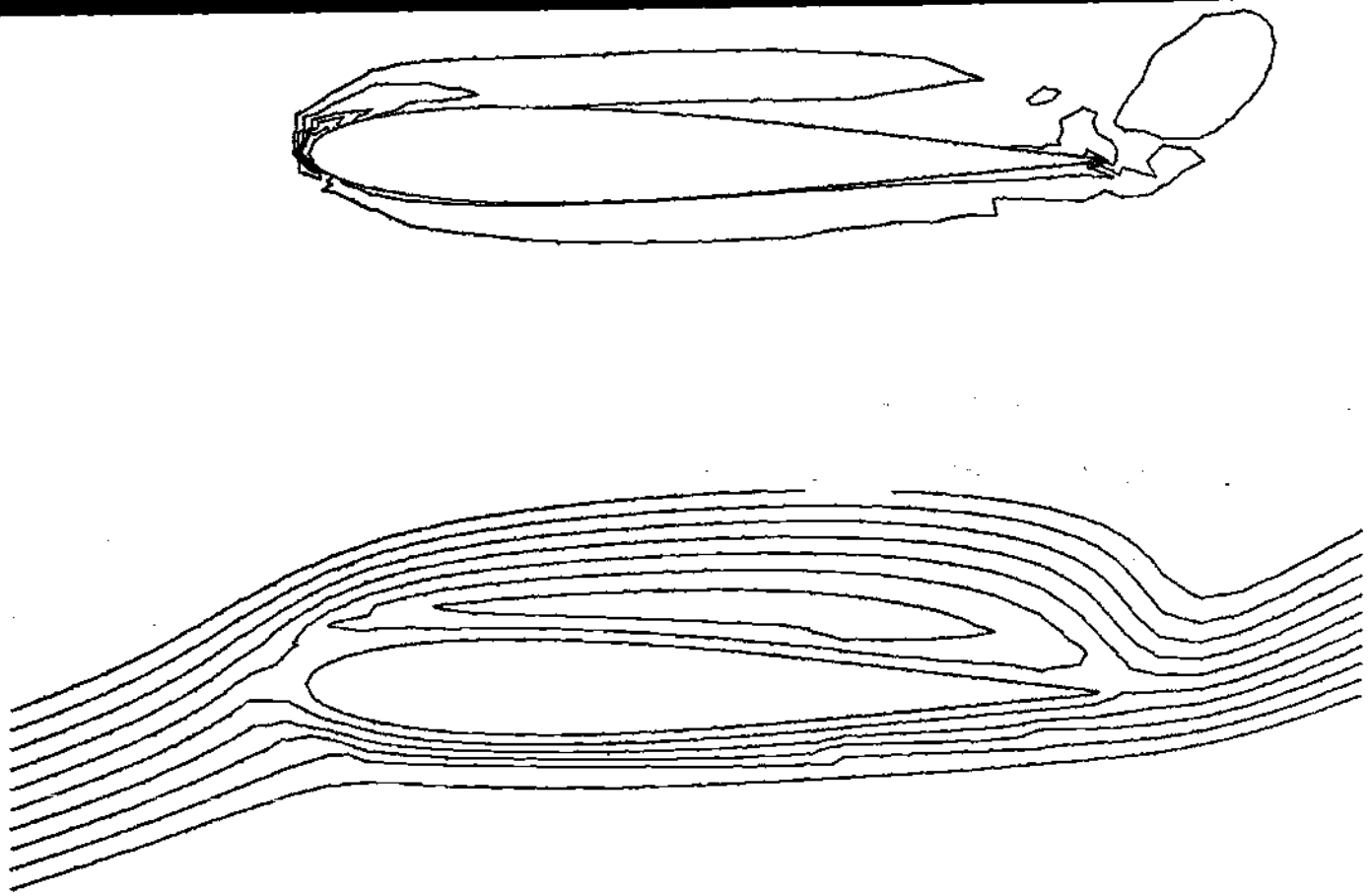

Figure 64. Joukowski 12% Airfoil ($\alpha = 9^{\circ} - 6^{\circ} \cos 6t$)--Streamlines and Constant Vorticity Contours at $t = 0.52$

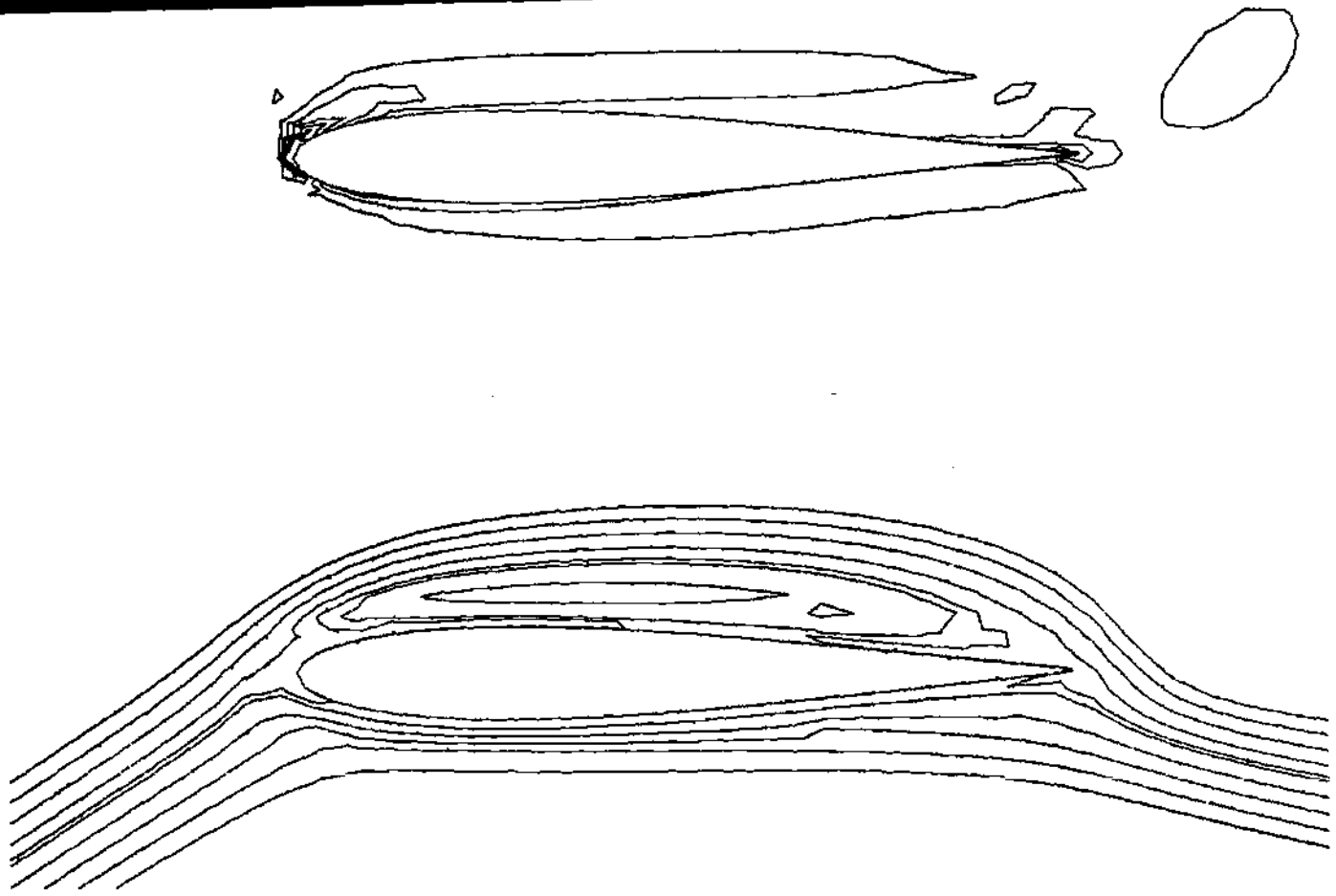

Figure 65. Joukowski 12% Airfoil ($\alpha = 9^{\circ} - 6^{\circ} \cos 6t$)--Streamlines and Constant Vorticity Contours at t = 0.64

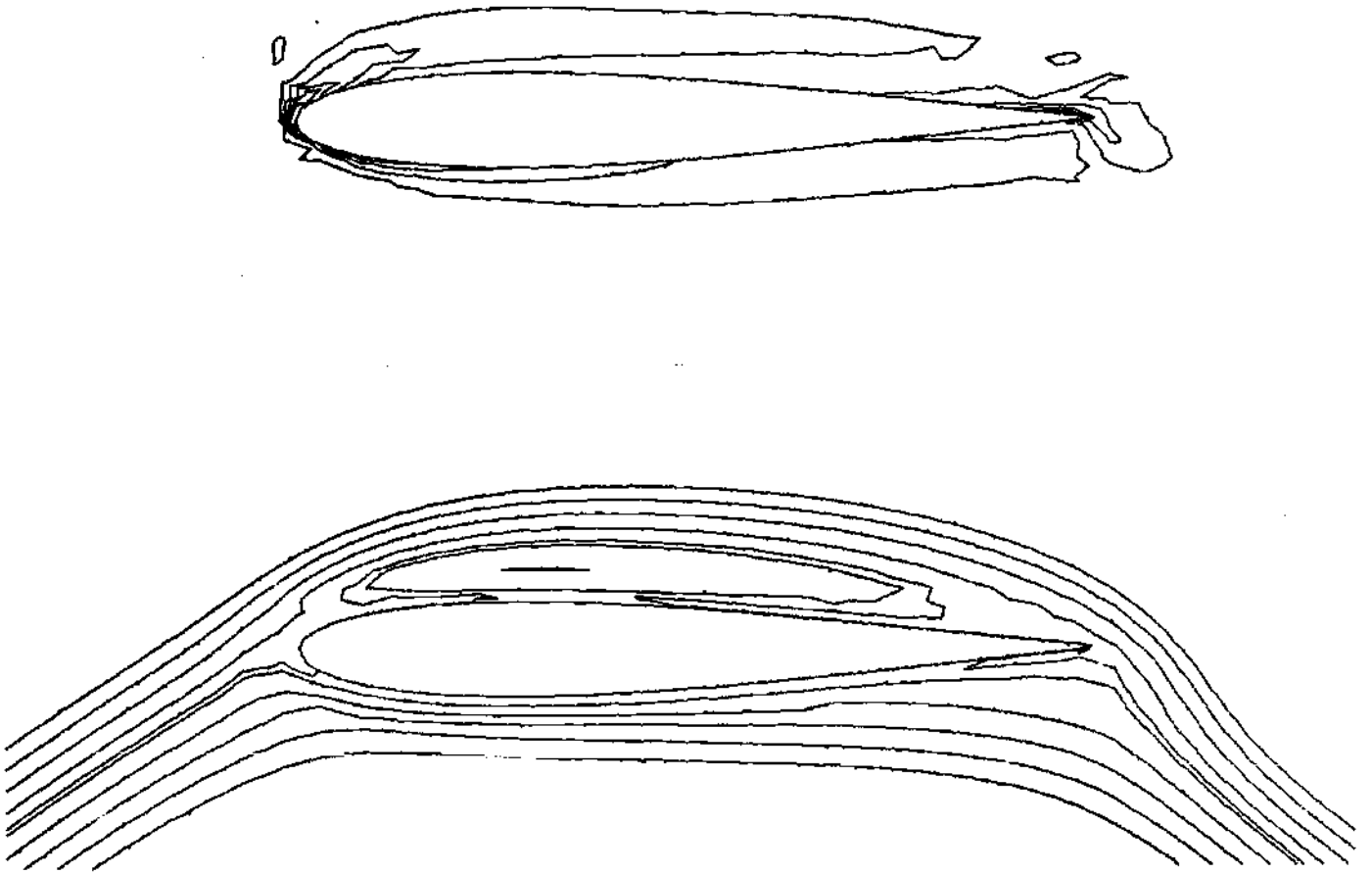

Figure 66. Joukowski 12% Airfoil ($\alpha = 9^{o} - 6^{o} \cos 6t$)--Streamlines and Constant Vorticity Contours at t = 0.76

APPENDIX A

AN EXPLICIT CLOSED FORM SOLUTION FOR THE NEUMANN PROBLEM

In this section, a closed form solution for the Neumann problem is presented for the exterior of a two-dimensional closed surface. In addition, a general solution to the Laplace equation with homogeneous Neumann boundary conditions is also presented.

We consider a region R, exterior of a regular boundary B, where solution to the Laplace equation subject to Neumann type of boundary conditions is to be obtained. The governing relationships are:

(1) Laplace Equation:

$$\nabla^2 \Phi = 0 \tag{A-1}$$

(2) Boundary Conditions:

$$\frac{\partial \Phi}{\partial n} = f_1(\bar{r}_B) \tag{A-2}$$

Here $\bar{r}$ represents the position vector while the subscript B refers to the boundary of the solid.

In addition, for the infinite domain R, it is also necessary to specify the Neumann Boundary conditions very far away from B. The physics of the problem in the present case requires the following condition:

$$\frac{\partial \Phi}{\partial n} = 0. \quad \text{at large distances} \tag{A-3}$$

It is convenient to solve the above problem in a transformed plane. We consider a conformal transformation relationship of the following general form:

$$\zeta = f(Z) = \xi + i\eta = \zeta\, e^{i\phi}$$

Here ζ represents the physical coordinates in the transformed plane (to be called the ζ-plane), while Z represents the coordinates in the physical plane.

Because the transformation is conformal, the Laplace equation retains its form in the ζ-plane as well. Thus,

$$\frac{\partial^2 \Phi}{\partial \xi^2} + \frac{\partial^2 \Phi}{\partial \eta^2} = 0 \qquad \text{(A-4)}$$

the transformation relationship is so chosen that the boundary B is transformed into a unit circle S in the ζ-plane, and the exterior region R is transformed into an infinite domain V exterior of the unit circle. Thus,

$$\zeta_B = f(Z_B) = 1\, e^{i\phi}$$

The stretching relationship between the physical length 'dZ' of an infinite line segment in the physical plane, and the corresponding length in the transformed plane is given by

$$H(\rho,\phi) = \left|\frac{dZ}{d\zeta}\right| \qquad \text{(A-5)}$$

We will be mainly concerned with stretching relationship at the

surface. The following equations hold:

$$dn = H(1,\phi)\ d\rho$$

$$ds = H(1,\phi)\ d\phi$$

Thus, the Neumann boundary condition on B takes the following form in the ζ-plane.

$$\frac{\partial \Phi}{\partial n} = \frac{1}{H(1,\phi)} \quad \frac{\partial \Phi}{\partial \zeta} = f_1(\bar{r}_B)$$

Thus,

$$\frac{\partial \Phi}{\partial \rho} = H(1,\phi)\ f_1(\bar{r}_B) \qquad \text{at the surface.} \tag{A-6}$$

In order to obtain a closed form solution to the Laplace equation, we make use of Green's theorem in its two-dimensional scalar form. If $P(\xi,\eta)$ and $Q(\xi,\eta)$ are two functions possessing continuous second order partial derivatives in the domain V, and possessing continuous first order partial derivatives on S and on S_1 (the far field boundary), then the following relationship is true.

$$\int_V (P\nabla^2 Q - Q\nabla^2 P)\ dV = \int_{S+S_1} (P\nabla Q - Q\nabla P) \cdot n\ dS \tag{A-7}$$

Here $\bar{n}$ is the unit vector pointed away from the domain V, normal to the surface. For the present application, we choose,

$$P = \Phi(x,y) = \Phi(\xi,\eta)$$

$$Q = \frac{1}{4\pi} \log\left(\rho^2 + \rho_o^2 - 2\rho\rho_o \cos\ (\phi-\phi_o)\right) \tag{A-8}$$

It is easy to show that $\nabla^2 Q$ vanishes everywhere except at the point ($\rho = \rho_o$, $\phi = \phi_o$). We are primarily interested in the value of Φ, and $\frac{\partial \Phi}{\partial s}$ on the solid surface. Thus, we are interested in the case where $\rho = 1$, $(-\pi < \phi < \pi)$. So we enclose the point (ρ,ϕ) on the unit circle S with a semicircle of radius ϵ, as shown in the following figure.

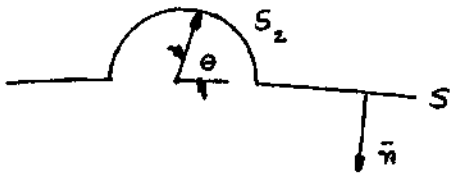

Then on S_2, $\quad \Phi(\rho_o,\phi_o) = \phi(1,\phi) + 0(\epsilon)$

Also on S_2, $\quad Q = \frac{1}{2\pi} \log \epsilon$

$$\frac{\partial Q}{\partial n} = - \frac{1}{2\pi\epsilon}$$

Thus, on S_2,

$$\int_{S_2} (P\nabla Q - Q\nabla P) \cdot \bar{n}\, dS = \int_0^{\pi} \Phi(1,\phi) \left[- \frac{1}{2\pi\epsilon} \right] \epsilon\, d\theta$$

$$- \int_0^{\pi} \frac{1}{2\pi} \log \epsilon \cdot \left(\frac{\partial \Phi}{\partial n} \right) \cdot \epsilon\, d\phi$$

In the limit as $\epsilon \to 0$, the second term on the right hand side vanishes. Thus,

$$\int_{S_2} (P\nabla^2 Q - Q\nabla^2 P) \cdot \bar{n}\, dS = - \frac{\Phi}{2} (1,\phi) \qquad \text{(A-9)}$$

On S_1, the far boundary, from the physics of the problem,

$$\frac{\partial \Phi}{\partial n} = 0.$$

We assume that the far boundary is a circle of radius R, where $R \gg 1$.

On S_1,

$$\frac{\partial Q}{\partial n} = \frac{\partial Q}{\partial \rho_o}\bigg|_{\rho_o = R}$$

Thus,

$$\frac{\partial Q}{\partial n}\bigg|_{S_1} = \underset{\rho_o \to R}{Lt} \frac{1}{2\pi} \frac{2\rho_o - 2\rho\cos(\phi-\phi_o)}{\rho^2 + \rho_o^2 - 2\rho\rho_o\cos(\phi-\phi_o)} \simeq \frac{1}{2\pi R} \quad (R \gg \rho).$$

Thus,

$$\int_{S_1} \left[\Phi \frac{\partial Q}{\partial n} - Q \frac{\partial \Phi}{\partial n}\right] dS = \int_0^{2\pi} \frac{\Phi(R,\theta)}{2\pi R} R d\theta = C_1$$

Where C_1 is a constant. The value of C_1 in general will depend on R.

On S , $\rho_o = 1$. Thus, $Q = \frac{1}{4\pi}\left[1 + \rho^2 - 2\rho\cos(\phi-\phi_o)\right]$

Also,
$$\frac{\partial Q}{\partial n}\bigg|_S = -\frac{\partial Q}{\partial \rho_o}\bigg|_{\rho_o=1} = -\frac{1}{4\pi}\left[\frac{2\rho_o - 2\rho\cos(\phi-\phi_o)}{\rho_o^2 + \rho^2 - 2\rho\rho_o\cos(\phi-\phi_o)}\right]_{\rho_o=1}$$

$$= -\frac{1}{4\pi}\left[\frac{2\rho - 2\cos(\phi-\phi_o)}{1 + \rho^2 - 2\rho\cos(\phi-\phi_o)}\right]$$

Since $\rho=1$ as stated earlier,

$$\left.\frac{\partial Q}{\partial n}\right|_S = -\frac{1}{4\pi} \tag{A-10}$$

Thus, for the surface S, we get

$$\int_S \left[\Phi \frac{\partial Q}{\partial n} - Q \frac{\partial \Phi}{\partial n}\right] dS = \oint_o^{2\pi} \left[\Phi(1,\phi_o) \cdot \left(-\frac{1}{4\pi}\right) - Q \frac{\partial \Phi}{\partial n}\right] d\phi_o$$

$$= C_2 + \frac{1}{4\pi} \oint \log\left[2 - 2\cos(\phi-\phi_o)\right]\left(\frac{\partial \Phi}{\partial \rho_o}\right) d\phi_o$$

Combining all the terms involving S_1, and S_2 and S , and noting that the area integral vanishes, we get the following form:

$$\frac{\Phi}{2}(1,\phi) = C_1 + C_2 + \frac{1}{4\pi} \oint \log\left[2 - 2\cos(\phi-\phi_o)\right] \frac{\partial \Phi}{\partial \rho_o} d\phi_o \tag{A-11}$$

Taking the derivative of Φ with respect to ϕ, we get,

$$\frac{\partial \Phi}{\partial \phi}(1,\phi) = \frac{1}{2\pi} \oint \frac{\sin(\phi-\phi_o)}{1 - \cos(\phi-\phi_o)} \frac{\partial \Phi}{\partial \rho_o} d\phi_o$$

Or, alternatively,

$$\frac{\partial \Phi}{\partial s} = \frac{1}{H(1,\phi)} \frac{\partial \Phi}{\partial \phi} = \frac{1}{2\pi H(1,\phi)} \oint \frac{\sin(\phi-\phi_o)}{1 - \cos(\phi-\phi_o)} \frac{\partial \Phi}{\partial \rho_o} d\phi_o \tag{A-12}$$

Eqs. (A-12) and (A-11) are the desired closed form solutions to the Neumann problem. It is seen from (A-10), that $\Phi(1,\phi)$ can be determined to within an arbitrary constant, as is the usual case with Neumann problems.

Homogeneous Solution to the Laplace Equation

The existence of the function $\Phi(x,y)$ and the fact that $\Phi(x,y)$ satisfies Laplace equation suggests that a conjugate function $\Psi(x,y)$ exists which also satisfies Laplace Equation. In addition, Φ and Ψ obey Cauchy-Riemann conditions. In the ζ-plane, at the surface, the Cauchy-Riemann conditions take the following form:

$$\frac{\partial \Phi}{\partial \rho} = \frac{\partial \Psi}{\partial \Phi} \; ; \qquad \frac{\partial \Psi}{\partial \rho} = - \frac{\partial \Phi}{\partial \phi} \tag{A-13}$$

Using Green's theorem, and the principal solution $Q(\xi,\eta)$ we obtain, in a manner analogous to that outlined in the previous section, for a point (ρ,ϕ) located in V, not necessarily on S,

$$\Psi(\rho,\phi) = \frac{1}{4\pi} \oint \log \left[1 + \rho^2 - 2\rho \cos(\phi-\phi_o)\right] \frac{\partial \Psi}{\partial \rho_o} \, d\phi_o + C \tag{A-14}$$

We want to test if the following relationship is a valid solution to the Laplace equation, with homogeneous Neumann boundary conditions.

$$\frac{\partial \Phi}{\partial s} = \frac{1}{H(1,\theta)} \qquad \text{on S} \tag{A-15}$$

Using the stretching relationships, we get

$$\frac{\partial \Phi}{\partial \phi} = 1 \qquad \text{on S.}$$

From Cauchy-Riemann conditions,

$$\frac{\partial \Psi}{\partial \rho} = - \frac{\partial \Phi}{\partial \phi} = - 1 \qquad \text{on S.}$$

Thus Eq. (A-14) becomes, for the above condition,

$$\Psi(\rho,\phi) = -\frac{1}{4\pi}\oint \log\left[1 + \rho^2 - 2\rho\cos(\phi-\phi_o)\right] d\phi + C$$

$$= \log\rho + C \qquad \rho > 1$$

$$= C \qquad \rho < 1$$

If $\Psi(x,y)$ is interpreted as the stream function, the distribution (A-15) gives streamlines that are concentric circles outside the unit circle in the ρ-plane, and constant values of Ψ inside the circle. At the surface, in particular,

$$\frac{\partial\Phi}{\partial n} = \frac{1}{H(1,\phi)}\frac{\partial\Phi}{\partial\rho}\Big|_{\rho=1}$$

$$= \frac{1}{H(1,\phi)}\frac{\partial\Psi}{\partial\phi}\Big|_{\rho=1} = 0 \qquad \text{(A-16)}$$

The condition (A-16) is clearly the homogeneous Neumann boundary condition. Thus the distribution (A-15) is a valid solution to the Neumann problem for the region exterior to the solid for homogeneous Neumann boundary conditions. The distribution (A-15) by virtue of (A-16) produces zero normal velocity at the surface.

APPENDIX B

DEVELOPMENT OF MOMENTUM EQUATION FOR THE TANGENTIAL VELOCITY AT THE SURFACE

In a rotating coordinate system, the vector momentum equation is given by Eq. (3).

$$\frac{\partial \bar{v}}{\partial t} + (\bar{v} \cdot \bar{\nabla})\,\bar{v} = \frac{1}{\rho}\,\bar{\nabla} p + \nu \bar{\nabla}^2 \bar{v} - \dot{\bar{\Omega}} \times \bar{r} - 2(\bar{\Omega} \times \bar{v}) - \bar{\Omega} \times (\bar{\Omega} \times \bar{r}) \qquad \text{(B-1)}$$

At the surface, the momentum equation is reduced to the following simple form because of no slip conditions.

$$\nu \bar{\nabla}^2 \bar{v} - \frac{1}{\rho}\,\bar{\nabla} p - \dot{\bar{\Omega}} \times \bar{r} - \bar{\Omega} \times (\bar{\Omega} \times \bar{r}) = 0 \,. \qquad \text{(B-2)}$$

Taking the dot product of the above vector equation with respect to $\bar{t}$, where $\bar{t}$ is the unit tangential vector at the surface defined positive in the counter clockwise sense, we get

$$-\frac{1}{\rho}\frac{\partial p}{\partial s} + \nu \nabla^2 v_t - (\dot{\bar{\Omega}} \times \bar{r}) \cdot \bar{t} - [\bar{\Omega} \times (\bar{\Omega} \times \bar{r})] \cdot \bar{t} = 0. \qquad \text{(B-3)}$$

Here v_t is the tangential component of the velocity vector defined positive in the counterclockwise sense; s is the coordinate direction tangential to the surface, measured positive in the counterclockwise sense.

The surface is defined in the polar coordinates by the following equation:

$$r = r(\theta) \quad \text{where } r = \sqrt{x^2 + y^2} \quad \text{and} \quad \theta = \tan^{-1}\frac{y}{x} . \tag{B-4}$$

also

$$x = r\cos\theta \tag{B-5}$$

$$y = r\sin\theta$$

$$\bar{t} = \frac{dx}{ds}\bar{i} + \frac{dy}{ds}\bar{j} \tag{B-6}$$

Now, from (B-5)

$$dx = -r\sin\theta\, d\theta + \cos\theta\, dr$$

$$dy = r\cos\theta\, d\theta + \sin\theta\, dr$$

Thus,

$$(\Omega \times r) \cdot t = [\dot{\Omega}\tilde{k} \times (x\tilde{i} + y\tilde{j})] \cdot \left[\frac{dx}{ds}\bar{i} + \frac{dy}{ds}\bar{j}\right]$$

$$= \dot{\Omega}[r\cos\theta\ \bar{j} - r\sin\theta\ \bar{i}] \cdot \left[\frac{dx}{ds}\bar{i} + \frac{dy}{ds}\bar{j}\right] \tag{B-8}$$

$$= \dot{\Omega}r^2\frac{d\theta}{ds}$$

$$[\bar{\Omega} \times (\bar{\Omega} \times \bar{r})] \cdot \bar{t} = -\Omega^2(x\bar{i} + y\bar{j}) \cdot \bar{t}$$

$$= -\Omega^2 r\frac{dr}{ds} \tag{B-9}$$

Also, $$\bar{\nabla}^2 v_t = \frac{\partial^2 v_t}{\partial s^2} + \frac{\partial^2 v_t}{\partial n^2}$$

Because of no-slip condition v_t is zero everywhere on the surface. Thus $\frac{\partial^2 v_t}{\partial s^2}$ is zero. So, we get

$$\tilde{\nabla}^2 v_t = \frac{\partial^2 v_t}{\partial n^2} \tag{B-10}$$

Combining all the terms, Eq. (B-3) reduces to the following form.

$$-\frac{1}{\rho}\frac{\partial p}{\partial s} + \nu \frac{\partial^2 v_t}{\partial n^2} - \dot{\Omega} r^2 \frac{d\theta}{ds} + \Omega r^2 \frac{dr}{ds} = 0 \ . \tag{B-11}$$

APPENDIX C

EVALUATION OF THE LINE INTEGRALS APPEARING IN THE SURFACE VORTICITY SCHEME

We consider Eq. (53):

$$\gamma_1 = v_{t_1} + \frac{1}{2\pi H(1,\theta)} \oint \frac{\sin(\theta-\theta_o)}{1 - \cos(\theta-\theta_o)} v_{n_2} H(1,\theta_o)\, d\theta_o \qquad \text{(C-1)}$$

Assume

$$f(\theta_o) = v_{n_2} H(1,\theta_o) = \sum_{\mu=0}^{N} a_\mu \cos\mu\,\theta_o + \sum_{\mu=1}^{N-1} b_\mu \sin\mu\,\theta_o \qquad \text{(C-2)}$$

Then, from the theory of Fourier Series,

$$a_o = \frac{1}{2N} \sum_{\nu=0}^{2N-1} f_\nu$$

$$a_\mu = \frac{1}{N} \sum_{\nu=0}^{2N-1} f_\nu \cos\mu\,\theta_\nu \qquad \mu=1,2,\ldots,(N-1)$$

$$b_\mu = \frac{1}{N} \sum_{\nu=0}^{2N-1} f_\nu \sin\mu\,\theta_\nu \qquad \mu=1,2,\ldots,(N-1)$$

$$a_N = \frac{1}{2N} \sum_{\nu=0}^{2N-1} f_\nu \cos N\,\theta_\nu \qquad \text{(C-3)}$$

Once the Fourier coefficients are determined, Eq. (C-1) becomes,

$$\gamma_1 = v_{t_1} + \frac{1}{2\pi H(1,\theta)} \sum_{\mu=0}^{N} a_\mu \oint \frac{\sin(\theta-\theta_o)}{1 - \cos(\theta-\theta_o)} \cos\mu\,\theta_o d\theta_o$$

$$+ \frac{1}{2\pi H(1,\theta)} \sum_{\mu=1}^{N-1} b_\mu \oint \frac{\sin(\theta-\theta_o)}{1 - \cos(\theta-\theta_o)} \sin\mu\,\theta_o d\theta_o \qquad \text{(C-4)}$$

We consider

$$I_\mu(\theta) = \oint \frac{\sin(\theta-\theta_o)}{1 - \cos(\theta-\theta_o)} \cos\mu\,\theta_o d\theta_o \qquad \text{(C-5)}$$

It is clear that $I_o(\theta) = 0$ because the integrand is an odd function of θ_o when $\mu = 0$.

For other values of μ,

$$\cos\mu\,\theta_o = \cos\mu(\theta_o - \theta + \theta) = \cos\mu(\theta_o - \theta)\cos\mu\theta$$

$$- \sin\mu(\theta_o - \theta)\sin\mu\theta \qquad \text{(C-6)}$$

Thus,

$$I_\mu(\theta) = \cos\mu\theta \int \frac{\sin(\theta-\theta_o)}{1 - \cos(\theta-\theta_o)} \cos\mu(\theta_o - \theta)\, d\theta_o$$

$$- \sin\mu\theta \int \frac{\sin(\theta-\theta_o)}{1 - \cos(\theta-\theta_o)} \sin\mu(\theta_o - \theta)\, d\theta_o \qquad \text{(C-7)}$$

We define $\phi = \theta_o - \theta$. The first integral on the right hand side of Eq. (C-7) vanishes because the integrand is odd. Thus Eq. (C-7) simplifies

to the following form.

$$I_\mu(\theta) = -\sin\mu\theta \int_{-\pi}^{\pi} \frac{\sin\phi \sin\mu\phi}{1 - \cos\phi}\, d\phi$$

$$= \frac{-\sin\mu\theta}{2} \oint \left[\frac{\cos(\mu-1)\,\phi}{1 - \cos\phi} - \frac{\cos(\mu+1)\,\phi}{1 - \cos\phi}\right] d\phi \qquad \text{(C-8)}$$

From the integral tables,

$$\int_{-\pi}^{\pi} \frac{\cos n\theta}{1 + a^2 - 2a\cos\theta}\, d\theta = \frac{2\pi a^n}{1 - a^2} \qquad a^2 < 1 \qquad \text{(C-9)}$$

Thus,

$$I_\mu(\theta) = \lim_{a\to 1} -\sin\mu\theta \left[\int_{-\pi}^{\pi} \frac{\cos(\mu-1)\,\phi - \cos(\mu+1)\,\phi}{(1 + a^2 - 2a\cos\phi)}\, d\phi\right]$$

$$= -\sin\mu\theta \lim_{a\to 1} \left[\frac{2\pi}{1 - a^2}\,(a^{\mu-1} - a^{\mu+1})\right]$$

$$= -2\pi \sin\mu\theta \qquad \text{(C-10)}$$

Also,

$$J_\mu(\theta) = \oint \frac{\sin(\theta-\theta_o)}{1 - \cos(\theta-\theta_o)} \sin\mu\theta_o d\theta_o$$

$$J_\mu(\theta) = \cos\mu\theta \oint \frac{\sin(\theta-\theta_o)}{1 - \cos(\theta-\theta_o)} \sin\mu(\theta_o - \theta)\, d\theta_o$$

$$+ \sin\mu\theta \oint \frac{\sin(\theta-\theta_o)}{1 - \cos(\theta-\theta_o)} \cos\mu(\theta_o - \theta)\, d\theta_o$$

$$= 2\pi \cos\mu\theta \qquad \text{(C-11)}$$

Thus Eq. (C-4) simplifies to the following form.

$$\gamma_1 = v_{t_1} + \frac{1}{H(\theta)} \sum_{\mu=1}^{N-1} (b_\mu \cos \mu\theta - a_\mu \sin \mu\theta) \qquad \text{(C-12)}$$

Check:

We consider the potential flow over circular cylinder as a test case. At the surface,

$v_{t_1} = -\sin\theta \qquad v_{n_1} = -\cos\theta \qquad H(\theta) = 1$

$v_{n_2} = +\cos\theta$. Thus, by inspection,

$a_1 = 1; \quad a_n = 0 \ (n>1); \quad b_n = 0 \quad$ for all n

Then, from Eq. (C-12)

$\gamma_1 = -\sin\theta - \sin\theta = -2\sin\theta$

This is the desired potential flow velocity distribution. Upon using no-slip condition, γ_1 is also the desired vortex sheet strength.

APPENDIX D

EXTENSION OF GALERKIN METHOD TO ACCOMODATE INTERNAL BOUNDARY CONTINUITY CONDITIONS

In Chapter III, Galerkin method has been used to treat the vorticity transport equation in the neighborhood of the airfoil. This method, as applied in the present context, makes use of linear interpolation functions for the dependent variable ω', as well as the coefficients u and v appearing in the convection terms.

The use of linear interpolation functions guarantees the continuity of ω' across the internal boundaries (i.e. element interfaces). However, it does not guarantee that the derivatives of ω' also will be continuous across the internal boundaries. The physics of the problem demands that all derivatives of ω' be continuous in the fluid domain. Therefore, it is desirable to ensure the continuity of the vorticity as well as its derivatives. One way of satisfying this condition will be to use higher order interpolation functions. However, it is possible to satisfy these continuity conditions, at least in an average sense, by an extension of Galerkin method as shown in Ref. 32.

For the purpose of illustrating how Galerkin's method may be extended to allow for discontinuities the following simple example will be considered here.

We seek the solution of the following boundary value problem

$$\frac{d^2\phi}{dx^2} = 0 \; . \qquad\qquad 0 < x < L$$

according to the boundary conditions:

$$\phi(x = 0) = \phi_o$$

$$\phi(L) \quad = \phi_L$$

where ϕ_o and ϕ_L are sepcified constants.

At each internal node 'i', we need to satisfy

$$\phi(x_i^+) = \phi(x_i^-)$$

$$\frac{d\phi}{dx}(x_i^+) = \frac{d\phi}{dx}(x_i^-).$$

where $x_i^+ = x_i + \epsilon$ and $x_i^- = x_i - \epsilon$ and $0 < \epsilon \ll 1$.

The domain of interest ($0 \le x \le L$) is divided into M_1 subdomains or finite elements. Associated with each node i, there exists a linear function $N_i(x)$ with the following properties:

$$N_i(x_j) = 1 \qquad i = j \qquad 0 \le x_j \le L$$

$$= 0 \qquad i \neq j \qquad 0 \le x_j \le L$$

Thus, the function $\phi(x)$ may be written in the following form:

$$\phi(x) = \sum_{i=1}^{M_2} N_i(x)\, \phi_i(x) \qquad 0 \le x \le L$$

Here M_2 is the total number of nodes including the end nodes. It is clear that in the above case M_2 will be equal to $M_1 + 1$. Then,

according to Ref. 32, the complete Galerkin formulation for the present problem, which takes into account the governing equation, as well as the continuity conditions is given by the following equation:

$$\sum_{r=1}^{M_1} \int_{x_y}^{x_{r+1}} \frac{d^2\phi}{dx^2} N_i(x)\, dx - N_i(x) \left[\sum_{n=1}^{M_1-1} \left[\left(\frac{d\phi}{dx}\right)_{x_n}^{+} - \left(\frac{d\phi}{dx}\right)_{x_n}^{-} \right] \right] = 0.$$

In the above equation, the first term represents sum of integrals. The second term represents sum over all the (M_1-1) interior nodes. It is possible to integrate the first term by part in the following manner:

$$\int_{x_r}^{x_{r+1}} \frac{d^2\phi}{dx^2} N_i dx = \left[N_i \frac{d\phi}{dx} \right]_{x_r}^{x_{r+1}} - \int_{x_r}^{x_{r+1}} \frac{d\phi}{dx} \frac{dN_i}{dx}\, dx$$

Thus, we obtain the following form:

$$- \sum_{r=1}^{M_1} \int_{r} \frac{d\phi}{dx} \frac{dN_i}{dx}\, dx = 0 \ .$$

We can obtain (M_1-1) such equations for the (M_1-1) unknown nodal values by varying i from 2 to M_1. Finally, the boundary values ϕ_o and ϕ_L may be substituted in the above equation in the place of ϕ_1 and ϕ_{M+1} respectively.

It is possible to extend the above procedure to two dimensional problems, and in particular to the vorticity transport equation. The final result obtained by the above extended Galerkin's method would be identical to that given by Eq. (39). However, it is clear that the above procedure deals with the internal continuity conditions on a firmer

mathematical basis.

REFERENCES

1. Crimi P. and Reeves, B. L., "A Method for Analyzing Dynamic Stall of Helicopter Rotors," NASA CR-2009, 1972.

2. Launder, B. E. and Spalding, D. B., "The Numerical Computation of Turbulent Flows," Computer methods in Appl. Mech. and Engrg., pp. 269-289, March 1974.

3. Wu, J. C., "Numerical Boundary Conditions for Viscous Flow Problems," AIAA Journal, Vol. 14, No. 8, pp. 1042-1049, August 1976.

4. Mehta, U. B. and Lavan, Z., "Starting Vortex, Separation Bubbles and Stall--A Numerical Study of Laminar Unsteady Flow Around an Airfoil," J. Fluid Mechanics, Vol. 67, pp. 227-256, 1975.

5. Mehta, U. B., "Dynamic Stall of an Oscillating Airfoil," Proceedings, AGARD Fluid Dynamics Panel Symposium on Unsteady Aerodynamics, Ottawa, Canada, 1977.

6. Wu, J. C. and Sampath, S., "A Numerical Study of Viscous Flow Around an Airfoil," AIAA 9th Fluid and Plasma Dynamics Conference, Paper No. 76-337, July 1976.

7. Thompson, J. F., Thames, F. C. and Mastin, C. W., "Boundary-Fitted Coordinate Systems for Solution of Partial Differential Equations on Fields Containing any Number of Arbitrary Two-Dimensional Bodies," NASA, CR-2729, 1977.

8. Kinney, R. B., "Two-Dimensional Viscous-Flow Past an Airfoil in an Unsteady Airstream," Proceedings, AGARD Fluid Dynamics Panel Symposium on Unsteady Aerodynamics, Ottawa, Canada, 1977.

9. Bratanow, T. and Ecer, A., "On the Application of the Finite Element Method in Unsteady Aerodynamics," AIAA Journal, Vol. 12, No. 4, pp. 503-510, April 1974.

10. Bratanow, T., Aksu, H. and Spehert, T., "A Rigorous Solution of the Navier-Stokes Equations for Unsteady Viscous Flow at High Reynolds Numbers around Oscillating Airfoils," AIAA Paper 75-863, June 1975.

11. Wu, J. C. and Thompson, J. F., "Numerical Solutions of Time-Dependent Incompressible Navier-Stokes Equations Using an

Integro-Differential Formulation," Computers and Fluids, Vol. I, pp. 197-215, 1973.

12. Schlichting, H., Boundary Layer Theory, McGraw-Hill Book Co., Inc., 1960.

13. Wahbah, M. M., "Evaluation of Shape Functions Associated with the Finite Element Solution of the Integral Representation for Two-Dimensional Flows," Unpublished Notes, Georgia Institute of Technology, Atlanta, Georgia, 1976.

14. Roache, P. J., Computational Fluid Dynamics, Hermosa Publishers, Alburquerque, New Mexico, 1972.

15. Sampath, S., "Numerical Solution of Navier-Stokes Equations for Incompressible Two-Dimensional Flow Past a Finite Flat Plate," Unpublished Notes, Georgia Institute of Technology, Atlanta, Georgia, 1974.

16. Grove, A. S., Shair, F. H., Petersen, E. E. and Andreas, A., "An Experimental Investigation of the Steady Separated Flow Past a Circular Cylinder," J. Fluid Mech., Vol. 19, pp. 60-80, 1964.

17. Kawaguti, M., "Numerical Solutions of Navier-Stokes Equations for Flow Around a Circular Cylinder at Reynolds Number 40," J. Phys. Soc. Japan, Vol. 8, No. 6, 1953.

18. Apelt, C. J., "The Steady Flow of a Viscous Fluid Past a Circular Cylinder at Reynolds Numbers 40 and 44," Reports and Memoranda, No. 3175, Aero. Res. Council, London, 1958.

19. Kawaguti, M. and Jain, P., "Numerical Study of a Viscous Fluid Past a Circular Cylinder," University of Wisconsin, M.R.C. Summary Report No. 590, 1965.

20. Jain, P. C. and Rao, K. S., "Numerical Solution of Unsteady Viscous Incompressible Fluid Flow Past a Circular Cylinder," Phys. of Fluids, Vol. 12, Supplement II, II-57, 1969.

21. Ives, D. C., "A Modern Look at Conformal Mapping Including Multiply Connected Regions," AIAA J., Vol. 14, No. 8, pp. 1006-1011, 1976.

22. Taneda, S., "The Development of the Lift of an Impulsively Started Elliptic Cylinder at Incidence," J. Phys. Soc. of Japan, Vol. 33, No. 6, pp. 1706-1711, 1972.

23. Bisplinghoff, R. L., Ashley, H. and Halfman, R. L., Aeroelasticity, Addison-Wesley, Reading, Mass., 1957.

24. Kottapalli, S. B. R., "Drag on an Oscillating Airfoil," Ph.D. Thesis, Georgia Institute of Technology, Atlanta, Georgia, 1977.

25. McCroskey, W. J., "Inviscid Flow Field of an Unsteady Airfoil," AIAA J., Vol. 11, No. 8, pp. 1130-1137, August 1973.

26. Ericsson, L. E., "Comment on Unsteady Airfoil Stall," J. of Aircraft, Vol. 4, No. 5, pp. 478-480, September-October 1967.

27. Ericsson, L. E. and Reding, J. P., "Dynamic Stall Analysis in Light of Recent Numerical and Experimental Results," AIAA 13th Aerospace Sciences Meeting, Paper No. 75-26, January 1975.

28. Carta, F. O., "A Theoretical Study of the Effect of Unsteady Pressure Gradient on Dynamic Stall Delay," J. of Aircraft, Vol. 8, No. 10, pp. 839-841, October 1971.

29. Wu, J. C., Spring, A. H., and Sankar, N. L., "A Flow Field Segmentation Method for the Numerical Solution of Viscous Flow Problems," Proceedings, 4th International Conference on Numerical Methods in Fluid Dynamics, Springer-Verlag, pp. 452-457, 1975.

30. Wu, J. C. and Sankar, N. L., "Explicit Finite Element Solution of the Viscous Flow Problem," Proceedings, 1976 International Conference on Finite Element Methods in Engineering, 1976.

31. Wu, J. C., Sampath, S., and Sankar, N. L., "A Numerical Study of Unsteady Viscous Flow Around Airfoil," Proceedings, AGARD Fluid Dynamics Panel Symposium on Unsteady Aerodynamics, Ottawa, Canada, 1977.

32. Aral, M. M., Mayer, P.G. and Smith, C. V., "Finite Element Galerkin Method Solution to Selected Elliptic and Parabolic Differential Equations," Proceedings, Third Conference on Matrix Methods in Structural Mechanics, Wright-Patterson AFB, Ohio, pp. 215-243, 1971.

VITA

Narayana Moorthy Lakshmi Sankar was born in Rasipuram, India on January 12, 1951, and was graduated from Government High School, Singampettai, India in 1967. He received his Bachelor's degree in Aerospace Engineering from Indian Institute of Technology, Madras in 1973. He joined the School of Aerospace Engineering at Georgia Institute of Technology in 1973 and received his Master's degree in Aerospace Engineering in 1975.